Actuator disk methods for tidal turbine arrays



William Hunter
Lady Margaret Hall
University of Oxford

A thesis submitted for the degree of
Doctor of Philosophy

Michaelmas 2015

Acknowledgements

I would like to thank my supervisor Dr. Richard Willden for introducing me to the topic of tidal energy, and for his advice and encouragement throughout my DPhil. All members of the Tidal Energy Research Group at the University of Oxford contributed to the stimulating academic enviroment but working alongside Dr. Takafumi Nishino has been a highlight. I would also especially like to thank Dr. Christopher Vogel for the very enjoyable cooperation on a wind energy consulting project, and Dr. Conor Fleming for introducing me to Python!

My DPhil studentship, as well as numerous conference attendances and priority access to the University of Oxford's HPC facility, Advanced Research Computing, were generously funded by the Oxford Martin School through the Programme on Globalising Tidal Power Generation. It has been an honour to be a James Martin Research Fellow and I am very grateful for the financial support provided.

Finally, for their support and immense patience, thank you to my family.

Abstract

Tidal stream energy presents challenges that will require the development of new engineering tools if designs are to harness this energy source effectively. At first glance one might imagine that tidal stream energy can be treated as wind with appropriate adjustment for fluid properties of water over air, and account taken of the harsher offshore environment; both waves and turbulence.

However, it is now well accepted that the flow past turbines that are constrained by the local sea bed, sea surface, and possibly also neighbouring turbines and channel sides, will differ markedly from that of an ostensibly unblocked wind turbine. Garrett & Cummins (2007) were the first to demonstrate that operating a turbine in a non-negligibly blocked flow passage presents a different flow solution and importantly a significant opportunity to enhance the power that can be delivered by blocked turbines with the limit of power extraction exceeding the Lanchester-Betz limit for operation of unblocked wind turbines by a factor $(1 - B)^{-2}$ where B is the area blockage ratio of turbine to channel cross-section. Although it is impractical to array real turbines across the entire width of a channel it has been proposed to use short arrays of turbines making use of local constructive interference (blockage) effects; Nishino & Willden (2012) showed that although the phenomenal power limits of Garrett & Cummins are unobtainable in a real flow, a significant uplift in the limit of power extraction can be achieved for short fences of turbines arrayed normally to the flow in wide cross-section channels. However, it does not follow that rotors designed using unblocked wind turbine tools are capable of extracting any more power than they are designed for and hence the power uplift made available through blockage effects may be squandered.

This thesis sets out to develop design tools to assist in the design of rotors in blocked environments that are designed to make use of the flow confinement effects and yield rotors capable of extracting some of the additional power on offer in blocked flow conditions. It is the pressure recovery condition used in wind turbine design that requires relaxation in blocked flow conditions and hence it is necessary to resort to

a computational framework in which the free stream pressure drop can be properly accounted for. The tool of choice is a computational fluid dynamics embedded blade element method. As with all models with semi-empirical content it is necessary to select and test correction models that account for various simplifications inherent to the use of the blade element method over a fully blade resolved simulation. The thesis presents a rigorous comparison of the computational model with experimental data with the various correction methods employed.

The tool is then used to design rotors, first for unblocked operation, with favourable comparison drawn to lifting line derived optimal Betz rotor solutions. The final objective of the study is to design rotors for operation in short fence configurations of four turbines arrayed normally to the flow. This is accomplished and it is shown that by using bespoke in situ rotor design it is possible to extract more power than possible with non-blockage designs. For the defined array layout and operating conditions, the bespoke rotor array design yields a power coefficient 26% greater than the implied Betz limit for an unblocked rotor and 4% greater than operating the rotor designed in isolation in the same array.

Contents

1 Introduction **1**

1.1 Tidal resource 1

1.2 Analysis methods 4

1.3 Aims and objectives 6

1.4 Layout of thesis 6

2 Staggered and tuned arrays of turbines using actuator disks **8**

2.1 Introduction 8

2.2 Numerical models 10

2.2.1 Reynolds-averaged Navier-Stokes equations 10

2.2.2 Actuator disk 12

2.3 Details of the computations 13

2.4 Results 16

2.4.1 Tuning a row of four turbines 16

2.4.2 Tuning a row of eight turbines 19

2.4.3 Effect of staggering a row of seven turbines 20

2.4.4 Tuning the staggered array of turbines 23

2.5 Conclusions 30

3 General actuator disk for RANS using blade element theory **32**

3.1 Blade element theory 33

3.1.1 Correction for finite number of blades 37

3.1.2 Correction of 3D and rotational effects 37

3.1.2.1 Rotational augmentation and stall delay 37

3.1.2.2 Correction of aerodynamic drag 39

3.1.2.3 Force correction for blade tips 39

3.2 Implementation of a general actuator disk for RANS 40

3.3 Validation of the model 41

3.3.1 Description of test rotor and test case . . . 42
3.3.2 Airfoil data . . . 44
3.4 Simulation setup . . . 52
3.5 Results . . . 55
3.5.1 Convergence and grid refinement . . . 55
3.5.2 Comparison of rotor performance . . . 58
3.5.2.1 Effect of modelling . . . 61
3.5.2.2 Effect of tip-speed ratio . . . 62

4 Hydrodynamic design of tidal turbines 71
4.1 The lifting line method . . . 72
4.2 RANS actuator disk design method . . . 75
4.2.1 Corrections applied to the blade element momentum method . 76
4.2.2 RANS actuator disk design method and constraints . . . 79
4.3 Designing for unblocked flow . . . 80
4.3.1 Rotor design . . . 83
4.3.1.1 Tip constraint for twist . . . 87
4.3.2 Closing remarks on designing for unblocked flow . . . 88
4.3.3 Rotor performance . . . 88

5 Hydrodynamic design of tidal turbines for an array 97
5.1 Computational domain . . . 97
5.2 Designing for turbulence . . . 98
5.2.1 Simulation details . . . 98
5.2.2 Simulation results . . . 98
5.3 In situ array rotor design . . . 104
5.3.1 The computational domains . . . 104
5.3.2 Simulation results . . . 105
5.3.3 Tuning the four turbine array . . . 107
5.3.4 Closing comments on in situ tidal turbine design . . . 107
5.4 Rotor performance . . . 113

6 Conclusions 117
6.1 Conclusions . . . 117
6.2 Contributions . . . 118
6.3 Future work . . . 119

Bibliography **121**

Nomenclature

Roman

$\hat{u}$	axial induced velocity by a unit strength horseshoe vortex
Re	Reynolds number
Re_c	chord Reynolds number
A	disk area
a	axial induction factor
a'	azimuthal induction factor
a, b, d	model coefficients, Eq. 3.27
B	channel blockage
c	chord
c_1, c_2, c_3	model coefficients, Eq. 3.31
C_{pres}	pressure coefficient
C_μ	turbulence modelling constant
C_D	lift coefficient
C_L	lift coefficient
C_n	axial force coefficient, reference velocity U_{rel}
C_P	power coefficient, reference velocity U_∞
C_T	thrust coefficient, reference velocity U_∞
C_t	tangential force coefficient, reference velocity U_{rel}

$C_{\epsilon 1}$, $C_{\epsilon 2}$ turbulence model constants

$C_{L,\text{inv}}$ inviscid lift coefficient

$C_{L,2D}$ 2D lift coefficient

$C_{L,3D}$ 2D lift coefficient corrected for 3D effects of rotation

C_{TH} axial force coefficient, reference velocity $\sqrt{U_\infty^2 + (\Omega r)^2}$

$C_{TL,\text{nom.}}$ nominal local thrust coefficient, reference velocity U_D

C_{TL} local thrust coefficient, reference velocity U_D

C_{TQ} tangential force coefficient, reference velocity $\sqrt{U_\infty^2 + (\Omega r)^2}$

D diameter of rotor/disk

D drag force

F Glauert/Prandtl tip loss factor

F_1 performance tip correction of Shen et al.

f_L lift augmentation factor, Eq. 3.27

F_n axial force component

F_t tangential force component

g acceleration due to gravity

g model coefficient, Eq. 3.30

G_k turbulent production

H height of computational domain

K resistance coefficient

L lift force

L turbulence length scale

M momentum sink

n number of disks in array

n_{sim}	number of disks in the computational domain
P	power
p	pressure
p_{atm}	atmospheric pressure
p_v	vapour pressure
Q	torque
q	reference dynamic pressure
r	radial coordinate
r_{hub}	hub radius
r_c	radius of control point
r_v	radius of trailing vortex
s	lateral spacing between actuator disks
s_{sub}	lateral spacing between actuator disks in sub-array
T	thrust
t	maximum profile thickness, usually presented as a percentage of chord
TI	turbulence intensity
U	mean velocity, in Reynolds-Averaged sense
u	induced axial velocity
u'	fluctuating velocity component
U_∞	upstream undisturbed velocity
U_{rel}	relative (to aerofoil chord line) velocity magnitude
U_θ	θ component of velocity, tangential direction
U_d	normal velocity at disk
U_x	x component of velocity, streamwise, axial direction

W width of computational domain

w induced tangential velocity

x, y, z Cartesian coordinates

Z number of blades

$C_P{}^*$ $\equiv C_{P\max}$ for optimum non-staggered array

$C_{P\max}$ maximum power coefficient (at optimum operating point)

Greek

α angle of attack

α_0 zero lift angle of attack

α_{LD} angle of attack at maximum ratio lift to drag

β blade twist

δr blade element width

Δr_v spanwise length of horseshoe vortex at lifting line

Δ relative variation in percent (Chapter 3)

δ_{ij} Kronecker delta

ϵ turbulent dissipation rate

η basin efficiency

Γ Circulation

Γ_∞ Circulation for ideal Betz rotor

Λ modified tip speed ratio, Eq. 3.27

λ tip speed ratio

λ_r local blade speed ratio ($\equiv \lambda r/R$)

μ dynamic viscosity

ν kinematic viscosity

ν_t turbulent eddy viscosity

Ω rotational speed

ϕ flow angle at disk (Ch. 3 onwards)

ϕ scalar variable (Ch. 2)

ρ density

σ solidity (Ch. 3 onwards)

σ_k turbulent Prandtl number (Ch. 2)

θ azimuthal coordinate, $\theta = 0$ coincides with $+y$-axis (up)

ξ streamwise separation of sub-arrays in staggered array

k turbulent kinetic energy

Subscripts

ϵ pertaining to ϵ equation (Eq. 2.6)

u. uncorrected (for wind tunnel blockage effects)

d specific to disk (rather than array)

k pertaining to k equation (Eq. 2.5)

R at blade tip, i.e. $r/R = 1$

Other

$\langle \bullet \rangle$ spatial average operator (Ch. 2)

$\overline{\bullet}$ Reynolds averaging operator (Ch. 2)

$\overline{\bullet}$ azimuthal averaging operator (Ch. 3 onwards)

Abbreviations

AD Actuator Disk.

BEM Blade Element Momentum.

CARDC China Aerodynamics Research and Development Center.

CFD Computational Fluid Dynamics.

CSU Colorado State University.

DUT Technical University of Denmark.

FST Freestream Turbulence.

LL Lifting Line.

LMADT Linear Momentum Actuator Disk Theory.

NREL National Renewable Energy Laboratory.

OSU Ohio State University.

RANS Reynolds-Averaged Navier Stokes.

S809 NREL aerofoil section name.

SIMPLE Semi-Implicit Method for Pressure-Linked Equations.

TC Tip Constraint.

VOF Volume Of Fluid.

Chapter 1

Introduction

1.1 Tidal resource

The tides are cyclic variations in the sea level caused by the gravitational forces that exist between the Earth (and its oceans), the Moon and the Sun. 'Equilibrium Tidal Theory'[10] gives provides a basic explanation to some of the properties of the tides. The effect of a satellite, i.e. the Moon, on a planet with a surface layer of fluid, i.e. the Earth, is to cause the fluid to bulge in both directions along the planet-satellite axis. Fluid particles on the side closest to the satellite experiences a greater force than those furthest from the satellite, while the total force of attraction between the planet and the satellite remains fixed. The vectorial difference explains the tidal 'bulges' which appear to travel around the Earth as it rotates.

The Moon's orbital period about the Earth (actually about the centre of mass of the Earth-Moon system, which is inside the Earth) is 27.3 days, while the Earth's rotational period is 24hrs. As both rotations are in the same direction, the Moon has an orbital period of 24hrs 50mins in an Earth reference frame, leading to an almost diurnal tidal cycle with the tides occurring approximately an hour later each day. The (almost) diurnal contribution of the Moon to tidal elevation is referred to as the M2 constituent. The Sun has a weaker but exactly diurnal effect termed S2. The superposition of the two effects results in a modulated tidal elevation with a maximum spring tide at full and new moon (when the Sun is in line with the Earth-Moon axis), and minimum neap tide at $\frac{1}{4}$ and $\frac{3}{4}$ moon.

Equilibrium tidal theory however does not account for land masses obstructing the propagation of tidal waves, the Coriolis effect or the speed of waves in varying bathymetry. The tides observed at the coast occur as the interaction between the tides raised in the deep ocean, and the continental shelf bathymetry and coastline.

Figure 1.1 shows the resulting map of tidal elevation caused only by the M2 constituent. The white lines, called cotidal lines, indicate constant phase and extend from a common point, the amphidromic point, to the coastline. The wave systems travel around the amphidromic points in the direction indicated by the black arrows.

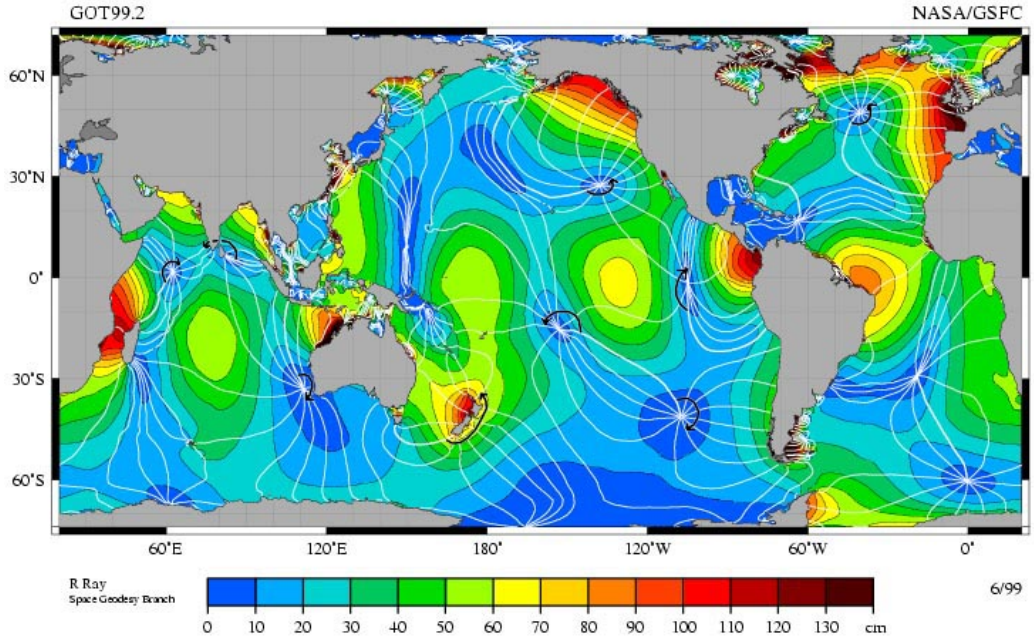


Figure 1.1: Contour map of M2 tidal constituent. Cotidal lines (lines of constant phase) are overlaid in white. Black arrows indicate direction of wave system about amphidromic point (intersection of cotidal lines). Graphic source: Wikipedia (Creative Commons).

Western Europe stands out globally as one of the areas with high tidal amplitudes. Due to its jagged coastline and numerous islands, channels and headlands, there are many locations around the UK with high tidal stream velocities. Figure 1.2 shows a map of peak flow speed for a mean spring tide near the UK coastline. The highest speeds, greater than 4 m/s, occur in the Pentland Firth off the north tip of Scotland. For tidal turbine developers active in the UK ([21]), this represents the maximum flow speed a device is expected to operate in, while 2-2.5 m/s may be the realistic target for rated power.

Despite maps of mean flow speed, estimating the available tidal resource remains challenging. The technically feasible resource in the UK was recently estimated at 29.0 TWh/y [8], where 'technical resource' is defined as "the energy that can be harvested from tidal currents using envisaged technology options and restrictions (including

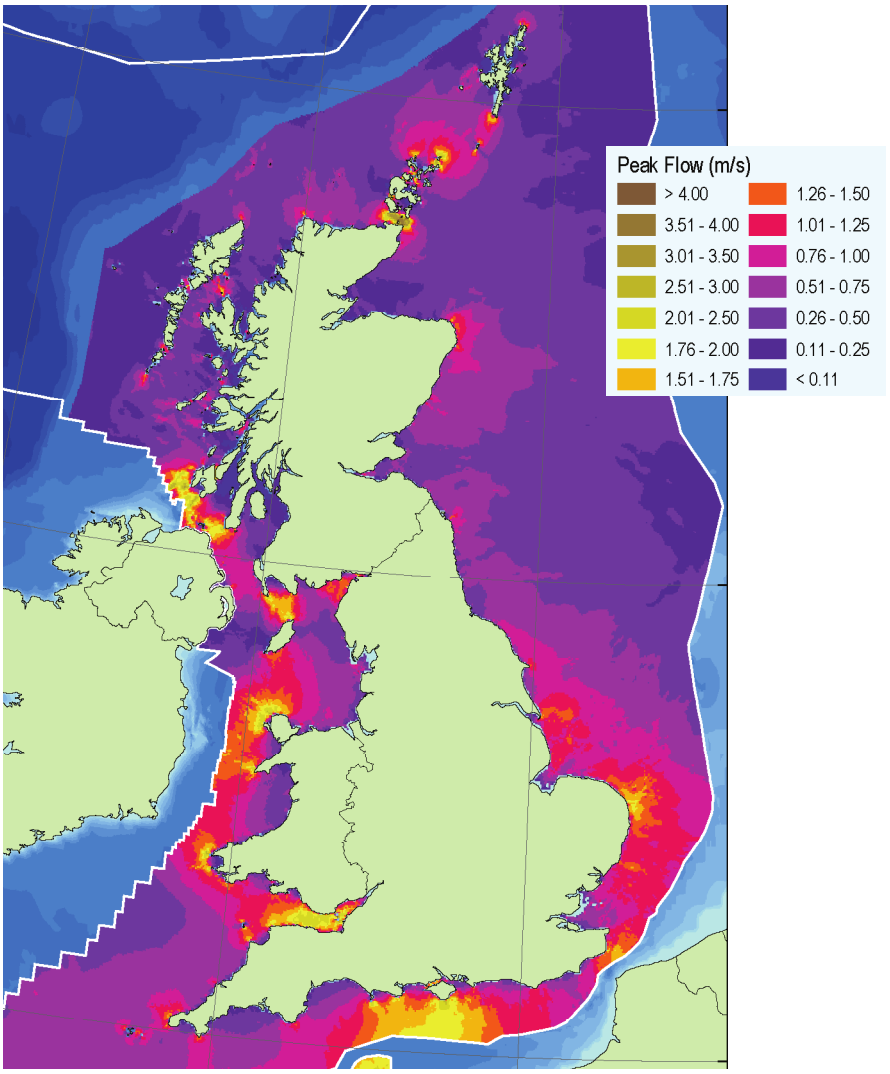


Figure 1.2: Peak Flow for a Mean Spring Tide (BERR [5])

project economics) without undue impact on the underlying tidal hydrodynamic environment". The underlying hydrodynamic model applied to 30 key sites around the UK is based on the work of Garrett & Cummins [27], which is a one-dimensional model of an idealised channel.

Draper et al. [15] performed numerical simulations using the shallow water equations (depth-averaged Navier-Stokes equations and continuity equation) of the Pentland Firth to estimate the maximum power that can be extracted by placing tidal stream power devices across across the Firth. Comparing the average power due to M2 forcing the numerical model estimates 3.75 GW compared to 3.1 GW from the analytical model of Garrett & Cummins, which represents agreement to within 20%.

The resource according to the numerical model over a full spring-neap cycle was 4.2 GW (36.8 TWh/y).

1.2 Analysis methods

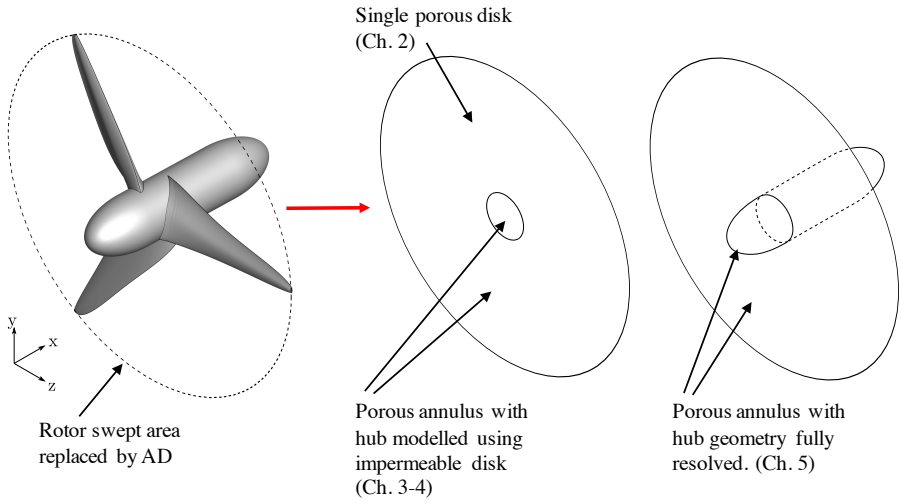


Figure 1.3: Left: Three bladed turbine designed using lifting line method to optimize power, using constant thickness S809 aerofoil section, with hub diameter of 0.15 times rotor diameter treated using image vortex system. Streamwise flow in x direction, rotor rotation in positive sense about x axis. (Full details to follow in Chapter 4). Right: Actuator disk representations of the rotor, as used in the remainig chapters of this thesis.

The majority of devices being developed ([21]) are horizontal axis axial flow turbines, which are at least aesthetically similar to modern commercial wind turbines. The analysis methods for tidal turbines are therefore similar if not identical to the methods used in wind turbine research which are described in one of many review papers, e.g. Sanderse et al. [60]. They include: Lifting line and vortex lattice methods [38], fully blade resolved computational fluid dynamics [71], Reynolds-Averaged Navier Stokes (RANS) embedded actuator line [69] and actuator disk methods. In this thesis, various implementations of the actuator disk method are used as it is the least computationally expensive method that can naturally account for the effect of blockage and turbulence on tidal turbines in channels

In their literature review, Batten et al. [4] list numerous applications of the simple and blade element actuator disk in RANS computations to study the performance and wakes of tidal turbines. One of the earliest investigations in the tidal energy field was a comparison of RANS actuator disk results with experimental results using a

porous plate by Sun et al. [73]. A recent implementation of a general blade element actuator disk for the study and design of ducted tidal turbines was presented by McIntosh et al. [45], and it was recently used to study the design of tidal turbines for blocked flows by Schluntz & Willden [61].

In their review of Computational Fluid Dynamics (CFD) for wind turbine wake aerodynamics, Sanderse et al. [60] list many much earlier implementations of actuator disk models. The simple actuator disk model was implemented for a axisymmetric Euler equation solver in a vorticity-streamfunction formulation as early as 1992 in Denmark [68], while integration of blade element theory in this model was presented in 1995 [67].

Sanderse et al. and a further 2011 review by Sørensen et al. [66] list notable attempts to directly model wind turbine rotors in a RANS-CFD framework without the use of actuator methods. Both suggest that the earliest study originated in Denmark in 1998, when Sørensen & Hansen [70] presented simulations of a three-bladed wind turbine with diameter, $D = 41m$ (then field size). The Navier-Stokes equations were solved in a frame of reference rotating with the turbine blades, with additional terms accounting for the Coriolis and centripetal acceleration (See, e.g. [77]), thus permitting a steady state solution. The $k\omega$-SST two-equation turbulence model was employed to model the eddy viscosity. An almost identical approach was used by Sørensen et al. [71], as part of the blind modelling comparison following the National Renewable Energy Laboratory (NREL) Phase VI wind turbine wind tunnel experiment. This is particularly interesting in the context of the present thesis, as data from the same experiment is used to validate the actuator disk model in Chapter3.

Finally, Fleming [24] thoroughly discusses the challenges and merits of blade resolved simulation for tidal turbine research and reviews the small number of blade resolved simulations applied to tidal turbines, with the earliest study due to O'Doherty et al. [55] in 2009. Interestingly, this study was used to study multiple rotors using the unsteady RANS ("URANS") equations, with each rotor embedded in a rotating cylindrical mesh, which interfaces with the stationary global mesh using a "sliding-mesh" technique. Despite considerable computational expense, the contour plots of field variables indicate a clear dependency on the mesh resolution, which appears to be very coarse, no grid convergence study was included in the study.

1.3 Aims and objectives

The work in this thesis starts from the premise that significant advances can be made in the design of tidal rotors to take advantage of the significant performance enhancements afforded by blockage as postulated by Garrett & Cummins [28] for turbines in rows of infinitely arrayed turbines, and by Nishino & Willden [51] for partial arrays of closely spaced turbines occupying only a small fraction of the overall width of the channel. The overall objective of this work is to: *Develop a method to design an optimally performing array of rotors for operation in a short array configuration in a channel of realistic geometry with realistic inflow turbulence conditions.*

To support this objective the following aims were set:

- To develop an upper limit on the performance of a short fence of optimal energy extracting disks subject to finite blockage constraints of a realistic channel geometry.
- To further develop and validate a CFD-embedded blade element method that can be used to evaluate the performance of rotor designs in arbitrary flow conditions; blockage and turbulence.
- To develop a CFD-based blade element method to design rotors with appropriate loading constraints to reflect actual tip performance.
- To use the developed method to design rotors for blocked and unblocked flow conditions, low and high freestream turbulence.
- To extend and use the developed method to design multiple rotors simultaneously for optimal in situ array performance.

1.4 Layout of thesis

This thesis is structured along the lines of the aims outlined above. Chapter 2 considers arrays of actuator disks arrayed in two short fence configurations; 4 and 7 turbines. The purpose this study is to ascertain the limit on energy extraction of such arrays and thus the turbines are presented using optimal energy extracting porous disks without recourse to blade and rotor detail. The study considers the effect of applying non-homogeneous array loadings as well as the effect of streamwise staggering of every other device in the 7 turbine configuration. Chapters 3 to 5 are then concerned with the design and representation of real turbines through CFD embedded blade element

methods. Chapter 3 seeks to validate a CFD-blade element method by comparison to published experimental data from the NREL Phase VI tests. The chapter also investigates the role of corrections to account for three-dimensional and tip effects not considered in the basic momentum conservation models. Chapter 4 uses the validated CFD-blade element model to develop rotor designs. Rotor designs are developed for hypothetical unblocked scenarios and comparison made to those developed using a lifting line method that seeks the optimal Betz rotor for given blade number and lift-to-drag characteristic. The design process requires target functions and, by reference to the optimal Betz designs, the chapter develops target radial thrust loading profiles. Chapter 5 makes use of the rotor design tool to consider bespoke rotor designs for different flow conditions; blockage and freestream turbulence. Of interest is the extent to which rotors can be designed for in situ performance within a short, 4 turbine, closely spaced array in a realistic channel geometry much wider than the length of the short array. The array chosen for analysis is that was considered in Chapter 2 in the framework of optimal energy extracting actuator disks, aiding comparison between the theoretical limit of energy extraction of a short fence, and what can be achieved through bespoke in situ rotor design. Finally Chapter 6 draws conclusions on the work presented in this thesis and suggests areas of potential future work.

Chapter 2

Staggered and tuned arrays of turbines using actuator disks

The contents of this chapter appear in the article "Investigation of Tidal Turbine Array Tuning using 3D Reynolds-Averaged Navier-Stokes Simulations" by Hunter et al. [35].

2.1 Introduction

Most successful attempts to harness tidal stream energy so far have resembled modern wind turbines, i.e. a horizontal axis two- or three-bladed rotor mounted on a supporting tower, e.g. [25]. It has been known for almost a century that the power extractable by a wind turbine can be estimated using (Linear Momentum Actuator Disk Theory (LMADT)). By modelling the turbine as a step drop in static pressure over the swept area of the rotor in the axial flow direction, LMADT combines control volume analysis of momentum, mass and energy and the assumption of an incompressible, inviscid fluid to estimate the power that can be extracted from a flow. For wind turbines, the maximum power that can be extracted, normalised by the kinetic energy flux of the undisturbed flow through the equivalent rotor swept area is now known as the Betz limit [11]:

$$C_{P\max} = \frac{P_{\max}}{\frac{1}{2}\rho A U_\infty^3} = 16/27 \tag{2.1}$$

where A is the rotor swept area, U_∞ is the undisturbed upstream velocity and ρ is the fluid density. At this maximum, the velocity at the disk plane $U_d = 2/3U_\infty$, or the so-called "induction factor" $a = 1 - U_d/U_\infty = 1/3$.

The same limit of power extraction may apply to an isolated tidal turbine in a very large channel. However, tidal turbines are expected to be located in tidal

streams where the depth of the flow is typically $1.5D$ - $5D$, where D is the diameter of the rotor. The flow will therefore be constrained vertically by the sea bed and the free surface [34], possibly also laterally in narrow tidal channels, and by the presence of other devices. By considering an additional stream-tube for the accelerated flow bypassing a turbine, Garrett & Cummins [28] found that the $C_{P\max}$ of a tidal turbine in a constrained channel is increased by a factor of $(1-B)^{-2}$ where B is the blockage, defined as the ratio of the rotor swept area of the turbine, or turbines, to the cross-sectional area of the channel. Nishino & Willden [50] confirmed that this result agrees well with computational fluid dynamics (CFD) simulations of an actuator disk in channels of various cross-section. They also found that the limit could be exceeded when the effect of turbulent mixing in the near wake was considered. Turbulent mixing was found to result in momentum transfer from the faster bypass flow to the slower core flow, accelerating the core flow through the turbine, thus increasing the $C_{P\max}$.

In order to extract sufficient energy from tidal resources to make a meaningful contribution to energy demands, many devices will need to be installed in a given tidal channel. Groups of devices in rows across the channel cross-section are often referred to as "tidal fences" or "tidal turbine arrays". In long channels, it may also be possible to install multiple rows along the length of the channel to create tidal energy farms.

While LMADT suggests that turbines should be installed across a large fraction of a channel cross-section to achieve high blockage, this is unlikely to be feasible due to competing uses (navigation, wildlife, etc.) and varying bathymetry. It is more likely that turbines will be installed in arrays occupying only a small fraction of a channel cross-section, i.e. with small global blockage (ratio of total turbine frontal area to channel cross-sectional area). By applying the model of Garrett & Cummins [28] for the flow around each turbine also to the flow around the entire array, Nishino & Willden [51] have developed an analytical model for such a 'partial' array of turbines. One of the key findings of this analysis was the existence of optimal intra-turbine spacings. For a given water depth, the optimal spacing is the result of the competing effects of local blockage due to neighbouring turbines and the effect of array scale flow reduction as the overall thrust of the array increases. An extended version of this analytical model [54] compared well with 3D RANS actuator disk simulations, which also indicated that turbulent mixing in the array near wake was responsible for the increased power of an optimally spaced partial turbine array.

As discussed in [52], the analytical models to date have delivered important results but still represent an incomplete description of the wake mixing mechanisms. Additionally, all of the analytical models discussed assume uniform inflow and operating conditions across the array. The current work aims to investigate the effects of allowing variable operating conditions for turbines across an array. It is postulated that turbines at the centre of the array will experience a different flow than those closer to the fence edges, and therefore non-uniform operating conditions may be required to achieve better (or optimal) performance. In a further experiment, an array of turbines is staggered with respect to the streamwise direction. In this case it is postulated that the downstream turbines located in the fast bypass flow of the upstream turbines may benefit the overall output of the array. These two scenarios are investigated numerically using computational fluid dynamics (CFD) to solve the Reynolds-Averaged Navier-Stokes equations in combination with actuator disk models for the turbines. A concurrent study [16]([17]) presents a different extension to LMADT to consider two rows of tidal turbines placed in centred or staggered arrangement. The findings are presented as a ranking of different turbine arrangements based on maximum power coefficient and efficiency. In Section 2.4.3 the results of the current work are compared with the findings in [16].

2.2 Numerical models

2.2.1 Reynolds-averaged Navier-Stokes equations

In this study, numerical solutions are presented of the incompressible Reynolds-averaged Navier-Stokes (RANS) equations:

$$\frac{\partial U_i}{\partial x_i} = 0 \tag{2.2}$$

$$\frac{\partial U_i}{\partial t} + \frac{\partial}{\partial x_j}\left(U_i U_j\right) = -\frac{1}{\rho}\frac{\partial p}{\partial x_i} + \frac{\partial}{\partial x_j}\left[\nu\left(\frac{\partial U_i}{\partial x_j} + \frac{\partial U_j}{\partial x_i}\right)\right] + \frac{\partial}{\partial x_j}\left(-\overline{u_i' u_j'}\right) \tag{2.3}$$

where U_i and p are the time-averaged velocity tensor and pressure, ν is the kinematic viscosity, $\overline{\phi}$ is the time averaging operator and ϕ' is a random fluctuation about the time-averaged value. The RANS equations have an identical structure to the Navier-Stokes equations with the exception of an additional unknown term $-\overline{u_i' u_j'}$, which is known as the Reynolds stress tensor. This is modelled using the Boussinesq

hypothesis to relate the Reynolds stresses to the mean velocity gradients:

$$-\overline{u_i' u_j'} = \nu_t \left(\frac{\partial U_i}{\partial x_j} + \frac{\partial U_j}{\partial x_i} \right) - \frac{2}{3} k \delta_{ij} \tag{2.4}$$

in which $k = \frac{1}{2}\overline{u_i' u_i'}$ is the turbulent kinetic energy and ν_t is the so-called turbulent viscosity. This is modelled using the standard k-ϵ model [41], which solves transport equations for k and for the turbulent dissipation rate, ϵ:

$$\frac{\partial k}{\partial t} + \frac{\partial}{\partial x_j}\left(k U_j\right) = \frac{\partial}{\partial x_j}\left[\left(\nu + \frac{\nu_t}{\sigma_k} \right) \frac{\partial k}{\partial x_j} \right] + G_k - \epsilon \tag{2.5}$$

where

- σ_k is the turbulent Prandtl number for k, given a value of 1.0
- the turbulent production due to mean velocity gradients, G_k, is modelled as $G_k = \nu_t S^2$, where S is the modulus of the mean rate-of-strain tensor, defined as $S = \sqrt{2 S_{ij} S_{ij}}$.

Transport of ϵ is modelled as:

$$\frac{\partial \epsilon}{\partial t} + \frac{\partial}{\partial x_j}\left(\epsilon U_j\right) = \frac{\partial}{\partial x_j}\left[\left(\nu + \frac{\nu_t}{\sigma_\epsilon} \right) \frac{\partial \epsilon}{\partial x_j} \right] + C_{\epsilon 1} \frac{\epsilon}{k} G_k - C_{\epsilon 2} \frac{\epsilon^2}{k} \tag{2.6}$$

where

- σ_ϵ is the turbulent Prandtl number for ϵ, given a value of 1.3
- $C_{1\epsilon} = 1.44$, $C_{2\epsilon} = 1.92$ are empirically determined coefficients.

The variable required in Equation 2.4 to close Equation 2.3 is the turbulent viscosity ν_t, which is computed as:

$$\nu_t = C_\mu \frac{k^2}{\epsilon} \tag{2.7}$$

where $C_\mu = 0.09$. (For details, see e.g. [57]). The k-ϵ model was chosen in preference to other turbulence models due to its robustness and general success for the prediction of free shear flows.[1] The model is also chosen to allow direct comparison with related research, e.g. [50].

[1] The actuator disk methods used throughout this thesis result in free shear emanating from the edges of the disk, while avoiding the need to compute the shear caused by the rotor blade surfaces.

2.2.2 Actuator disk

Analogously to the actuator disks of LMADT, the turbines were modelled using a momentum extraction term in the RANS equations. The change in momentum flux per unit disk area is calculated locally as

$$M_x = K\left(\frac{1}{2}\rho U_d^2\right) \tag{2.8}$$

where the parameter K (resistance coefficient) can be used to vary the thrust acting on the disk. Hence the thrust on each disk is calculated as

$$T_{d(i)} = \int_{\text{disk}(i)} M_x \mathrm{d}A_d = K_i \frac{1}{2}\rho \int_{\text{disk}(i)} U_d^2 \mathrm{d}A_d \tag{2.9}$$

where i denotes the i-th disk in the array of n disks. The total thrust on the n disks of equal size A_d is calculated as

$$\sum_{i=1}^{n} T_{d(i)} = \frac{1}{2}\rho A_d \sum_{i=1}^{n} K_i \langle U_d^2 \rangle_i \tag{2.10}$$

where $\langle\phi\rangle$ is the spatial average of the variable ϕ over the disk. Thus the disk thrust coefficient is defined as

$$C_{T\,d(i)} = \frac{T_{d(i)}}{\frac{1}{2}\rho U_\infty^2 A_d} = K_i \frac{\langle U_d^2 \rangle_i}{U_\infty^2} \tag{2.11}$$

and the n-disk-averaged array thrust coefficient as

$$C_T = \frac{\sum_{i=1}^{n} T_{d(i)}}{\frac{1}{2}\rho U_\infty^2 n A_d} = \frac{1}{n}\sum_{i=1}^{n} K_i \frac{\langle U_d^2 \rangle_i}{U_\infty^2}. \tag{2.12}$$

The power available at the disk plane is calculated as

$$P_{d(i)} = \int_{\text{disk}(i)} M_x U_d \mathrm{d}A_d = K \frac{1}{2}\rho \int_{\text{disk}(i)} U_d^3 \mathrm{d}A_d. \tag{2.13}$$

Similarly, the disk and array power coefficients are defined as

$$C_{P\,d(i)} = K_i \frac{\langle U_d^3 \rangle_i}{U_\infty^3}, \qquad C_P = \frac{1}{n}\sum_{i=1}^{n} K_i \frac{\langle U_d^3 \rangle_i}{U_\infty^3}. \tag{2.14}$$

Finally, the spatially averaged axial flow induction factor is defined as

$$a_{d(i)} = 1 - \frac{\langle U_d \rangle_i}{U_\infty}, \qquad a = 1 - \frac{1}{n}\sum_{i=1}^{n} \frac{\langle U_d \rangle_i}{U_\infty}. \tag{2.15}$$

The actuator disk turbine model is chosen for its simplicity and generality, requiring no details of the rotor geometry, and describing the operating condition using

only the parameter K. These are desirable features when the limit of power extraction of a single device, or a single row of devices is of interest. To investigate the performance of a device in complex inflow, e.g. for a device positioned in the wake of another upstream device or interference effects of turbines in an array, a more realistic representation of a turbine would be required. Chapters 3-5 present the development, validation and application of a more advanced actuator disk model which considers the geometrical description of rotor blades and their rotational speed.

2.3 Details of the computations

Computational grids were created to simulate arrays of four, eight and seven turbines in rectangular channels. The actuator disks modelling the turbines were positioned at the centre of the channel cross-section (yz plane) at $x = 0$ with the channel extending $50D$ upstream and downstream of the disks. For a single turbine modelled as an actuator disk, a domain extending $5-10D$ upstream and $10-15D$ downstream (depending on freestream turbulence levels) is sufficient for accurate calculations of the integrated power and thrust coefficients. The domain around an array of turbines should scale approximately as the width of the array in order to achieve the same convergence of the array scale flow.

A uniform inlet velocity of 2 m/s was prescribed at the inlet; the working fluid was assigned a dynamic viscosity, $\mu = 0.001$ Pa.s and density, $\rho = 1000$ kg/m^3, giving a Reynolds number based on disk diameter $D = 20$ m, of $\mathrm{Re} = 4 \times 10^7$. As discussed in Section 2.1, turbines will likely be installed in closely (optimally) spaced arrays, occupying only a small fraction of a wide channel. For the current study, the channel depth (y-direction) was fixed at $2D$ while the width (z-direction) was varied as $10nD$, where n is the number of disks in the array, in order to maintain a constant global blockage of $B = 0.039$. The lateral spacing (gap) between the disks was fixed at $s = 0.25D$, which is close to the optimal spacing predicted by the analytical model of Nishino & Willden [51] for the present array lengths. Due to the symmetry of the flow domain about the $y = 0$ and $z = 0$ planes, the computational domain comprised only a quarter of the channel and actuator disk array (i.e. $-50D \leq x \leq 50D$, $0 \leq y \leq D$ and $0 \leq z \leq 5nD$).

The lateral and vertical boundaries of the domain are assigned slip wall conditions, which means that the sea surface is modelled as a rigid fixed lid. Consul et al. [12] compared CFD simulations of a cross-flow tidal turbine modelling the upper boundary as either a rigid fixed lid or a physically more accurate deformable free surface

Table 2.1: Description of physical domain for channel simulations. Due to symmetry of the solution about the horizontal centre plane, $y = 0$, and vertical centre plane, $z = 0$, the computational domain comprises one quarter of the physical domain, in the quadrant where y and z are positive.

Array layout	Length, Width, Height	Disk spacing
$n = 4$, non-staggered	$100D$, $10nD$, $2D$	$s/D = 0.25$
$n = 8$, non-staggered	$100D$, $10nD$, $2D$	$s/D = 0.25$
$n = 7$, staggered	$100D$, $10nD$, $2D$	$s/D = 0.25$, $s_{\text{sub}}/D = 1.5$

using the volume of fluid (Volume Of Fluid (VOF)) model. They found that while global blockage leads to considerable increases in C_P, in agreement with LMADT, additional increases due to the deforming free surface only become significant at very high blockage levels, i.e. an order of magnitude greater than in the current study. Hence, the computational expense of the VOF model was avoided in the current study, and the rigid fixed lid model used in all cases.

Inlet turbulence was prescribed with turbulence intensity of 20 % and turbulent length scale $L = 0.2D$. With no shear to sustain it, the turbulence intensity decreased monotonically between the inlet and the disk plane. The length scale at the inlet was chosen to achieve free-stream turbulence at the disk plane with turbulence intensity of 4-5 %. Higher free-stream turbulence is known to enhance near-wake mixing and increase the limit of power extraction [50]; the chosen values provide a lower bound on potential power limits and the key findings should be unchanged.

Table 2.2: Description of boundary conditions for channel simulations (cf. Table 2.1). The unrealistically high inlet turbulence intensity is set to achieve a realistic level at the disk plane, which has been appended to the table for reference, despite not being an actual boundary condition.

Location	Boundary condition / operation condition
inlet	$U_\infty = 2$ m/s, (TI = 20%)
outlet	$p = 0$
$y = 0$, $z = 0$	symmetry
$y = D$, $z = 5nD$	slip wall
disk plane ($x = 0$)	TI $\approx$ 4..5%

Computations were performed using the commercial CFD solver, ANSYS® Fluent®

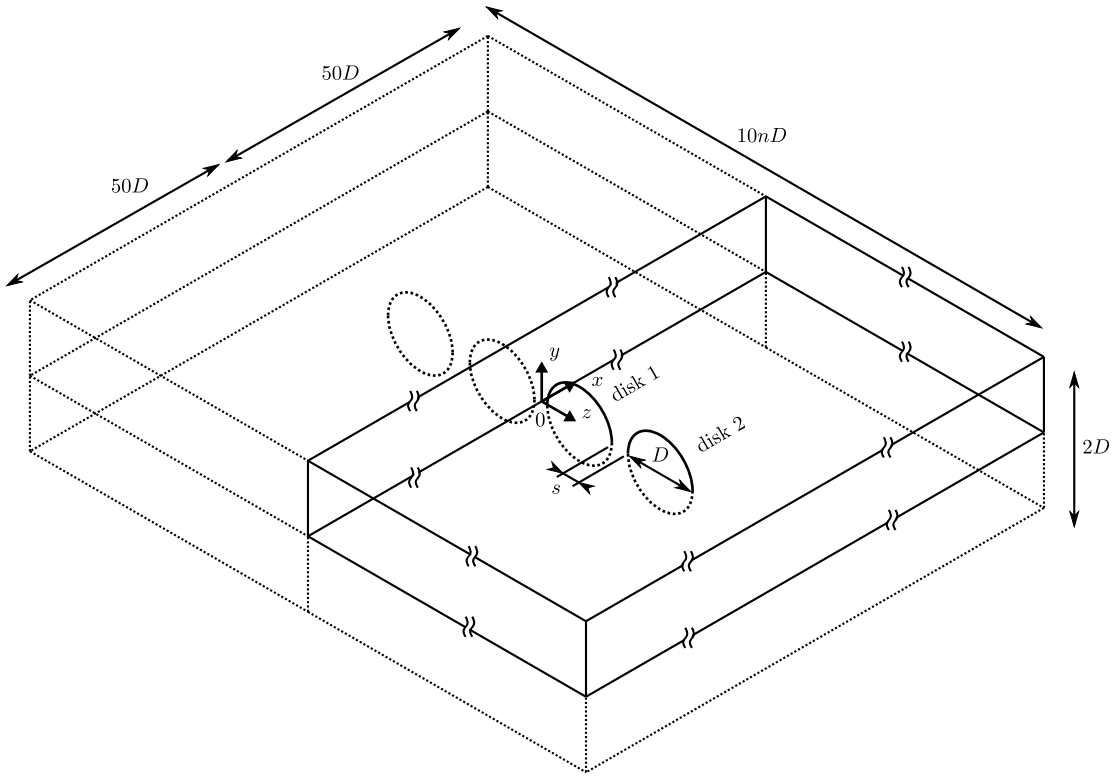


Figure 2.1: Schematic diagram of the physical (dotted) and computational domain for the four disk array.

[1] using its default "pressure-based" segregated solver for the steady state, time-averaged Navier-Stokes equations. The standard pressure interpolation scheme is a co-located scheme (pressure and velocity are evaluated at the cell centres), based on that proposed by Rhie and Chow [58] developed to suppress pressure oscillations, and is nominally second order accurate in space. The Semi-Implicit Method for Pressure-Linked Equations (SIMPLE) Algorithm [56] was used for pressure-velocity coupling.

The mesh resolution and topology shown in Fig. 2.2 is very similar to that used in the previous study by Nishino & Willden [50]. A block-structured hexahedral mesh was created by extruding a 2D block-structured quad mesh in the streamwise direction. Fig. 2.2 shows how the resolution has been refined to resolve the shear layers at the edge of the disk (initial cell height of D/200 at the disk perimeter, geometric growth rate < 1.2). A grid sensitivity study was performed by Nishino & Willden

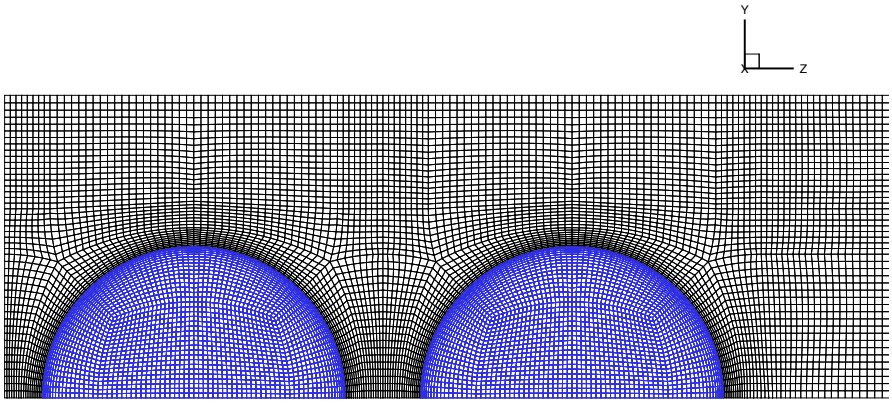


Figure 2.2: Cross-sectional view of mesh at disk plane.

[50] and the resolution of the current mesh represents their "medium" resolution which was found to be adequate for grid-independent solutions of the desired integral quantities a_d, C_{Pd} and C_{Td}. Their tests included comparing the current resolution with a further refinement in all directions, resulting in a total cell count 8 times larger, at a range of operating conditions and turbulence levels. In all cases, the change in C_{Pd} was less than 0.5%.

2.4 Results

2.4.1 Tuning a row of four turbines

As outlined in Section 2.2.2, C_P for the array is evaluated using the flow field solution so the operating conditions required to achieve $C_{P\max}$ are not known a priori. LMADT can be used to show that Betz limit, Eq. 2.1, is achieved at a thrust coefficient $C_T = 8/9$, or equivalently by a local thrust coefficient of 2 based on U_D, which corresponds directly to the resistance coefficient K of the numerical actuator disk model. For arrays of actuator disks in finite blockage and considering viscous effects however, this value was approached numerically by repeated simulations using a range of values of K. Using a cubic spline interpolation of the simulation results, $C_P = \text{function}(K)$, the location of $C_{P\max}$ was estimated by interpolation. As outlined in Section 2.3, the computational domain comprised only a quarter of the channel, which for the current four turbine array included one half of two actuator disks (cf. Fig. 2.2). K was varied independently for each of the two disks in the computational domain. Considering

the symmetry condition, the value K_1 controlled the operation of the two turbines at the centre, and K_2 the turbines at both ends of the four turbine array. For a range of values in the parameter space of K_1 and K_2, the power and thrust coefficients, C_P and C_T, were calculated as described in Section 2.2.2.

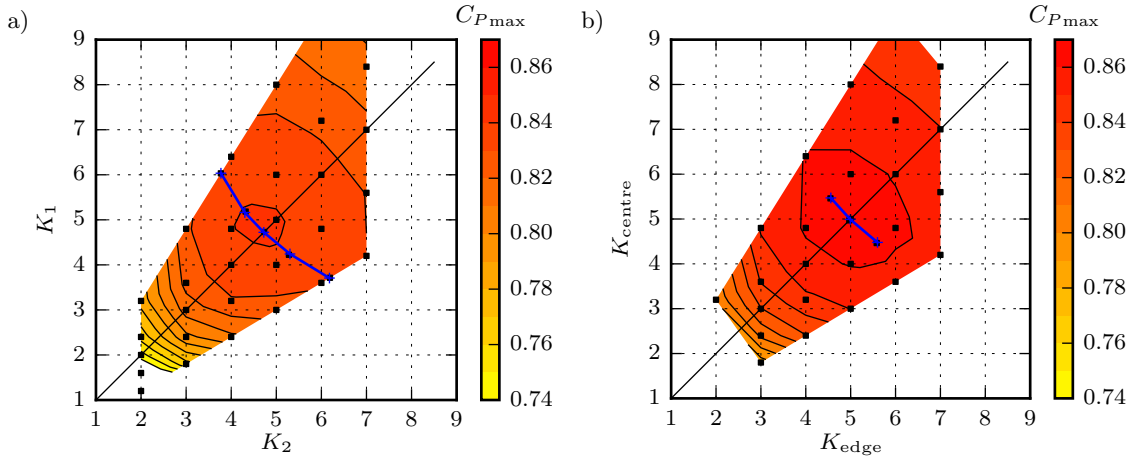


Figure 2.3: Array C_P as a function of array tuning for: a) four turbine array, b) eight turbine array. Squares indicate simulated cases; the locus of $C_{P\max}$ for a given ratio (e.g. K_1/K_2 for the four turbine array) is indicated by the blue crosses.

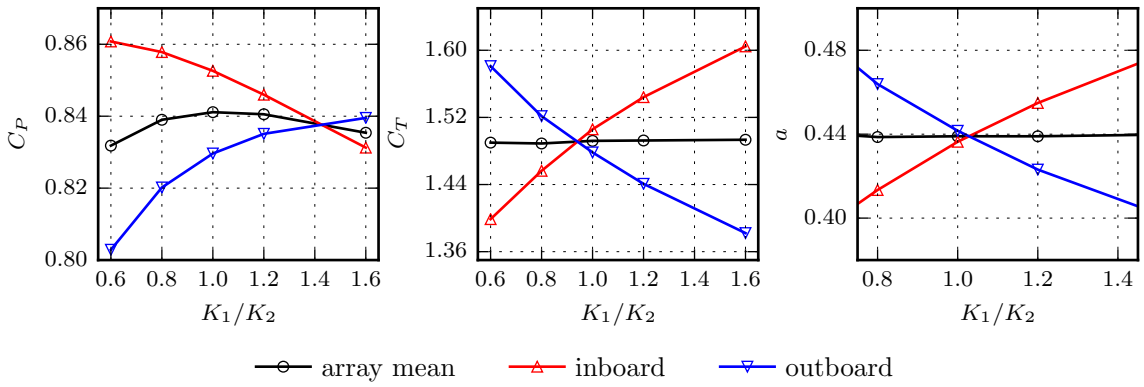


Figure 2.4: Maximum array C_P for each K_1/K_2, plotted together with contributions from the centre and edge disks of the array; corresponding C_T and induction factors a are also presented.

Contours of array C_P are shown in Fig. 2.3a as a function of K_1 and K_2. This clearly shows the trend that a uniform resistance coefficient across the array is required to achieve optimal performance. However, the simulations also show that operating slightly away from the optimal condition leads to only slightly sub-optimal

performance, e.g. for $K_1/K_2 = 1.2$ or $K_1/K_2 = 0.8$, the array $C_{P\max}$ is reduced by less than 0.25 %. Fig. 2.4 shows C_P, C_T, and the induction factor, a, corresponding to (approximately) the maximum array C_P for each of the tuning ratios K_1/K_2. At higher K_1/K_2, e.g. 1.6, the inboard thrust is higher resulting in reduced mass flow rate (increased axial induction) and a net reduction in the C_{Pd} of the inboard disk to less than the outboard disk. At $K_1/K_2 = 0.6$, flow 'leaks' through the centre of the array with too little resistance, the inboard disk produces more power, but lower mass flow rate and power at the outboard disk reduces the overall array power. To operate the array at its $C_{P\max}$, i.e. $K_1/K_2 = 1$, the turbines at the centre of the array have higher C_{Pd} and C_{Td} and a lower induction factor (greater mass flow rate) than the turbines at the ends of the array. From a structural point of view, the location of uniform thrust across the array (equal C_{Td} at the inboard and outboard disk) is of interest. For a uniformly loaded fence $K_1/K_2 < 1$ and the inboard C_{Pd} exceeds the outboard C_{Pd} by 3.5% for the current configuration, compared to 1.9% at $K_1/K_2 = 1$, but the array $C_{P\max}$ is just 0.1% less than the optimum array with $K_1/K_2 = 1$.

As well as maximising the array C_P, it is also desirable that tidal turbine installations should aim to maximise the power extractable by the turbines compared to the total power lost in the flow due to the presence of the turbines. As noted by Garrett & Cummins [28], this ratio is always less than unity due to the necessary wake mixing between the faster bypass flow and the slower core flow through the turbines. The total power removed from the flow can be calculated using control volume analysis of energy and momentum over the entire channel, from the far upstream to the far downstream location where the wake is fully remixed (beyond the simulation domain). In the current study where the free surface cannot deform, the velocity, and thus momentum fluxes at the far upstream and far downstream boundaries are equal. The thrust of the turbines is balanced by the difference in pressure between the far upstream and far downstream locations. The ratio of power extractable by the turbines to total power removed from the flow is therefore:

$$\eta = \frac{C_P A \frac{1}{2} \rho U_\infty^3}{C_T A \frac{1}{2} \rho U_\infty^2 \times U_\infty} = \frac{C_P}{C_T} \tag{2.16}$$

which has been referred to in the literature as 'basin efficiency' (e.g. [34]) or 'farm efficiency' [75]. The basin efficiency at the maximum array C_P for each of the tuning ratios K_1/K_2 is not shown here but may be inferred from C_P and C_T plotted in Fig. 2.4. It is found to vary only slightly between 0.559 and 0.564 for $0.6 \leq K_1/K_2 \leq 1.6$, with the highest value at $K_1/K_2 = 1$. For comparison, the basin efficiency of an

isolated turbine in a very large (infinite) channel, corresponding to the Betz limit, is 2/3.

2.4.2 Tuning a row of eight turbines

The previous experiment was repeated for a longer array of eight turbines. The computational domain was widened to maintain the same global blockage as in the four turbine array case and again made use of the symmetry of the flow domain about the $y = 0$ and $z = 0$ planes. Analogously to the four turbine array, K was varied across the four disks in the computational domain. A linear tuning distribution is initially investigated, i.e. $K_i = K_{\text{edge}} + (K_{\text{centre}} - K_{\text{edge}}) * (n_{\text{sim}} - i)/(n_{\text{sim}} - 1)$ where K_{centre} controls the two turbines at the centre, and K_{edge} the turbines at the edge of the array, and $i = 1..4$, where $n_{\text{sim}} = 4$, specifies the turbine from the edge to the centre of the array in the simulation domain. The results will show that the choice of a linear variation (as opposed to some other non-linear variation) is unimportant.

Fig. 2.3b shows that the array $C_{P\max}$ was again achieved using uniform K across the array. The eight turbine array was found to have an array $C_{P\max} = 0.864$ compared to $C_{P\max} = 0.841$ for the four turbine array at the same global blockage $B = 0.039$ and the same intra-turbine spacing $s/D = 0.25$. The model of [54] predicts $C_{P\max} = 0.832$ for the current blockage and disk spacing assuming a wide array. For smaller arrays, $C_{P\max}$ will tend back to the Garrett & Cummins result of $C_{P\max} = 0.642$. The present numerical results agree with this trend (note, however, that the $C_{P\max}$ values obtained in the current study are higher due to the effect of free-stream turbulence). While the results of the four turbine array already showed that (for the array $C_{P\max}$ condition) the turbines at the centre of the array were subjected to a higher thrust and produced more power than the turbines at the edge of the array, the results of the current case indicate how this trend continues for wider arrays.

The disk-averaged values of C_{Pd}, C_{Td} and a_d are shown in Fig. 2.5 corresponding to the maximum array C_P for $K_{\text{centre}}/K_{\text{edge}} = 0.8$, 1.0 and 1.2. As concluded from the four turbine array case, for uniform K and at $C_{P\max}$, the turbines at the centre of the array have higher C_{Pd} and C_{Td}, and lower induction factors (higher velocity) than the turbines at the edge of the array. Using $K_{\text{centre}}/K_{\text{edge}} = 0.8$, i.e. attempting to increase the loading of the outboard disks, the mass flow rate through the outboard disks falls rapidly (increase of a_d) such that the outboard disks produce less power. The power distribution is still highest at the centre and lowest at the edge. Therefore it may seem advantageous to increase the loading on the inboard disks,

using $K_{\text{centre}}/K_{\text{edge}} = 1.2$, but this leads to a decrease in mass flow rate and C_{Pd} at the centre so that the overall array C_P is reduced. For the linear tunings tested, the distribution of C_{Pd} across the array could be made either more or less uniform, but this always resulted in a lower array C_P. Using the current linear tuning across the array, it was not possible to create a more uniform distribution of C_{Td} across the array than achieved with uniform K. Although not shown here, a more uniform thrust distribution may be achieved by using a slightly increased K only for the end turbine. However, this did not improve the array C_P. These conclusions are in agreement with the condition for uniform thrust in the four disk array.

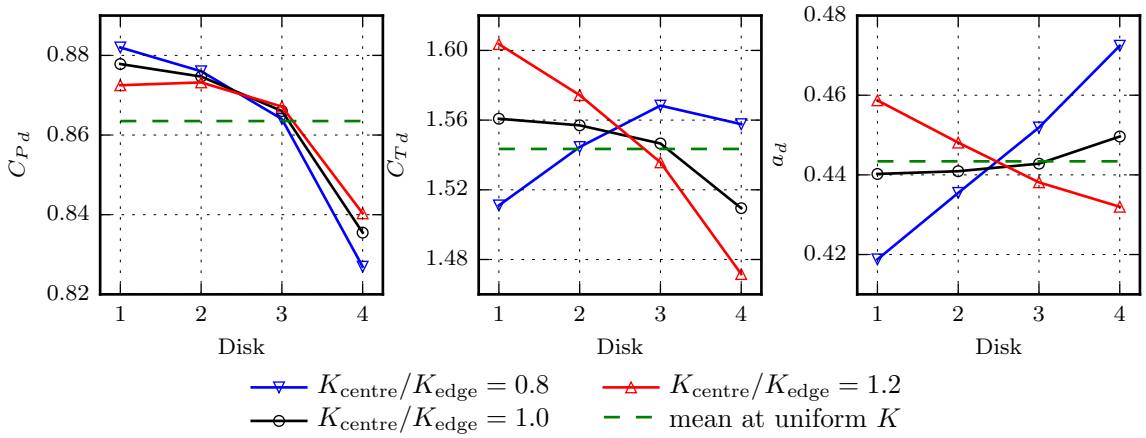


Figure 2.5: Disk averaged values of C_{Pd}, C_{Td} and a_d corresponding to the maximum array C_P for three tuning ratios $0.8 \leq K_{\text{centre}}/K_{\text{edge}} \leq 1.2$. Disks 1 and 4 are the inboard (centre) and outboard (edge) disks, respectively.

2.4.3 Effect of staggering a row of seven turbines

A further mesh was created to model seven turbines at the centre of the domain. The global blockage and lateral intra-turbine spacing were unchanged from the previous two cases at $B = 0.039$ and $s = 0.25D$. The actuator disk boundary conditions were assigned in the mesh to allow the disks to be staggered with streamwise spacings $\xi = 0.25D, 0.5D, 0.75D$ and $1D$ downstream of the $x/D = 0$ plane. In the results shown here, four equally spaced turbines including the ends of the array were left at the upstream $x/D = 0$ plane ("front row"), while the remaining three equally spaced turbines were placed uniformly at various downstream locations ("rear row"). As a result, the intra-turbine spacing in each sub-array became $s_{\text{sub}} = 2s + D = 1.5D$. Again, due to the symmetry of the flow domain about the $y/D = 0$ and $z/D = 0$

planes, only a quarter of the physical domain was simulated. The computational domain of the array is shown schematically in Fig. 2.6.

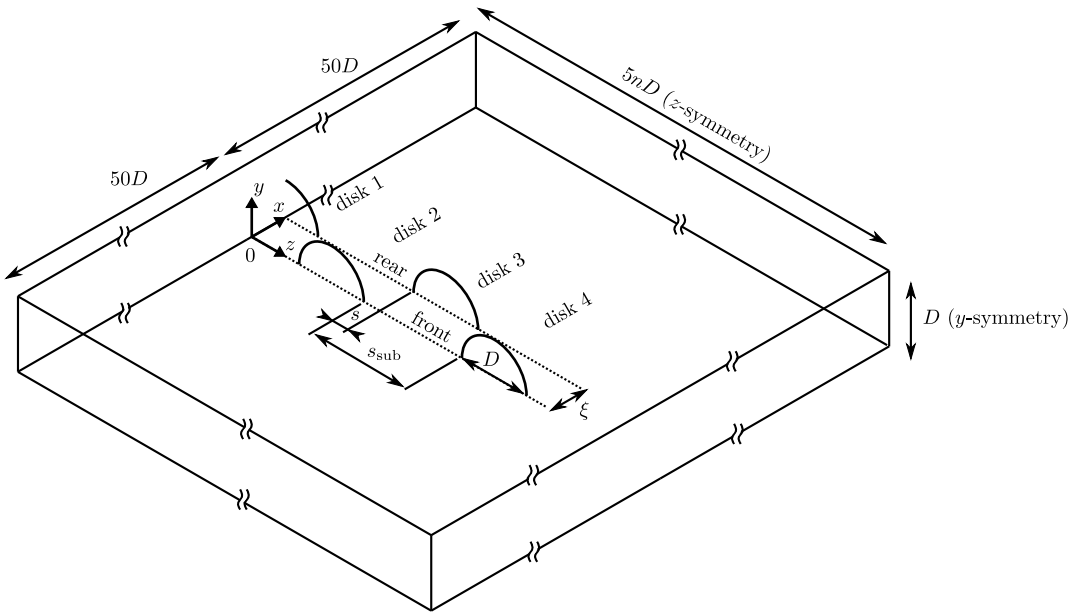


Figure 2.6: Schematic diagram of the computational domain for the seven disk staggered array (cf. physical and computational domain in Figure 2.1).

Motivated by the results of Section 2.4.1, initially, a uniform value of K was used across the turbine fence, and for both rows. Fig. 2.7a shows the mean array C_P at a range of K values, where each symbol is the result of a simulation case, as well as the locus of $C_{P\max}$. The highest array $C_{P\max}$ is achieved by the non-staggered array ($\xi/D = 0$) and decreases monotonically with increasing streamwise spacing. Using C_T, as plotted in Fig. 2.7b, the efficiency, η (Eq. 2.16), can be calculated. Fig. 2.7c plots the relationship between the mean array C_P and η, showing that the non-staggered array produces the most power for a given efficiency. These trends are in agreement with the ranking of turbine arrangements based on the model of [16], i.e. that a single row of $2N$ turbines has a higher array $C_{P\max}$ than a staggered

array with two sub-arrays of N turbines, which in turn has a higher $C_{P\max}$ than a staggered array with large streamwise spacing of the sub-arrays. This suggests that the assumptions made in the analytical model, while they may lead to inaccuracies, are not fundamentally wrong.

In Fig. 2.8, the array $C_{P\max}$ values are plotted together with the mean C_P of each row, for a range of ξ/D. As postulated in the introduction to this chapter, the rear row does achieve a higher mean C_P, benefiting from the faster bypass flow of the upstream row of disks until $\xi/D \approx 0.5$. C_P then begins to decrease as ξ/D is further increased, the approach flow to the downstream row of turbines is more able to divert around the rear disks, which benefit less from the accelerated bypass flow of the upstream row of disks. At the same time, however, the mean C_P of the front row drops as the local blockage in the front row is reduced by staggering the array until $\xi/D \approx 1.0$. This can be interpreted as a reduction in the effective blocking presence of the downstream row. At $\xi/D > 1$ however, the downstream row is simply an obstruction and C_P of the front row begins to increase again as the rear row is placed further downstream. Therefore both the front and rear row tend to independent behaviour by $\xi/D = 4$. In total, the array $C_{P\max}$ is lower than that of the non-staggered array at all sub-array spacings $\xi/D > 1$.

The increased power production at the rear row was also reported recently by Malki et al. [44], who used RANS embedded blade-element momentum (BEM) simulations of a staggered array of three turbines. Compared to the current study using ideal actuator disks to investigate the limit of power extraction, the RANS embedded BEM method can be used to study the performance of more realistic rotors. At comparable intra-turbine spacing ($s_{\text{sub}}/D = 1$ and 2), similar trends are seen for the C_P of the turbine in the rear row. In their study the channel width and height were $W = 10D$ and $H = 3D$, leading to a higher global blockage of 0.079, but lower local blockage effects due to the small number of turbines in the array and the absence of multiple rotors in the rear sub-array The absolute performance of the turbines in the RANS embedded BEM study is also lower due to the turbine model.

While C_P, as defined in Equation 2.14, is the power coefficient averaged over the disk, Fig. 2.9 shows the variation of the local C_P over the turbine fence at $K = 4.5$ (close to $C_{P\max}$ for $\xi/D = 0..1$). The contours are normalised by $C_{P\max}$ for the non-staggered array, which is hereafter referred to as $C_P{}^*$. For the non-staggered row, it is clear that the turbines at the ends of the fence produce less power due to lower local blockage at one side. As the array is staggered, the turbines in the front row produce less power compared to the non-staggered case. For a small streamwise

spacing $\xi/D = 0.25$, for example, it is observed that the local C_P across the inner two disks of the front row ($z/D = \pm 1.25$) is similar in magnitude to that experienced by the end disk in the non-staggered fence. For $0.25 \leq \xi/D \leq 1.0$, C_P of the front row continues to decrease, cf. Fig. 2.8.

Contours of static pressure on the centre-plane through the disks at $y/D = 0$ are shown in Fig. 2.10. The streamlines passing each side of the disk in this plane indicate the streamwise evolution of the stream-tube for each turbine. These plots show qualitatively that for the staggered cases, the pressure drop over the turbines (or equivalently, the axial thrust that each turbine imposes on the flow) is higher at the rear row and lower at the front row, compared to the non-staggered array (note the differences in pressure immediately downstream of each turbine).

2.4.4 Tuning the staggered array of turbines

While the results of Sections 2.4.1 and 2.4.2 indicate that a uniform tuning of K is required to achieve the highest array $C_{P\text{max}}$ for a non-staggered array of turbines, the following results show that, for a staggered array, a slightly higher array $C_{P\text{max}}$ may be achieved by tuning the front and rear rows differently. This is unsurprising as the more flow that is diverted around the front row, the greater the energy flux approaching the rear row.

Fig. 2.11 shows the array C_P against the front and rear row operating conditions, K_{front} and K_{rear}; the maximum mean power output for this staggered array is achieved close to an optimum ratio of $K_{\text{rear}}/K_{\text{front}} = 0.8$. Operating with a higher K_{front} and lower K_{rear} causes the front array to divert more flow onto the rear row in bypass flow. However, the maximum value $C_{P\text{max}} = 0.852$ achieved is still less than the ${C_P}^* = 0.856$ for the non-staggered case ($\xi/D = 0$). Additionally, inspection of the contour values shows that this new maximum represents less than half a percent increase compared to the staggered case with the same value of K for both rows ($C_{P\text{max}} = 0.850$). Conversely, this also shows that slightly staggering an array of turbines in two rows, spaced $\xi/D = 0.25$ apart, results in only a small reduction of the array $C_{P\text{max}}$, especially if the front and rear rows are tuned, i.e. operated at different values of K.

The effect on the maximum array C_P of differential tuning of the front and rear rows at $\xi/D = 0.25$, for each tuning ratio $K_{\text{rear}}/K_{\text{front}}$, and the corresponding C_T and induction factors are shown in Fig. 2.12. The optimal tuning for the staggered array, $K_{\text{rear}}/K_{\text{front}} = 0.8$, compared to a uniform tuning for both rows results in a greater difference in the power produced by the front and rear rows, but reduces the

difference in thrust between the two rows. Increasing the rear array thrust from this optimum, i.e. towards $K_{\text{rear}} = K_{\text{front}}$, leads to reduced flow speed through the rear disks and greater flow speed and reduced thrust supported by the front disks. The power gains made by the front row are however offset by the greater power loss of the rear row. The optimum overall array $C_{P\max}$ is achieved when the disks of the front row are used as blockers to divert the flow onto the rear row.

As discussed previously, the rear row ($z/D = 0$ and ± 2.5) extracts more power per disk area than the front row ($z/D = \pm 1.25$ and ± 3.75). An effect of tuning the staggered array, with its optimal tuning ratio of $K_{\text{rear}}/K_{\text{front}} = 0.8$, is to develop a more uniform thrust across the array. While tuning results in only a modest increase in C_P, the resulting more uniform thrust distribution across the array may also be beneficial from a viewpoint of the structural design of the turbines. Equal thrust at the front and rear rows is achieved at $K_{\text{rear}}/K_{\text{front}} \approx 0.73$ and results in a greater difference between front and rear row power output compared to the optimum case, along with a very small reduction of overall array $C_{P\max}$.

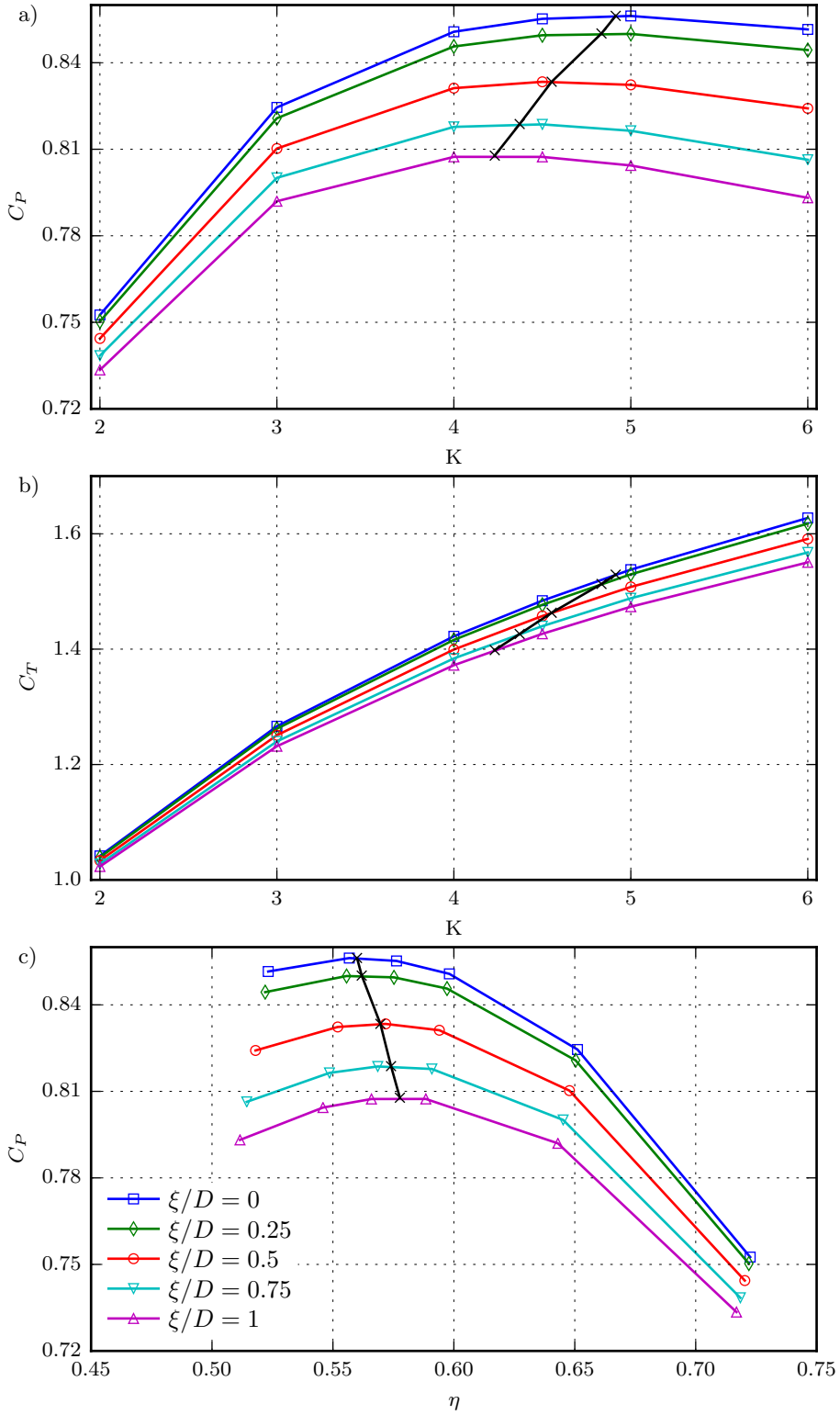


Figure 2.7: Array performance in terms of C_P, C_T and η at a range of operating conditions (using uniform K for all turbines) for row separations $\xi/D = 0..1$. The black crosses indicate the locus of $C_{P\max}$ with respect to row stagger.

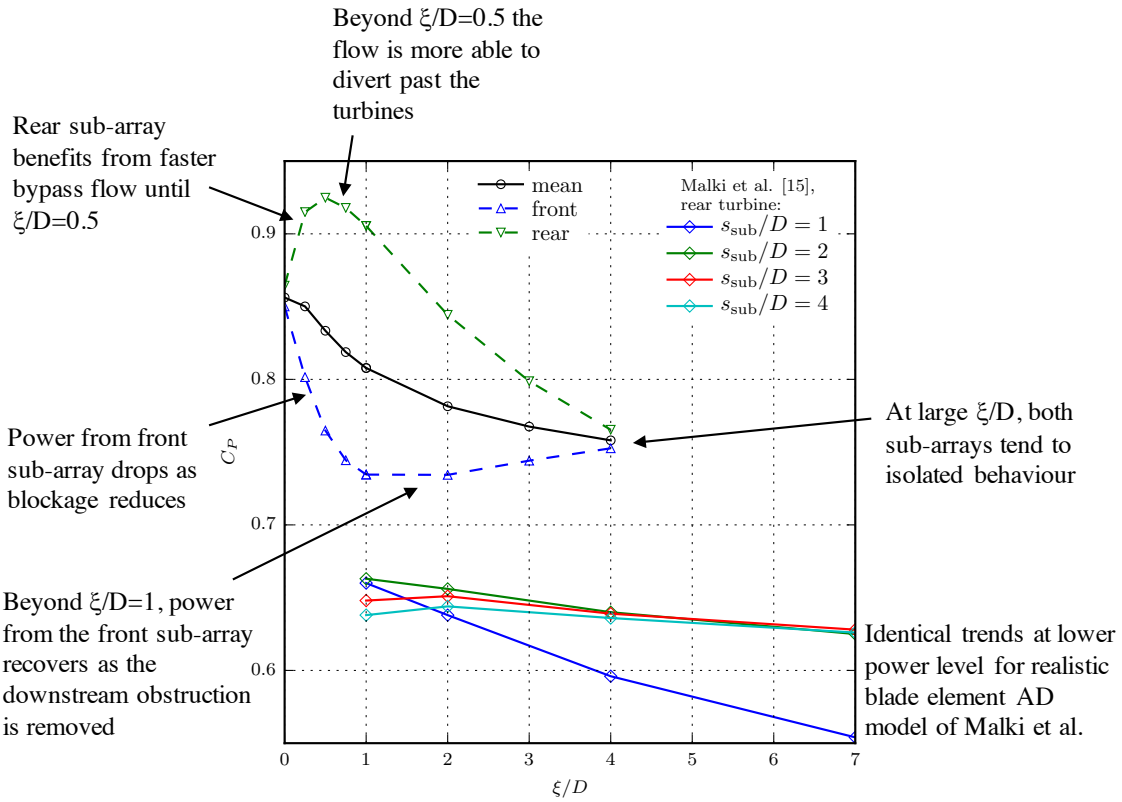


Figure 2.8: Contribution to the mean array $C_{P\max}$ from the front and rear sub-arrays for an extended range of sub-array spacing ξ/D (for fixed intra-turbine spacing in sub-arrays, $s_{\text{sub}}/D = 1.5$). Also plotted are RANS-BEM results of Malki et al. [44]: C_P of the rear turbine of a three rotor array at $s_{\text{sub}}/D = 1..4$.

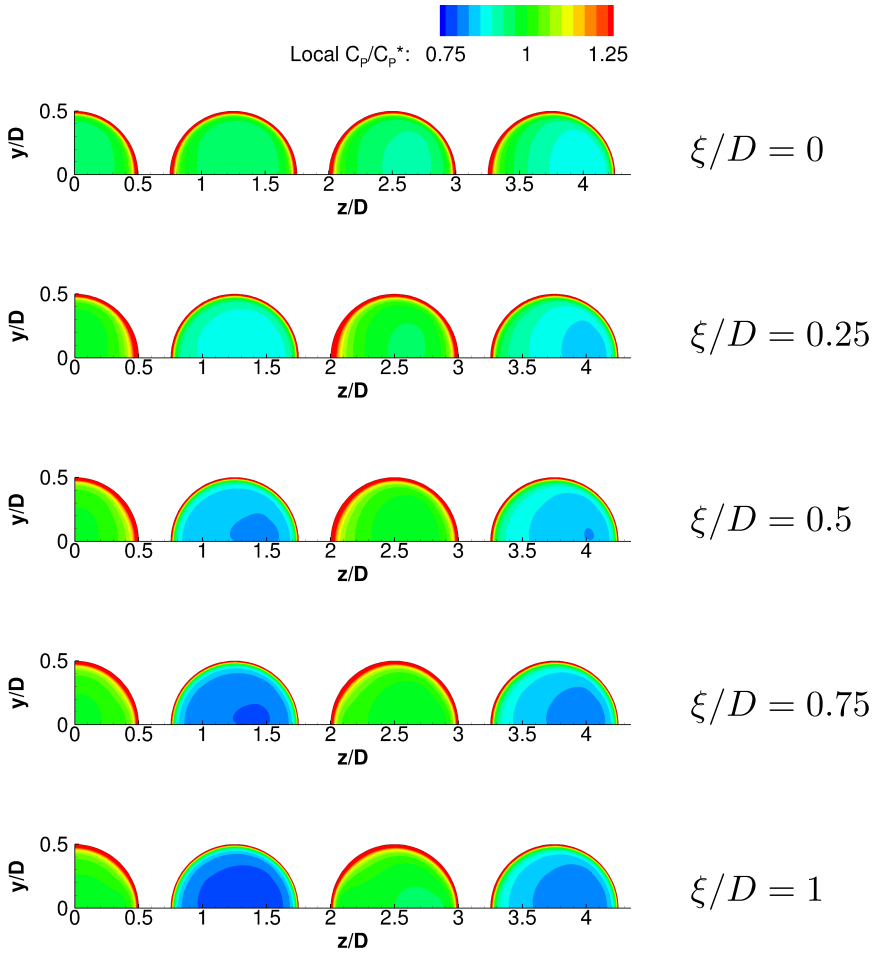


Figure 2.9: Variation of local C_P (normalised by $C_P{}^* = C_{P\max}$ for the non-staggered array) over the fence for $K = 4.5$; from top to bottom: $\xi/D = 0, 0.25, 0.5, 0.75$ and 1. Note that the disks centred at $z/D = 0$ and ± 2.5 are in the rear row, whilst those at $z/D = \pm 1.25$ and ± 3.75 are in the front row.

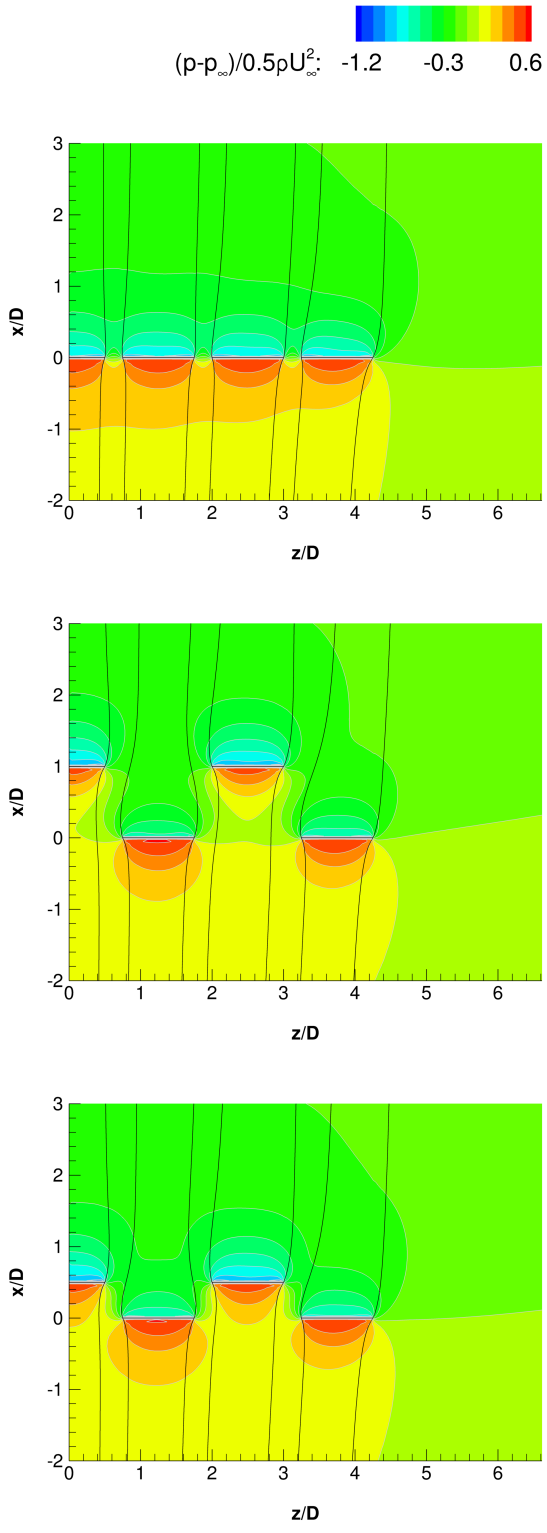


Figure 2.10: Contours of pressure coefficient $(p - p_\infty)/\frac{1}{2}\rho U_\infty^2$, where p_∞ is the far upstream static pressure, and streamlines on the centre-plane through the disks, $y/D = 0$ for $K = 4.5$. Streamwise row separations, from left to right: $\xi/D = 0, 0.5$, and 1. Flow is up the page in the positive x direction.

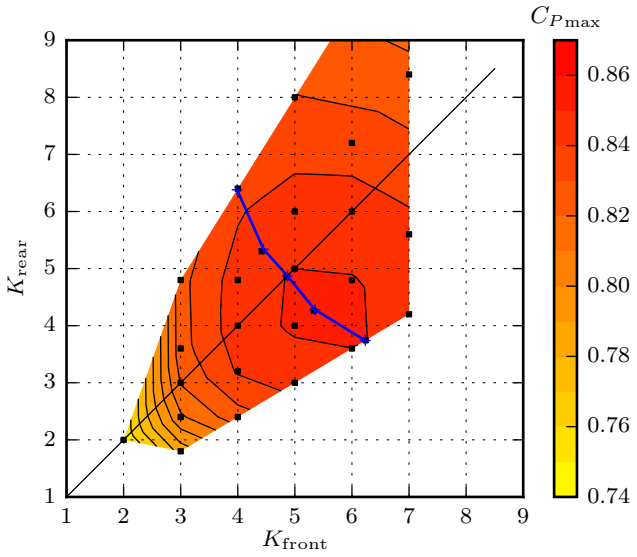


Figure 2.11: Array C_P for different front and rear row disk tunings at $\xi/D = 0.25$. Squares indicate simulated cases; the locus of $C_{P\max}$ for a given $K_{\text{rear}}/K_{\text{front}}$ is indicated by the blue crosses.

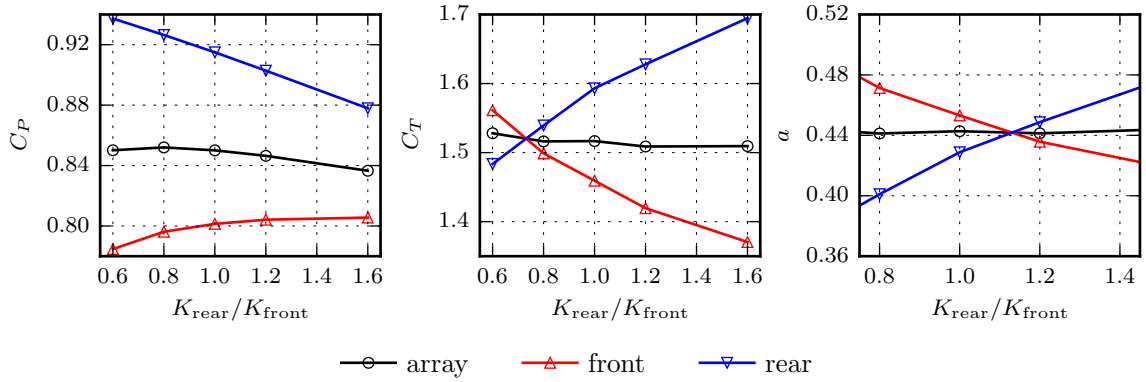


Figure 2.12: $C_{P\max}$ for each $K_{\text{rear}}/K_{\text{front}}$, showing contributions to the mean from the front and rear rows of the array; corresponding C_T and induction factor a are also presented. Streamwise staggering, $\xi/D = 0.25$, (cf. Figure 2.6).

2.5 Conclusions

In this study, 3D incompressible RANS computations of the water flow past arrays of tidal turbines, modelled as actuator disks, were performed using a CFD solver. Although analytical models exist to predict the performance of a full (homogeneous) array of turbines across a channel cross-section (e.g. [28], [74], [75]) and of a partial array (e.g. [51], [54]), these models consider only uniform tuning of the turbines across the entire array. One of the objectives in this numerical study was therefore to investigate the effect of tuning non-uniformly the resistance coefficient, K, of actuator disks across four and eight turbine arrays. By evaluating the array C_P for a wide range of tunings, it was found that the highest array $C_{P\max}$ is achieved by uniform K across the array. Uniform tuning of K across the array results in a non-uniform distribution of C_{Pd} and C_{Td}, both of which are higher towards the centre of the array, and lower at the edges.

This study has also examined the effect of staggering an array of uniformly tuned turbines. Specifically, the second, fourth and sixth turbines of an array of seven turbines were moved into a row $0.25D, 0.5D, 0.75D$ and $1D$ downstream of the front row. At the array $C_{P\max}$, the rear row has a higher mean C_P benefiting from the faster bypass flow of the front row, while the C_P of the front row reduces due to the lower local blockage compared to the non-staggered array. Importantly, the array $C_{P\max}$ (i.e. averaged across all turbines in the front and rear rows) was found to decrease with increasing streamwise spacing and was always less than the value achieved by the non-staggered array. Also for a given efficiency, the non-staggered array was found to produce the most power. These trends are consistent with a ranking of turbine arrangements presented in [16].

While uniform tuning of K was required to achieve the highest array $C_{P\max}$ for a non-staggered array of turbines, the highest array $C_{P\max}$ for a staggered array was achieved by operating the front row at a higher value of K than the rear row. For a streamwise spacing of $\xi/D = 0.25$, for example, the array $C_{P\max}$ slightly increased from 0.850 for the uniform K case to 0.852 for the separately tuned case, but this was still below the non-staggered array $C_{P\max} = 0.856$.

These results suggest that the best strategy to maximise the power extraction by a given number of turbines is to arrange them in a non-staggered array (with an optimal intra-turbine spacing that can be estimated analytically), and operate them with a uniform flow resistance coefficient across the entire array, which equates to a non-uniform loading distribution. It should be remembered, however, that this

study employed ideal actuator disks to model turbines and also neglected the effects of vertical shear of the flow and seabed friction.

Chapter 3

General actuator disk for RANS using blade element theory

The previous chapter detailed simulations with tidal turbines modelled using a simple Actuator Disk (AD), which produced a step-wise change in static pressure proportional to the square of the local normal velocity. Implemented in CFD, this means a pressure jump between the upstream and downstream cells sharing a face on the disk where the boundary condition is implemented. As the model is parametrised entirely by an inertial coefficient K, it contains no information specific to the rotor design or operation. The model is defined theoretically and therefore requires no validation, verification of its correct implementation is assumed in ANSYS® Fluent®. However it is also simple enough that comparisons can be made with LMADT. The most intuitive variables to compare are the axial induction, thrust and power coefficients, which vary with the parameter K. Comparisons like these have been made e.g. by Nishino & Willden [50], which show good agreement with the analytical model, but also identify the effect of aspect ratio and free-stream turbulence levels, which are not accounted for in LMADT.

The simple AD is useful for parametric studies on the theoretical performance of turbines in various array configurations, as demonstrated by Nishino & Willden [54][53], Draper & Nishino [16], Hunter et al. [35]. However, it cannot represent any aspects of the rotor design or practical rotor operation. This chapter presents the development of a general AD for RANS, which uses blade element theory to include the aerodynamic performance of actual rotor blade sections. The chapter begins with a review of blade element theory including various theoretical and semi-empirical corrections that have been suggested, leading to a description of the current implementation. The general model uses rotor geometry and operating conditions as input so validation is essential. The second section discusses potential options for validating the model

and describes a set of experiments, which are used to compare with results from the model. Results are presented in the third section to demonstrate grid convergence of the simulations and to compare simulation results with experimental results for a range of operating conditions and modelling options. The chapter is concluded with a discussion.

3.1 Blade element theory

Blade element theory was introduced as the linkage between the general momentum theory of a propeller and the aerodynamic characteristics of a real rotor. The resulting blade element momentum method was described by Glauert [30] in the form, which continues to be the principal tool for design and evaluation of rotors for wind turbines [66]. In order to explain how the blade element theory has been interpreted to be incorporated as a boundary condition in a RANS CFD solver, the BEM method is derived again here. The current implementation follows the suggestions of Shen et al. [62] and [63], and the following derivation differs only in the method of imposing the induced rotational velocity.

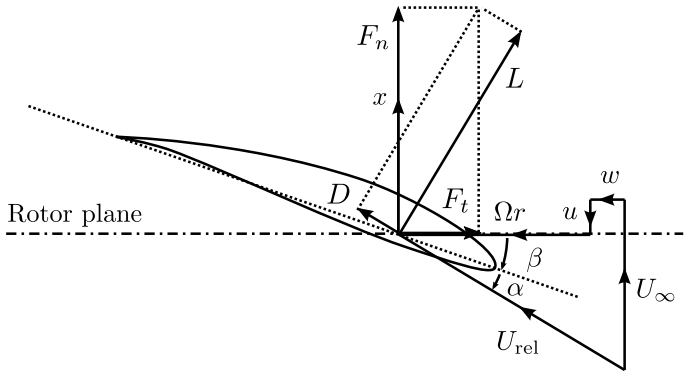


Figure 3.1: Blade element diagram at radial position r, velocities shown in blade frame of reference.

For a rotor with N identical blades, it is assumed that the aerodynamic forces acting on a radial element δr may be described by suitable lift and drag coefficients of the aerofoil section at radius r. The blade element shown in Figure 3.1 can be interpreted as a cross-section through a turbine rotor blade, parked at the top of the revolution ($\theta = 0\,\text{deg}$), of a rotor rotating in the positive sense about the (streamwise) x-direction. U_∞ is the upstream velocity, there is no rotational component far upstream of the disk. Due to the rotation of the rotor, the blade element experiences a tangential relative velocity equal in magnitude to the rotation of the rotor, Ωr,

but in the opposite direction. The effect of the rotor is to decelerate the axial flow and cause a rotational velocity component downstream of the rotor in the opposite direction to its rotation. These two effects are quantified by the induced axial and rotational velocities, u and w. The term 'induction' is maintained from the classical description of the flow field about a rotor using various levels of approximation of the vorticity present. The relative velocity magnitude at the blade element U_{rel} can be expressed as

$$U_{\text{rel}} = \sqrt{[U_\infty(1-a)]^2 + [\Omega r(1+a')]^2} \tag{3.1}$$

where the axial and rotational induction factors at the blade have been introduced as

$$u = aU_\infty \tag{3.2}$$

$$w = a'\Omega r \tag{3.3}$$

The blade element is pitched at an angle β to the plane of rotation, and the effective angle of attach, α, is calculated as $\alpha = \phi - \beta$, where ϕ is the flow angle between the resultant relative velocity and the plane of rotation.

$$\phi = \tan^{-1}\left[\frac{U_\infty(1-a)}{\Omega r(1+a')}\right] \tag{3.4}$$

The relative flow results in an aerodynamic lift and drag force experienced by the blade element, L and D, which can be decomposed into force components normal and tangential to the plane of rotation, F_n and F_t. Given the relative velocity U_{rel} of the flow to the blade element and its angle relative to the plane of rotation ϕ, the forces experienced by the blade element can be resolved into the axial and tangential direction:

$$F_n = L\cos\phi + D\sin\phi \tag{3.5}$$

$$F_t = L\sin\phi - D\cos\phi \tag{3.6}$$

Then differential elements of thrust, $\mathrm{d}T$, and torque, $\mathrm{d}Q$, acting on the rotor element of length $\mathrm{d}r$ can be expressed as

$$\frac{\mathrm{d}T}{\mathrm{d}r} = ZF_n = \frac{1}{2}Zc\rho U_{\text{rel}}^2 C_n \tag{3.7}$$

$$\frac{\mathrm{d}Q}{\mathrm{d}r} = ZrF_t = \frac{1}{2}Zcr\rho U_{\text{rel}}^2 C_t \tag{3.8}$$

where force coefficients C_n and C_t have been introduced, c is the local chord length, Z is the number of blades and ρ is the density. It is readily seen from Figure 3.1 that

$$\sin\phi = \frac{U_\infty(1-a)}{U_{\text{rel}}} \tag{3.9}$$

$$\cos\phi = \frac{\Omega r(1+a')}{U_{\text{rel}}} \tag{3.10}$$

which can be rearranged to yield

$$U_{\text{rel}}^2 = \frac{U_\infty^2(1-a)^2}{\sin^2\phi} = \frac{U_\infty(1-a)\Omega r(1+a')}{\sin\phi\cos\phi} \tag{3.11}$$

This allows Eqs. 3.7 and 3.8 to be expressed in terms of the blade induction factors

$$\frac{\mathrm{d}T}{\mathrm{d}r} = \frac{\rho Z c U_\infty^2(1-a)^2}{2\sin^2\phi} C_n \tag{3.12}$$

$$\frac{\mathrm{d}Q}{\mathrm{d}r} = \frac{\rho Z c U_\infty(1-a)\Omega r^2(1+a')}{2\sin\phi\cos\phi} C_t \tag{3.13}$$

The analytical BEM method would then equate the differential thrust and torque to expressions from general momentum theory for an AD

$$\frac{\mathrm{d}T}{\mathrm{d}r} = \int_0^{2\pi} \rho U_D(U_\infty - U_{\text{wake}}) r \mathrm{d}\theta \tag{3.14}$$

$$\frac{\mathrm{d}Q}{\mathrm{d}r} = \int_0^{2\pi} \rho U_D U_{\theta,\text{wake}} r^2 \mathrm{d}\theta \tag{3.15}$$

where U_D is the axial velocity at the disk, U_{wake} is the axial velocity far downstream of the disk where the pressure has recovered to its upstream value, but before any wake mixing has occurred, and $U_{\theta,\text{wake}}$ is the rotational velocity just downstream of the actuator. Using results from general momentum theory for an AD, these velocities can be expressed using induction factors as in Eqs 3.2 and 3.3:

$$U_D = U_\infty(1-a) \tag{3.16}$$

$$U_{\theta,\text{wake}} = 2\Omega r a' \tag{3.17}$$

$$U_{\text{wake}} = U_\infty(1-2a) \tag{3.18}$$

Carrying out the integration of Eqs. 3.14 and 3.15 results in

$$\frac{\mathrm{d}T}{\mathrm{d}r} = 4\pi r \rho U_\infty^2 \overline{a}(1-\epsilon_1\overline{a}) \tag{3.19}$$

$$\frac{\mathrm{d}Q}{\mathrm{d}r} = 4\pi r^3 \rho \Omega U_\infty \overline{a'}(1-\epsilon_2\overline{a}) \tag{3.20}$$

where $\overline{\bullet} = \frac{1}{2\pi}\int_0^{2\pi} \bullet \,\mathrm{d}\theta$, while $\epsilon_1 \equiv \overline{a^2}/(\overline{a}\,\overline{a})$ and $\epsilon_2 \equiv \overline{aa'}/(\overline{a}\,\overline{a'})$ are assumed to be unity. Equating Eq. 3.12 to 3.19 and Eq. 3.13 to 3.20 results in two equations for thrust and torque to solve for four unknown induction factors, a, a' and their annulus-average means $\overline{a}$ and $\overline{a'}$ at an arbitrary number of radial stations. The system is made

solvable again by introducing a relationship between the induction at the blade and the annulus-average values.

$$F = \overline{a}/a = \overline{a'}/a' \tag{3.21}$$

In the case of a turbine, it is intuitive that the flow is not equally decelerated over the swept area of the rotor, fluid in the vicinity of the blades will experience higher induction, while fluid between blades will maintain a higher axial velocity. In the theoretical limit of a rotor with an infinite number of blades, $F \to 1$, but in the general case of a rotor with a finite number of blades, the factor F is unknown and less than unity. Glauert [30] demonstrated that the result obtained by Prandtl [6] for the circulation distribution on a rotor with minimum induced drag, and finite number of blades, can be used to find F, as defined in Eq 3.21. It is found that the function F lies between 0 and 1, being close to 1 across most of the disk and dropping to 0 towards the edge of the disk. The factor has become known as Prandtl's tip loss factor and is calculated as

$$F = \frac{2}{\pi}\cos^{-1}\left[\exp\left(\frac{Z(1-R/r)}{2\sin\phi}\right)\right] \tag{3.22}$$

The blade elemental thrust and torque, Eqs. 3.12 and 3.13 are naturally expressed in terms of the blade induction factors following Figure 3.1, while the integral momentum and moment of momentum balance in Eqs. 3.14 and 3.15 may be written terms of annulus-averaged induction factors. In the most common application of the Prandtl factor, the induced axial and rotational velocity in Eqs. 3.19 and 3.20 are corrected to blade induction factors but the mass flow rate through the disk is left uncorrected. This proves to be an accurate approximation[11] and leads to a simple set of equations for the axial and rotational blade induction factors as

$$a = \frac{1}{\frac{4F\sin^2\phi}{\sigma C_n} + 1} \tag{3.23}$$

$$a' = \frac{1}{\frac{4F\sin\phi\cos\phi}{\sigma C_t} - 1} \tag{3.24}$$

where the rotor solidity $\sigma = \frac{Zc}{2\pi r}$ has been introduced. Following Hansen [33], the solution can proceed iteratively as follows:

1. Initialise a and a'.
2. Compute the local angle of attack α using the velocity triangle.
3. Read tabulated $C_L(\alpha)$ and $C_D(\alpha)$.
4. Compute new a and a' from Eqs. 3.23 and 3.24.

3.1.1 Correction for finite number of blades

The tip-loss factor F introduced in Eq 3.21 is derived from the solution to the more general problem of maximizing the efficiency of a wind turbine rotor. This problem was formulated by Betz [6] as finding the optimum circulation distribution along a rotor blade to minimize induced drag. The problem is analogous to finding the circulation distribution required to minimize induced drag for a finite wing, which was solved by Munk [48] in the framework of Prandtl's lifting line method. For the finite wing, the exact solution corresponds to uniform downwash across the span of the wing and is achieved by a straight wing with elliptic planform, a result which features in every modern introduction to incompressible aerodynamics, e.g. [38]. Betz showed that the analogous solution for a rotor with infinite blades is given when the wake of trailed vortices follows a helical path of constant pitch. For a discrete number of blades, shedding a discrete number of helical vortex sheets, the circulation distribution on each blade, Γ, is different to the ideal radial distribution of the Betz rotor. If the total circulation for a Betz rotor is Γ_∞, then the supposed circulation about each of the infinite number of blades is Γ_∞/Z and the factor F is interpreted as:

$$F = \frac{\Gamma}{\Gamma_\infty/Z} \tag{3.25}$$

An exact solution to this problem proved difficult to obtain, but Prandtl demonstrated that a simple solution can be found for an approximation of the problem. This is the result given in the appendix of the work by Betz [6], which was subsequently reinterpreted by Glauert [30] in terms of induction factors, to be included in the BEM method. The historical development of this interesting and still active research area has been excellently summarised by Branlard [9][1].

3.1.2 Correction of 3D and rotational effects

3.1.2.1 Rotational augmentation and stall delay

As a first approximation, C_L and C_D might be assumed equal to the values for the given aerofoil section in quasi-2D flow. However, it turns out that suitable tables of drag and lift data have to be constructed to achieve acceptable accuracy when the blade elements are rotating. Experiments on propellers as early as the 1940s showed increased lift coefficients at and above the 2D stall angle of attack. Numerous CFD simulations of rotating blades have since confirmed both the increase in maximum C_L

[1] The author would like thank E. Branlard for private communication to discuss and clarify some of the details of his work.

and also the delay of stall until higher angles of attack, e.g. [71]. Since then, "stall-delay" and "rotational augmentation" have been the subject of a considerable amount of research, and a number of semi-empirical models have appeared which aim to correct 2D aerofoil data for use in the BEM method. The analytical foundation of the most widely used stall-delay models is given by solutions to the 3D integral boundary-layer equations for rotating flow. After non-dimensionalizing using the local chord and radius, the higher order terms are neglected, and a simpler system of equations almost representing the 2D integral boundary layer equations with additional terms for centrifugal and Coriolis forces results. Besides offering parameterized solutions which can be tuned to experiments, the analysis also provides a physical explanation of the differences between 2D and 3D stall on rotating blades. The following explanation is paraphrased from Snel et al. [64]: Significant radial flow occurs in separation regions on the suction side of the blade. Flow towards the tips develops resulting in a Coriolis force in the main flow direction, which acts as a favourable pressure gradient. This decreases the displacement thickness of the separated boundary layer, leading to higher lift coefficients.

The application of all models aiming to correct for this effect may be reduced to the following form:

$$C_{L,3D} = C_{L,2D} + f_L(C_{L,\text{inv}} - C_{L,2D}) \tag{3.26}$$

where $C_{L,2D}$ is the quasi-2D lift coefficient for a non-rotating aerofoil and $C_{L,\text{inv}} = 2\pi(\alpha - \alpha_0)$ where α_0 is the zero-lift angle (which can be non-zero for cambered aerofoils). In practice, the calculated or measured lift slope from the linear region of the $C_L(\alpha)$ polar is used instead of the theoretical value for a thin aerofoil of 2π.

One of the most widely used correction models of this type, and the one used in this study, is given by Du & Selig [19]. This model uses the integral boundary layer method together with assumed velocity profiles to estimate the separation point on the suction surface of the rotating blade. The form of f_L from Eq. 3.26 is assumed to be similar to the solution derived for the laminar separation point, with a number of calibration constants. The resulting equation is given as:

$$f_L = \frac{1}{\pi}\left[\frac{1.6(c/r)}{0.1267}\frac{a - (c/r)^{\frac{d}{\Lambda}\frac{R}{r}}}{b + (c/r)^{\frac{d}{\Lambda}\frac{R}{r}}} - 1\right] \tag{3.27}$$

where a, b, and d are constants, which are generally set to unity, and the modified tip speed ratio

$$\Lambda = \Omega R / \sqrt{U_\infty^2 + (\Omega R)^2} \tag{3.28}$$

3.1.2.2 Correction of aerodynamic drag

There is no consensus on the effect of rotation on the drag coefficient. The report of Snel et al. [64] concentrates solely on quantifying the effect of lift augmentation and does not use the analysis to make any predictions about the effect on the drag. The correction model of Du & Selig [19] states, without explanation that the increase in lift is accompanied by a decrease in drag, which implies a reduction in momentum thickness to accompany the reduced displacement thickness. They suggest a correction formula for the C_D, which differs from Eq. 3.27 only in one of the tuning coefficients, and in sign, ensuring a decrease for the corrected values. In their CFD simulations of the wind tunnel experiment of a wind turbine, Sorensen et al. [71] found lift and also drag augmentation. Other CFD and experimental studies, as well as numerous correction models, many based on various simplifications of the integral boundary layer method, present the same variety of results, e.g.[42]. It is certain that rotation has an effect on the drag coefficient, but it appears that this may be strongly dependent on the details of the rotor geometry near the hub and tips, preventing the development of general correction models.

3.1.2.3 Force correction for blade tips

Shen et al. [62] reviewed the implications of Glauert's application of the Prandtl tip correction to the BEM method and demonstrated inconsistent behaviour at the blade tip. It is argued that the aerodynamic force on the aerofoil should tend to zero at the tip because there is no surface to maintain the pressure difference between the pressure and suction side. Typically the flow angle at the tip ϕ_R is non-zero, as is evidenced by the downstream convection of the tip vortex. In a thorough limit analysis it is deduced that the force coefficients must tend to zero at a rate proportional to the Prandtl tip correction factor. A relation with a similar form to Eq 3.22 is proposed which is parameterized only by the number of blades Z and the tip-speed ratio, λ. Three coefficients are used to match computational and experimental distributions of normal force near the tip of a rotor for two separate wind turbine wind tunnel experiments. Ideally these coefficients will continue to be tested and adjusted as more experimental data, or increasingly, blade-resolved CFD simulation data becomes available.

The model is applied to produce resulting (superscript 'r') force coefficients as:

$$C_\bullet^r = F_1 C_\bullet \tag{3.29}$$

where • takes either 'n' or 't', indicating normal and tangential coefficients respectively, and the correction factor

$$F_1 = \frac{2}{\pi}\cos^{-1}\left[\exp\left(g\frac{Z(1-R/r)}{2\sin\phi}\right)\right] \tag{3.30}$$

where g is a coefficient which introduces the parameter dependency. It is given the following form:

$$g = \exp\left[-c_1(Z\lambda - c_2)\right] + c_3 \tag{3.31}$$

In Shen et al. [62], the fitting coefficients receive values of $c_1 = 0.125$, $c_2 = 21$ and $c_3 = 0.1$, awaiting further validation data.

Shen et al. [63] outlined the application of this correction to AD and actuator line models for RANS, and were able to show improved agreement with experimental results when using the correction.

3.2 Implementation of a general actuator disk for RANS

Embedded in a RANS CFD code, continuity and momentum conservation is provided by solving the Navier-Stokes equations. The resulting flow field is sampled at the location of the AD, to calculate U_{rel} and ϕ, which can be used, together with the rotor geometry and lookup tables for aerofoil data, to calculate C_n and C_t, which give the magnitude of the forces to be imposed on the flow. In the case of a general CFD solver the forces can be imposed as momentum source terms. A review of previous implementations of AD models in CFD solvers was given in the introduction to this thesis. The current implementation was motivated by ideas presented by McIntosh et al. [45] but the author wishes to point out that this is an entirely new implementation. ANSYS® Fluent® [1] provides a 'fan' boundary condition, which can be applied across internal faces in a region of the computational domain. The boundary condition allows imposing a pressure jump across each face, as well as a rotational velocity component on the downstream side of each face. The current general AD model is implemented by iteratively sampling the mean flow field to calculate the parameters to be passed to the 'fan' boundary condition. The normal velocity component, U_D immediately provides the mass flux through the AD, which is used to establish linear and angular momentum balances with the blade elemental forces. The axial momentum balance returns the pressure jump across the AD as

$$\Delta p = \frac{\frac{1}{2}\rho U_{\text{rel}}^2 Z c C_n}{2\pi r} = \frac{1}{2}\rho U_{\text{rel}}^2 \sigma C_n \tag{3.32}$$

The rotor solidity σ has been introduced as defined previously. Equating change in angular momentum to the torque forces of the blade elements in an annulus is expressed by

$$\delta Q = \frac{1}{2}\rho U_{\text{rel}}^2 Z c r C_t \delta r = r U_{\theta,\text{wake}} \rho U_D 2\pi r \delta r \tag{3.33}$$

which can be reformulated to return the rotational velocity to be imposed just downstream of the rotor

$$U_{\theta,\text{wake}} = \frac{\sigma U_{\text{rel}}^2 C_t}{2U_D} \tag{3.34}$$

Both Eqs. 3.32 and 3.34 assume that the blade element force is smeared around the annulus at that radial station, but the calculation is performed for every cell face on the AD, meaning that the model is not restricted to axisymmetric flow.

The mean axial induction at the disk, $\overline{a}$ can be calculated from the mean axial velocity returned by the solver U_D, using the definition in Eq 3.16. The rotational velocity at the disk-plane is not read from the flow field, but rather it is assumed to be half the value imposed downstream of the disk. This approach is widely used in the analytical BEM method without a rigorous justification, instead it is plausibly assumed that if the fluid is accelerated from zero rotational velocity upstream of the disk to $2\overline{a'}\Omega r$ downstream, then the value at the plane of rotation must be approximately $\overline{a'}\Omega r$. The axial and rotational induction at the blade are then calculated as $a = \overline{a}/F$ and $a' = \overline{a'}/F$ in agreement with Eq 3.21, before U_{rel} and ϕ are evaluated using Eqs 3.1 and 3.4, respectively.

3.3 Validation of the model

The model attempts to represent the effect of the aerodynamic forces on the flow field, so validation can be achieved by comparing key areas of the simulated flow field or by comparing calculated rotor loading with experimental results. Both of these type of measurements require costly experiments especially at geometrical dimensions that result in relevant blade Reynolds numbers at typical tip-speed ratios. A number of published experiments present only total force measurements, such as rotor torque and axial thrust with respect to tip-speed ratio, e.g. Bahaj, et al. [3]. These integrated quantities can be misleading, different physical phenomena occurring at the hub, the main power producing regions and at the tip mean that relatively large errors can sometimes be masked or cancel out. This means that apparently good agreement based on integrated power and thrust coefficients, could mask poor predictions of radial force distribution, and consequently the overall flow field. In order to reduce

costs, most experiments also employ relatively small rotors, for which the aerodynamic performance may be strongly dependent on Reynolds number and tip-speed ratio.

3.3.1 Description of test rotor and test case

The Unsteady Aerodynamics Experiment (UAE) Phase VI conducted by NREL provides exceptional data from wind tunnel testing of a 10m diameter wind turbine. Full details of the experiment can be found in Hand et al. [32]. A range of test sequences were designed for the purpose of providing data to validate semi-empirical models used in the design and evaluation of wind turbines. These included conditions with yaw and dynamic inflow, which result in highly complex flow effects including dynamic stall, upwind and downwind operation, as well as shrouded operation. It is evident that the focus of wind turbine development has shifted since the experiment, as only a small subset of the data seems to have been used in published validation studies. The wind turbine industry has also converged on upwind, pitch regulated designs, which has consequences for the modelling used and the experimental data required to validate such models.

The turbine design is documented in an earlier report by Giguere & Selig [29]. The design was intended to operate as a stall-regulated, downwind machine having a rated power of 20 kW and operating speed of 72 rpm. The blade optimization in terms of taper and twist was required to maximise annual energy output given a Rayleigh wind-speed distribution with an average wind speed of 7.2 m/s, but the geometry was heavily constrained to accommodate the instrumentation. Further compromises made for convenience and consistency with earlier rotor designs resulted in the geometry shown in Figure 3.2. The design shows a linear taper from root to tip, non-linear twist distribution, and a single 21% thickness S809 aerofoil section is used for the entire blade apart from near the hub where it transitions into a cylindrical section. The alternative chord length at $r/R = 0.176$ and the dotted line are consistent with the tabulated data in [32], but this seems an improbable geometry (possible typo) so the taper indicated by the heavy line is used in the current study. Recalling the discussion in Section 3.1.1, which explains the theoretical development of Prandtl's tip loss correction, it is interesting to note that the analysis considered a rotor with optimal circulation distribution. The imposed constraints suggest that the rotor described here is unlikely even to approach the optimal rotor of this analysis.

Sequence S is one of the most commonly referenced datasets, in which the turbine was run with the rotor in the conventional upwind position at steady rpm, but at wind speeds $U_\infty = 5..25$ m/s (in 1 m/s intervals), resulting in tip-speed ratios, $\lambda = 1.5..7.5$.

Table 3.1: Selected test runs from the wind tunnel experiment. Rotation speed of 72 rpm ($\omega = 7.54$ rad/s) and tip radius, $R = 5.029$ constant for all test runs. Rotor in upwind position at zero yaw, zero coning, and with a rigid hub connection. Only the four test runs indicated by the red rectangle are used in the subsequent comparison of the CFD AD model. (The reader should note that the ordering of the test sequences does indeed correspond to the blade tip pitches shown, i.e. not $2, 3, 4$).

Test Sequence	Blade Tip Pitch	Wind Speed
S	3	$5, 6, 7, 8, 9, 10$
T	2	$5, 6, 7, 8, 9, 10$
U	4	$5, 6, 7, 8, 9, 10$

For reference, the optimal λ for maximum C_P is close to $\lambda = 5.29$, according to computations by the rotor blade designer[29]. Sequences T and U are run at the same conditions, but with blades at a different fixed pitch. The three blade tip pitches are indicated on the plot of blade twist, β, in Figure 3.2. The current validation study compared results for sequences S,T and U up to nominal inlet wind speeds of 10 m/s, but because similar trends are seen throughout, the results presented are limited to sequence S, for wind speeds of 5, 6, 7 and 8 m/s. The most valuable data recorded was from rows of twenty-two pressure taps at five radial locations (r/R = 30%, 47%, 63%, 80% and 95%) on the instrumented blade. The taps were positioned to allow an accurate interpolation of the pressure distribution around the section, and were more concentrated about the leading edge to allow accurate location of the stagnation point, which was used to estimate the local angle of attack. Using the measured stagnation point dynamic pressure, corrected for centrifugal force, the pressure tap measurements could be expressed as the familiar C_p distribution. Data was recorded at 520.83 Hz over 30-second durations, only the mean and standard deviations (SD) of the resolved axial and tangential force coefficients (thrust and torque), C_{TH} and C_{TQ}, are used in this validation study. As the blade stagnation pressure is naturally unavailable in the AD simulation, C_{TH} and C_{TQ} were re-normalized using the dynamic pressure $q = \frac{1}{2}\rho[U_\infty^2 + (\Omega r)^2]$, which is known a priori.

Previous simulation studies have all identified that the majority of higher inlet wind speeds tested resulted in significant stall regions across the blade, e.g. [71]. The recorded mean and standard deviation of the thrust and torque coefficients are plotted in Figure 3.3 for the S, T and U sequences, at inlet wind speeds from 5..10

m/s. Blade pitch (and twist) is defined as positive when the blade is rotated towards feather. Reducing the pitch from 4..2°, cf. Figure 3.2, will result in a higher effective angle of attack (cf. Figure 3.1) and higher aerodynamic force coefficients in the pre-stall region. This is seen clearly for wind speeds of 5..8 m/s in Figure 3.3. While the standard deviations, indicated by the error bars, are small for wind speeds of 5..8 m/s, the data series at $U_\infty = 9$ m/s is beginning to show a wider SD, which increases as the pitch is reduced (increase in angle of attack), although the mean values continue to follow a similar trend to the lower wind speeds. At $U_\infty = 10$ m/s, large standard deviations and a sharp fall in the mean force coefficients at the second and third radial stations indicate unsteady flow and significant stalled flow on the suction surface of the blade. The current validation study will focus on inlet wind speeds $U_\infty = 5..8$ m/s, which correspond to tip speed ratios, $\lambda = 4.7, 5.4, 6.3, 7.4$, where significant stall is not expected. This allows greater focus on the accuracy of the model itself by not introducing the uncertainty of constructing accurate mean aerodynamic force coefficient input data.

3.3.2 Airfoil data

The considerations for constructing a suitable set of aerodynamic data in the form of lookup tables for the AD model were introduced in section 3.1.2, and the methods chosen for the current study are documented here. The experimental rotor of Figure 3.2 uses a single aerofoil section along the blade, but the model should be able to account for varying aerofoil sections along the span of the blade. Even a single section will have different aerodynamic properties depending on its radial location, due to the radial effects mentioned in section 3.1.2, but also as a result of the variation of chord Reynolds number, Re_c. Figure 3.4 shows an estimate of Re_c for the required range of U_∞, where the local relative velocity magnitude U_{rel} is estimated as $\sqrt{U_\infty^2 + (\Omega r)^2}$. The rotational velocity dominates and there is a relatively small variation of $Re_c \approx 6..9 \cdot 10^5$ from the root to the tip. Figure 3.5 shows the data from wind tunnel measurements of the S809 section at $Re_c = 3..10 \cdot 10^5$. Three different wind tunnel facilities (indicated by OSU, CSU and DUT in the legend) measured the aerodynamic properties of the S809 section independently at a range of Re_c. Also shown for comparison are polars calculated for $Re_c = 10.0 \cdot 10^5$ using Xfoil [18] with the default free transition model.[2] The experimental polars show a surprising level

[2] Xfoil is an open source implementation of a viscous-inviscid design/analysis code for transonic and low Reynolds number aerofoils. The two-dimensional Euler equations are strongly coupled to an integral boundary-layer formulation with transition prediction.

of variation, and also clear disagreement in the case of $Re_c = 1 \cdot 10^6$, which was measured independently at two facilities. In particular, the range of slopes in the linear region of the $C_L(\alpha)$ curve, as well as a range of values for α_0 (where $C_L(\alpha_0) = 0$ suggest systematic measurement errors at the facilities. Different levels of free stream turbulence and surface roughness could also cause variation, the facilities are all described as "low turbulence" wind tunnels, but no quantitative information is given regarding turbulence intensity or model surface roughness. The measurements at $Re_c = 6.5 \cdot 10^5$ and $7.5 \cdot 10^5$ also show unrealistically low values for drag, resulting in very high lift-to-drag ratios.

In order to proceed, all six experimental polars were processed as outlined in section 3.1.2, and the results are demonstrated in Figure 3.6 for $Re_c = 3 \cdot 10^5$. The polars were first smoothed using the radial basis function method available in SciPY [37], where the default multiquadratic kernel and a smoothing parameter of 0.1 were used, which relaxed the resulting polar from interpolating outlying points. This was a precautionary measure to ensure steady convergence of the blade element method in the AD model. While the experimental test cases have been chosen to avoid stalled flow, the maximum angle of attack was not known a priori, so the experimental polars were extended to 50° with the widely-used model of Viterna & Janetzke [76]. The drag coefficients were corrected with the model of Eggers et al. [20], which unlike the drag correction of Du & Selig [19], predicts an increase of drag at the inboard sections. The extrapolation to higher angles of attack and the correction of lift and drag coefficients using the referenced models was made particularly easy by a set of tools written in Python called AirfoilPrep [49], made available by NREL. The correction was applied at five radial stations spaced equally between $r/R = 0.25$, where the transition from the cylindrical section is complete, and the blade tip.

Figure 3.6 shows the increasing effect of the correction towards the hub, increasing C_L and C_D at and after stall, while a slight decrease is predicted at the blade tips. These trends are consistent with the CFD study of [71]. The line labeled 'no3D' shows the polar which has been smoothed and extrapolated to higher angles of attack (if not present in the experimental results), which is used to compare the effect of the correction model. From Figure 3.5 it is clear that two of the CSU experimental runs did not include many negative angles, the Re=$3 \cdot 10^5$ data set does not even include the zero lift angle, α_0. This is not critical for the current study as the results will show that no negative angles of attack are encountered for the studied operating conditions, the incorrect extrapolation below $\alpha = 0°$ in Figure 3.6 similarly is unimportant for the

current study (as long as $C_L(\alpha)$ is well behaved for convergence of the blade element solution).

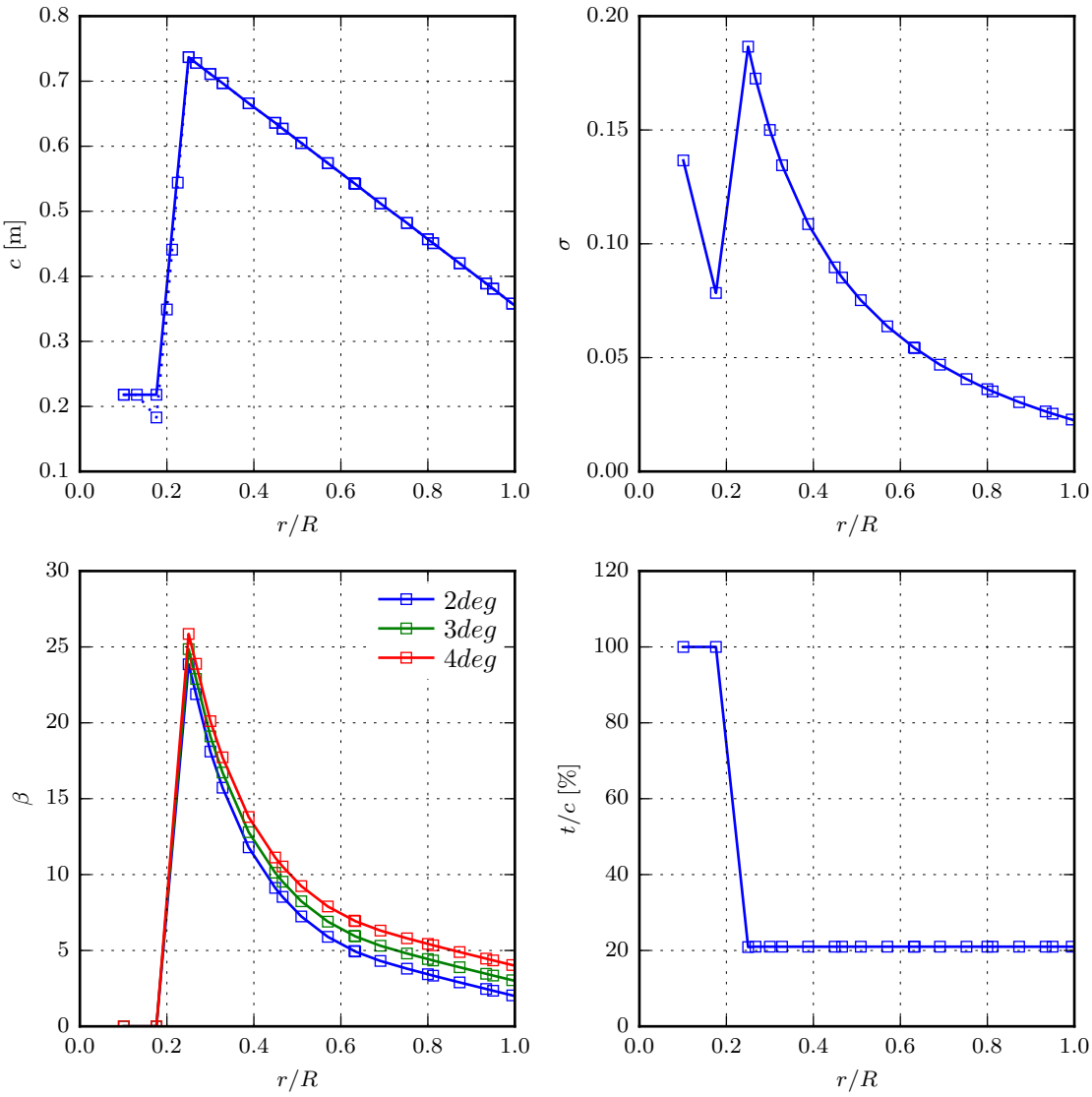


Figure 3.2: Geometrical description of NREL Phase VI rotor

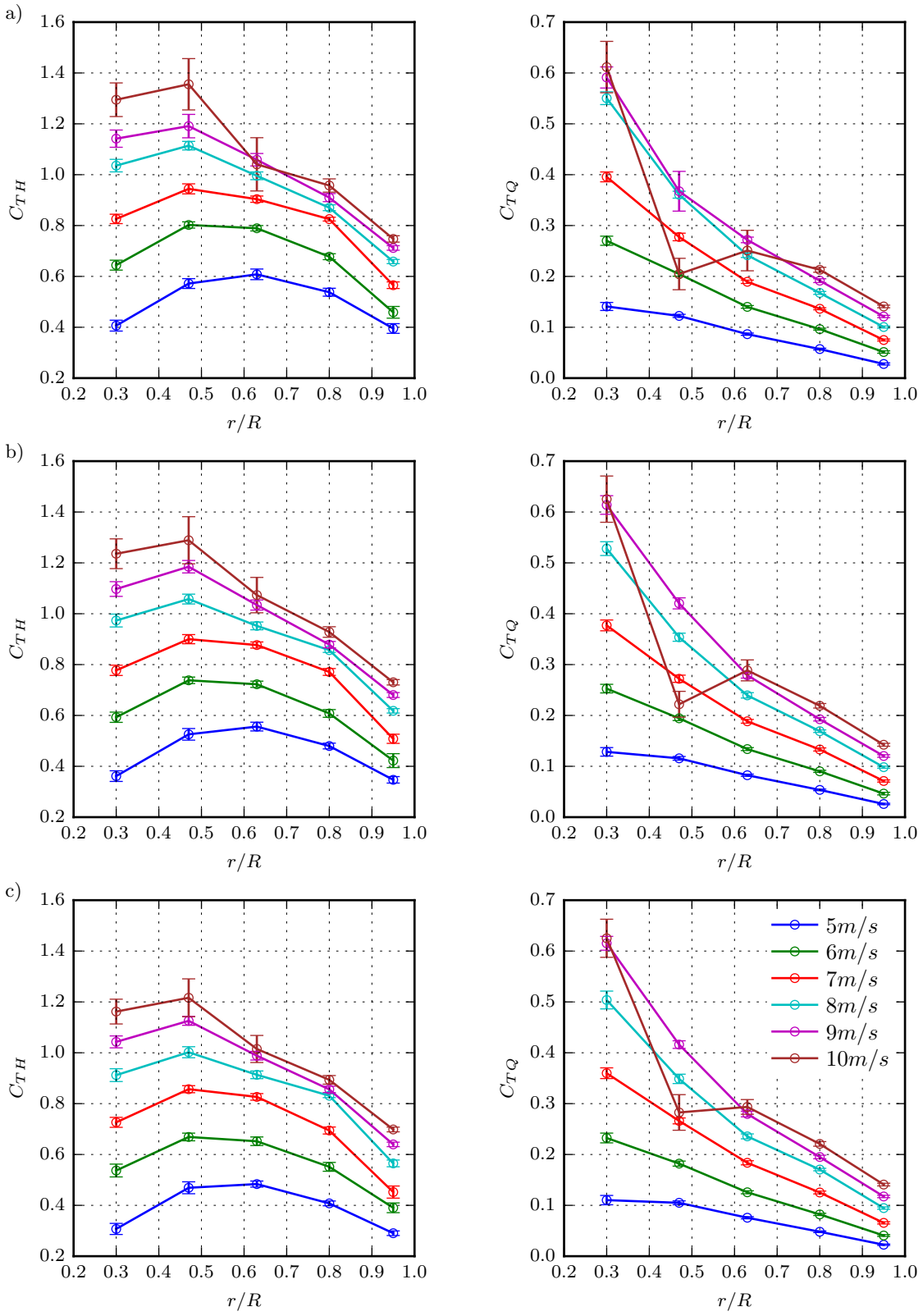


Figure 3.3: NREL Phase VI results for Sequence T, S (sic, cf. Table 3.1) and U ($\beta_{\text{tip}} = 2°, 3°, 4°$), (a), (b) and (c) respectively. Error bars indicate ±1SD centred on the mean value.

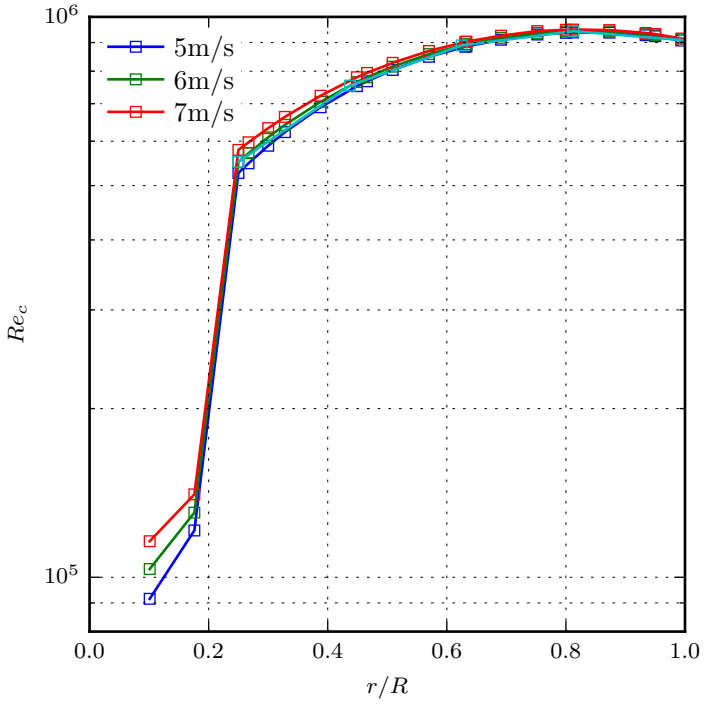


Figure 3.4: Blade Reynolds number across experiment flow speeds; $5 - 7$ m/s.

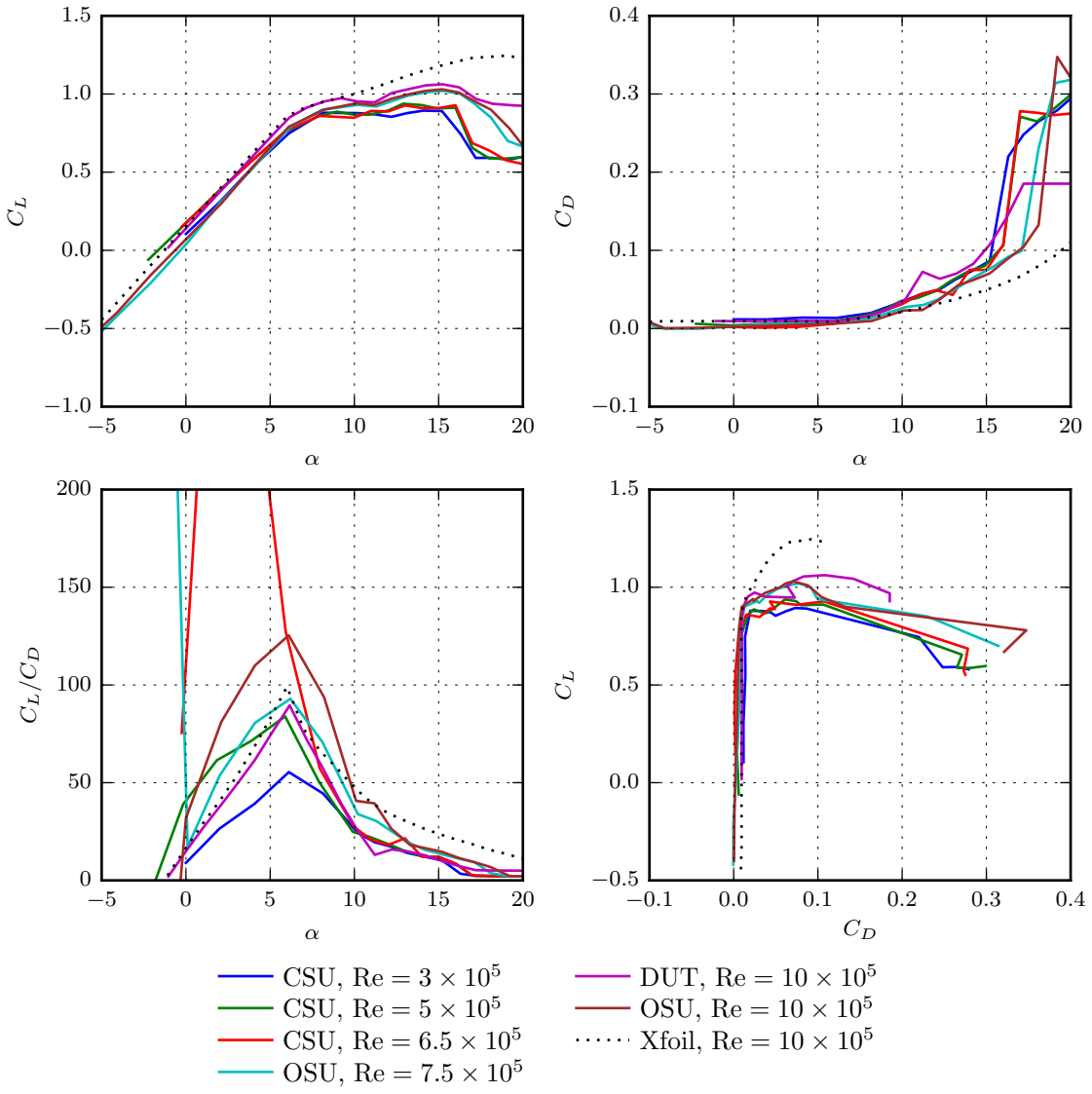


Figure 3.5: Experimentally measured polars. CSU, OSU and DUT signify three different wind tunnel facilities (further details in [32])

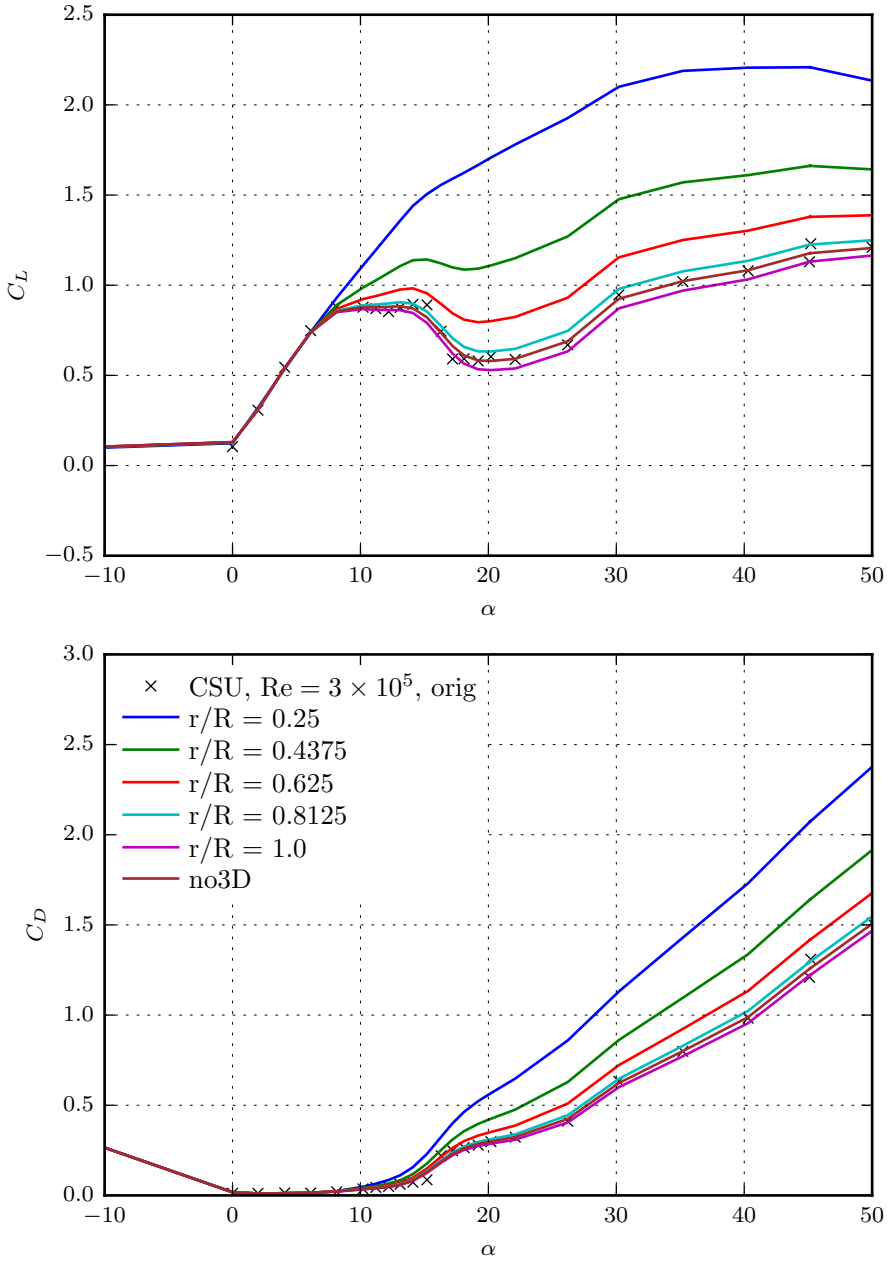


Figure 3.6: Preparation of aerofoil polars for BEM

3.4 Simulation setup

The computational domain was meshed to match the vertical and lateral extents of the experimental test section, width $z/D = 3.66$, height $y/D = 2.44$, which results in a blockage ratio of 0.089. From the schematic diagram of the experimental setup (Figure 1 in [32]), the test section length appears to be similar to the width, but the distance from the upstream to the downstream guide vanes appears to be ca. $15D$. The computational domain extends from $-5 \leq x/D \leq 10$ which is assumed to extend far enough to allow zero streamwise gradient boundary conditions at the inlet and outlet, and the rotor hub is centred at $\{x, y, z\} = \{0, 0, 0\}$ as in the experiment.

Uniform velocity was assigned at the inlet corresponding to the experiments. Inlet turbulence values are set to values of k and ϵ corresponding to a turbulence intensity $TI = 0.5\%$ and length scale $L = D/20$, which result in TI remaining almost unchanged before it begins to increase at $x/D \approx -0.5$ to an average of 1.5% at the AD plane. Turbulence intensity is defined as $TI \equiv \frac{u'}{U}$ where u' and U are the root-mean-square of the turbulent velocity fluctuations, which is related to the turbulent kinetic energy k as $u' = \sqrt{\frac{2}{3}k}$, and the normalizing velocity (taken as the bulk mean streamwise velocity in all cases in the present study) respectively.

When discussing the experimental aerofoil data in Section 3.3.2, the turbulence conditions of the measurements were presumed to be low, e.g. $TI = 0.5\%$, but it should be observed that the reference velocity for the rotating blades increases by a factor close to the tip-speed ratio λ above the tunnel mean velocity. Ideally the turbulence intensity in the quasi-2D aerofoil experiment and rotor experiment would be related as $TI_{\text{aerofoil}} \approx TI_{\text{rotor}}/\lambda_r$, which is achieved reasonably closely in the present simulations for the main power producing radii ($r/R \approx 0.7..0.9$).

The side walls are modelled as slip walls to avoid the spatial resolution required to resolve the boundary layer, in order to keep the computational cost low. The additional effective blockage due to the naturally no-slip walls of the experiment can be estimated using the boundary layer displacement thickness, but it is negligible for the current study.

A boom mounted camera and bulky instrumentation enclosures (fractionally wider than the blade hub connection) were mounted at $\approx D/10$ and $\approx D/3$ respectively upstream of the rotor, which meant that the hub geometry was far from aerodynamically streamlined. The precise geometry details are not published but appear to be too complicated to be meshed in detail, although the most inboard sections of the rotor will certainly be affected by a disturbed flow profile. For the current study, the

most simple approximation of an impermeable disk at the rotor plane with a diameter extending to the blade hub connection, $r_{\text{hub}}/R = 0.101$, is used. This is solely intended to model the blockage caused by the hub, it is not sufficiently discretized in any of the meshes to be able to resolve the detailed physics of flow normal to a circular disk, nor would such a flow be correct.

The meshes were generated using ANSYS® ICEM CFD®[2]. Structured hexahedral and fully unstructured tetrahedral meshes were used, each with three levels of refinement, in order to investigate grid dependence and convergence. Figure 3.7 shows a two-dimensional slice of the mesh at the disk plane for the structured and unstructured mesh, these are the coarsest meshes in each case, as the medium and fine resolution meshes would become obscure at this scale. The structured mesh uses a regularly spaced polar grid at the disk, with an O-grid topology at the hub, and double O-grid topology in the bypass region. This 2D plane is extruded to the inlet and outlet with a gradual transition to larger streamwise spacing. The medium case uses 32 radial nodes across the disk and 128 around the circumference, while the bypass and streamwise cell sizes are matched at the disk but grow slowly towards the boundaries. For the coarse and fine cases the node counts are scaled in the radial direction by approximately 0.6 and 1.5 respectively, while the streamwise direction was left unchanged, following previous experience. For the tetrahedral mesh, the nominal cell size at the disk was scaled in the same way, and a cylindrical density region of diameter 2D stretching from the disk to the outlet limited the maximum cell size in that area to better resolve the free shear and swirling flow. The maximum cell size was varied to produce a similar total cell count to the structured meshes. The coarse, medium and fine meshes had ca. $1.4 \cdot 10^6$, $2.1 \cdot 10^6$ and $4.7 \cdot 10^6$ cells, respectively.

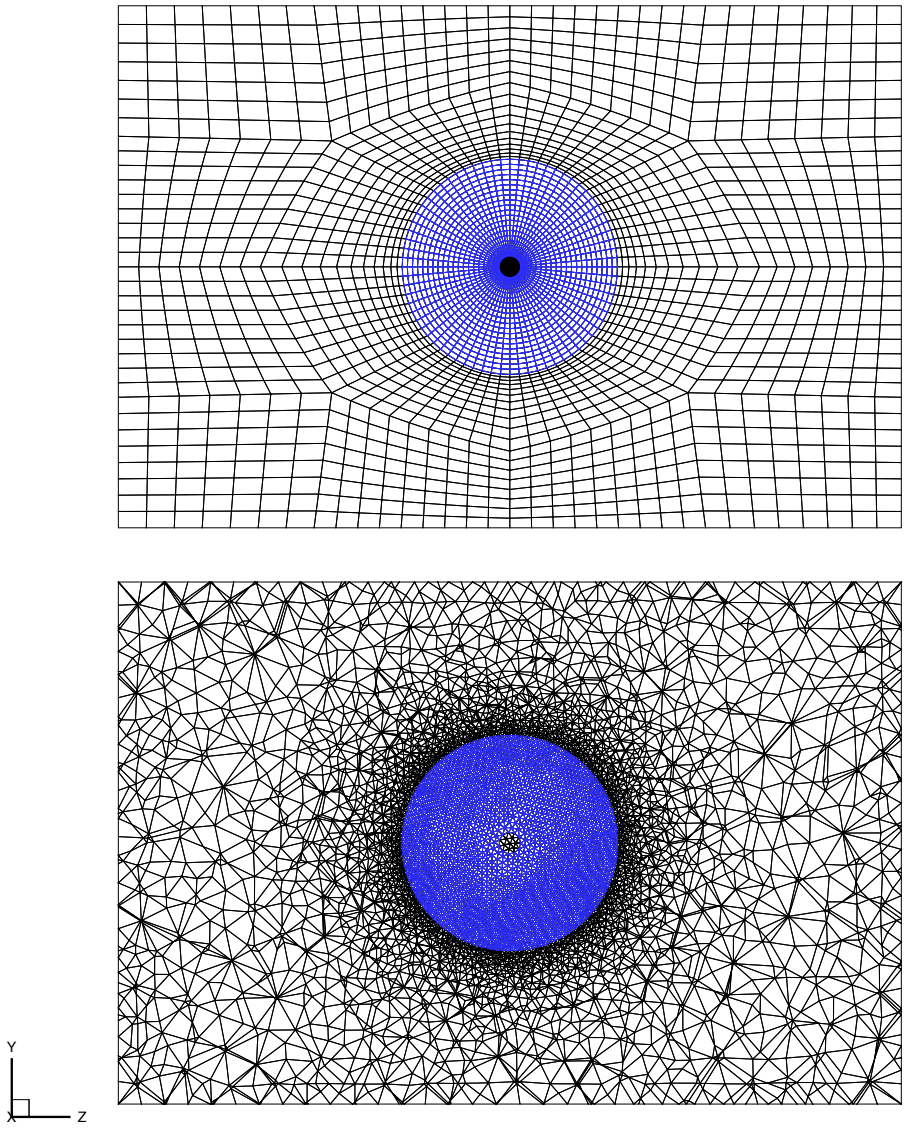


Figure 3.7: Mesh at disk plane. Top: Structured, hexahedral; Bottom: Unstructured, tetrahedral.

3.5 Results

3.5.1 Convergence and grid refinement

The presentation of the CFD results begins with the grid resolution study. For a particular operating point, set of aerofoil data and choice of modelling options, velocity profiles of the converged solution for each of the six meshes are presented.

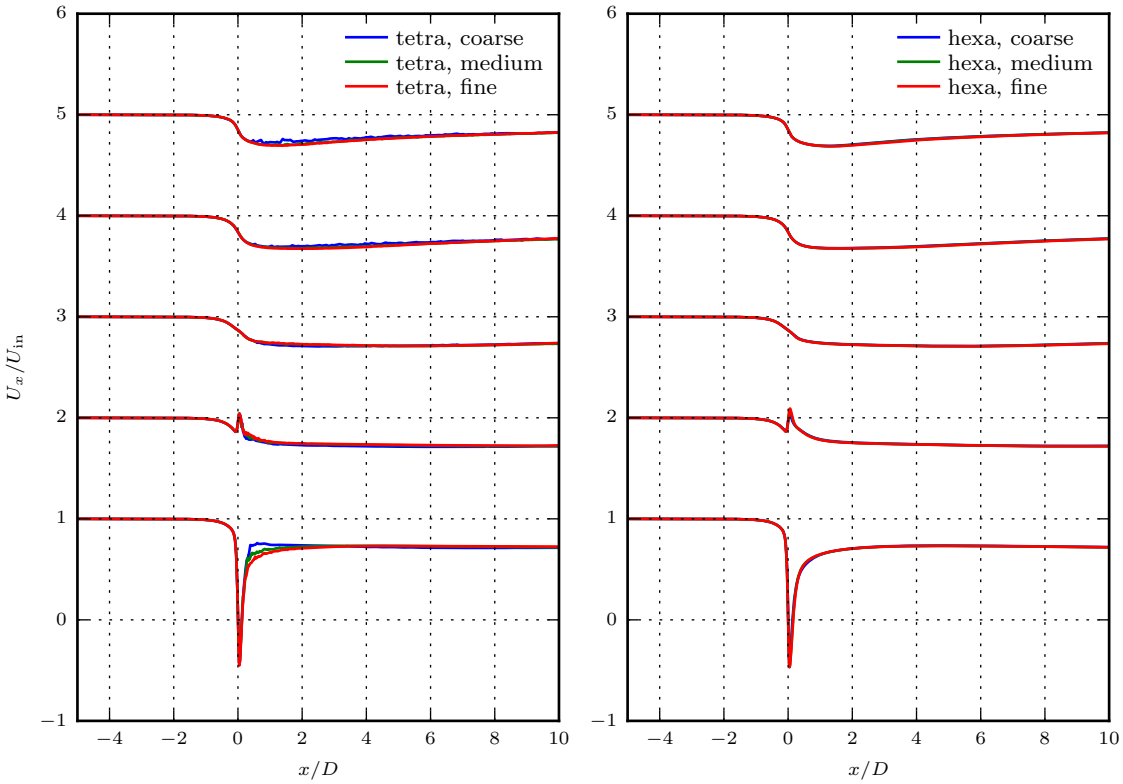


Figure 3.8: U_x on axial line passing through the AD, from bottom to top at $r/R =$ 0.0, 0.2, 0.4, 0.6 and 0.8, on the horizontal centre-plane. (Radial stations offset by 1m/s). Left: Unstructured, tetrahedral; Right: Structured, hexahedral.

Figure 3.8 shows the normalised axial velocity on axial lines running through the AD at $r/R = 0.0, 0.2, 0.4, 0.6, 0.8$. The centre line at $r/R = 0$ shows negative axial velocity caused by recirculation downstream of the hub disk, which is not present at other radial stations. Figure 3.9 shows contours of axial velocity U_x on a horizontal plane through the centre of the AD. The disk is indicated as a heavy black line and the gap at the centre is where the hub is modelled as an impermeable wall. The area of recirculation behind the disk is shown clearly in the zoomed view of the hub-disk intersection region, where the velocity direction vectors are also plotted. The area of

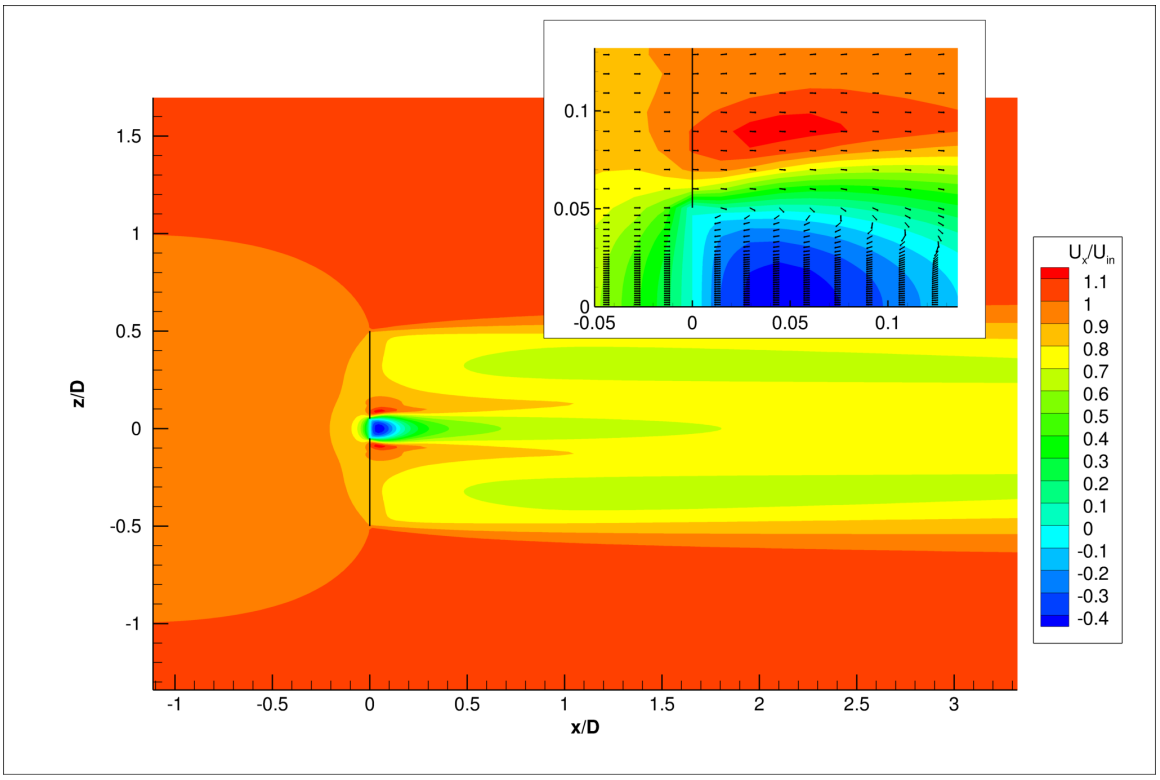


Figure 3.9: Contours of axial velocity on horizontal plane passing through the AD. Subplot: Zoomed view of the hub-disk intersection region with velocity direction vectors included (length does not indicate magnitude).

accelerated flow past the edge of the hub extends to $r/R = 0.2$ ($z/D = 0.1$), which causes the region of $U_x/U_\infty > 1$ in Figure 3.8. The contour plot shows the widening shear layer downstream of the edge of the AD, which also corresponds to the increased wake recovery on axial lines further from the centreline.

In terms of convergence, it is observed that the structured hexahedral grids agree well regardless of the level of mesh refinement, such that the lines obscure each other. Analysis of the data shows steady convergence from the coarsest to the finest mesh (one-sided convergence to the solution on the finest mesh, with decreasing change at each mesh refinement). E.g. choosing a reference point at $x/D = 1$ on the axial line ar $r/R = 0.6$, if U_x for the fine hexahedral mesh is assumed to be the most accurate solution, the coarse hexahedral mesh results in 8.0% higher axial velocity and the medium mesh 0.04% higher velocity at this point. The medium hexahedral mesh represents very good spatial convergence at a reasonable computational cost. Convergence is slower for the set of tetrahedral meshes, but it is steady and approaching the converged solution of the hexahedral mesh (0.2% higher than the reference point using the fine tetrahedral mesh). The coarsest tetrahedral mesh clearly has insuffi-

cient resolution in the wake downstream of the AD as indicated by the non-physical (considering the current turbulence modelling approach) wiggles. Even the finest tetrahedral mesh shows wiggles around $x/D = 1$, which confirms that discretization techniques of the CFD software are better suited to hexahedral elements.

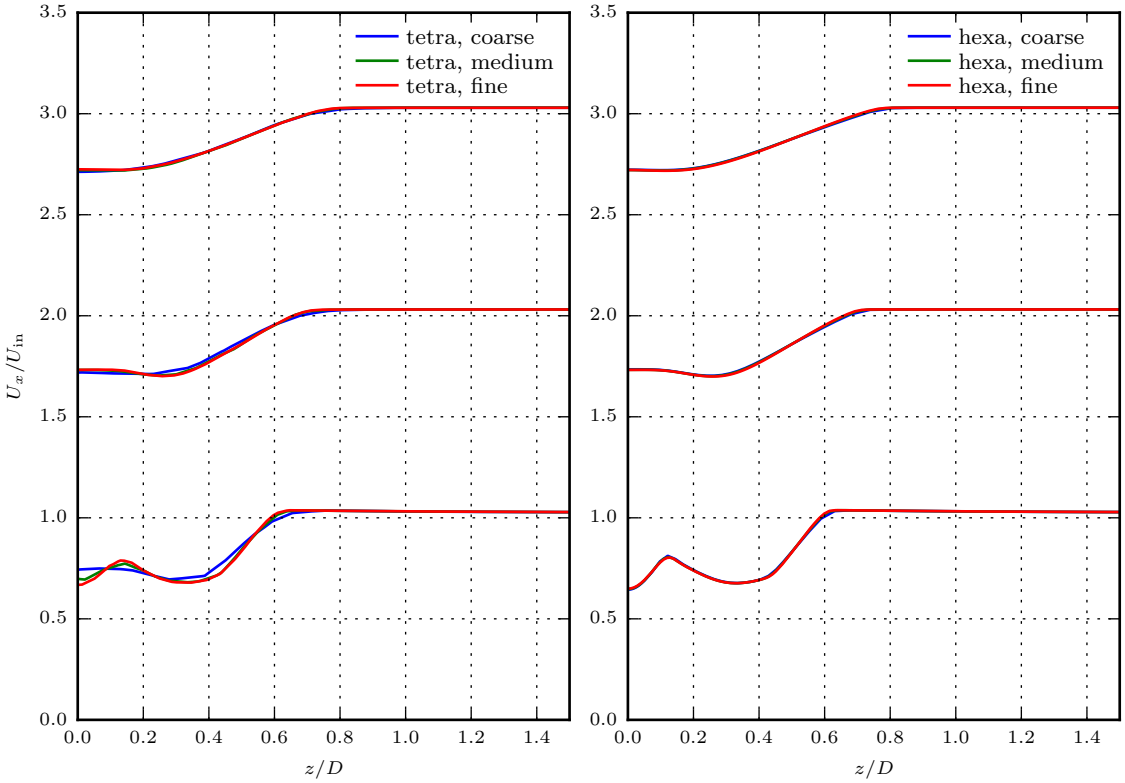


Figure 3.10: U_x on transverse line downstream of the disk, from bottom to top at $x/D = 1$, 5 and 9, on the horizontal centre-plane. (Streamwise stations offset by 1m/s.)

Figures 3.10 and 3.11 show the axial and rotational velocity components, respectively, on transverse lines on the horizontal plane at $x/D = 1$, 5 and 9 (downstream of the AD). On transverse lines, the rotational velocity is equivalent to the y-velocity in the current domain. The turbine is rotating in the positive sense about the x-axis at Ω causing the wake to rotate in the opposite direction to conserve the angular momentum in the flow. In the model this is implemented as Eq. 3.34. For reference, the hub diameter corresponds to $z/D = 0.05$ and the rotor blade transitions from a cylindrical (non-lifting) section at $r/R = 0.176$ to the first blade section at $r/R = 0.25$. This region of predominantly negative torque (due to the cylinder drag force) just downstream of where the hub wake ends results in reversed rotational flow

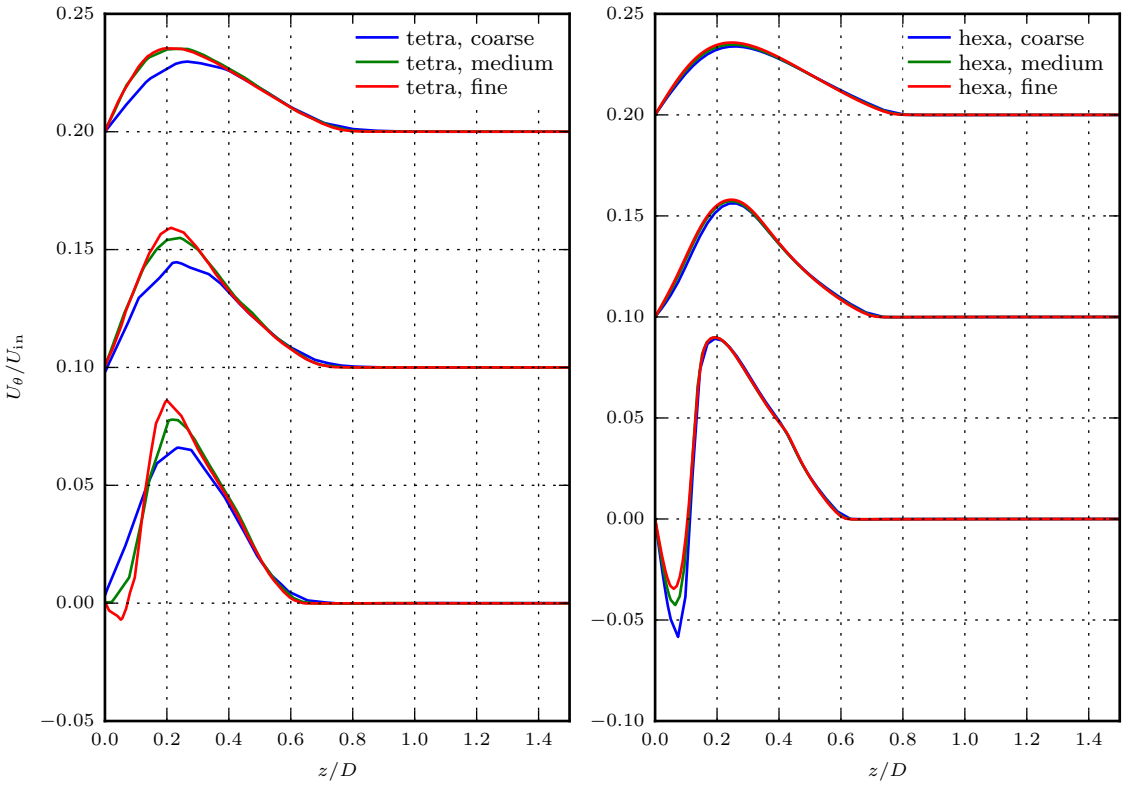


Figure 3.11: U_θ on transverse line downstream of the disk, from bottom to top at x/D = 1, 5 and 9, on the horizontal centre-plane. (Streamwise stations offset by 0.1m/s.)

velocity, i.e. flow being pushed around in the same direction as the blade. The associated impact on rotor performance will become apparent in plots to follow. The grid dependence and convergence observations are the same as for the plots on axial lines: Both tetrahedral and hexahedral meshes demonstrate steady convergence with refinement and the finest tetrahedral solution is approaching the hexahedral solution. The spatial resolution of the coarsest tetrahedral mesh is seen again to be wholly insufficient.

3.5.2 Comparison of rotor performance

Ignoring the Reynolds number dependency along the blade span (cf. Figure 3.4), each experimental set of drag and lift polars in Figure 3.5, following correction for rotational effects (cf. Figure 3.6), was used as input data for each of the experimental tip-speed ratios. At constant rotor rpm, the wind speeds $U_\infty = 5, 6, 7, 8$ m/s correspond to $\lambda = 4.7, 5.4, 6.3, 7.4$, as discussed in Section 3.3.1. The rotor power is

calculated as $P = \int \Omega \, \mathrm{d}Q$, which on the discrete faces of the AD becomes:

$$P = \rho\Omega \sum rU_{\theta,\mathrm{wake}}U_D\delta A$$

The results for rotor power and thrust are plotted as C_P and C_T in Figure 3.12, as well as the percent deviation from the experimental values. According to the experimental results the peak power point, $C_{P\max}$, is most closely approached at $\lambda = 6.3$. Two aerofoil datasets result in prediction of maximum C_P at higher λ, while the others show a peak at $\lambda = 6.3$, but with a spread of C_P values -7%..+10% about the experimental value. Thrust is generally over-predicted, at $\lambda = 6.3$ the deviation is 3-12%. There is a consistent trend of increasing C_P with Reynolds number, but as was discussed in relation to Figure 3.5, the experimental polars displayed inconsistent variation with respect to Reynolds number. The goal of the current study is not to select the "correct" aerofoil dataset based on agreement of the model with the experiment. It is not certain that any dataset is correct, and such an approach would naturally compromise the validation study. The uncertainty of aerofoil data as a model input for BEM methods has been reported before, e.g. [46], Figure 3.12 confirms this quantitatively.

For the CSU dataset at $Re = 3 \cdot 10^5$, the dotted and dashed lines show the effect of different modelling approaches applied to the blade tips. From Section 3.1 Prandtl's tip-loss correction for a finite number of blades can be neglected in the code by setting $F = 1$ in Eq. 3.21. Similarly, the correction of Shen et al. (cf. Section 3.1.2.3) for the blade forces can be ignored by setting $F_1 = 1$ in Eq. 3.30. When both F and F_1 are calculated, this is referred to the Shen modelling option in the current study, as it includes the most physics it is considered to be the most accurate option and will be the default case unless noted otherwise. If only F is calculated, but F_1 is fixed at 1, this is referred to as the Glauert modelling option, acknowledging Glauert's introduction of Prandtl's tip-loss factor in the BEM method. The third approach is where neither correction is applied, this is a very inaccurate approach and serves as a comparison only.

In Figure 3.12, the Glauert model causes a dramatic drop in C_P and C_T compared to the case with no tip corrections through its effect on the induction factors, while the Shen model lowers the loading directly via the aerodynamic force coefficients. For this particular aerofoil dataset, the corrections appear to be very effective matching the modelled and experimental C_T, but too severe if comparing modelled and experimental C_P. A general conclusion cannot be formulated following the discussion above regarding the consistency of the experimental aerofoil data, but it is reassuring that

the tip models tend towards accurately matching the thrust, which means that the global momentum balance is accurate. It is also clear that the corrections, while only affecting radial stations close to the blade tips, have considerable impact and cannot be ignored.

To complete the assessment of grid dependence and convergence, Figure 3.13 shows how C_P and C_T for the CSU dataset at $Re = 3 \cdot 10^5$ vary with respect to the mesh type and size. The spread of C_P is largest at $\lambda = 6.3$ and is less than 1%. The better resolved meshes appear to predict higher C_P than the less resolved meshes, which under-predict the velocity shear between the bypass and core flow through the AD in the near wake of the disk.

Figure 3.14 contains a grid of sub-plots showing azimuthally averaged output variables from the AD model, which enables detailed comparison of different cases. In order the variables plotted are:

- a: $= \overline{a}/F$, Axial induction at the blade
- $\overline{a}$: Azimuthally averaged axial induction
- a': $= \overline{a'}/F$, Tangential induction at the blade
- $\overline{a'}$: Azimuthally averaged rotational induction
- U_{rel}: Normalised relative velocity magnitude at the blade element
- F, F_1: Glauert tip-loss and Shen correction factors
- ϕ: Relative inflow at blade element, with respect to disk plane
- α: $(= \phi - \beta)$ Effective angle of attack at blade element
- C_P: $= \frac{P}{\frac{1}{2}\rho U_\infty^3 A}$ Power coefficient
- C_{TH}: $= \delta T / \frac{1}{2}\rho[U_\infty^2 + (\Omega r)^2] 2\pi r \delta r$ Thrust coefficient
- C_{TQ}: $= \delta F_Q / \frac{1}{2}\rho[U_\infty^2 + (\Omega r)^2] 2\pi r \delta r$ Tangential force coefficient[3]

Compared to C_T for the integrated thrust, used in Figures 3.12 and 3.13, a radially varying reference velocity of $\sqrt{U_\infty^2 + (\Omega r)^2}$ is used in the alternatively defined C_{TH}

[3] This is a tangential force coefficient rather than an actual torque coefficient as the lever arm is not included. However, the terminology has been retained from the original publication of the experiments [32].

and C_{TQ}. This is mainly done to be consistent with the literature on the NREL Phase VI experiment, including other model validation studies.

There is generally very close agreement between all the meshes, on the scale plotted any differences appear to be just outboard of the hub e.g. $r/R \approx 0.2$. However, the annulus area increases as r/R meaning that these inboard sections contribute little to the integrated C_T and C_P plotted in Figure 3.12. The slightly increased C_P of the finest resolved hexahedral mesh for example is related to a slightly increased C_P at outboard radial stations, (e.g. 0.46% at $r/R = 0.9$). The deviation of C_{TH} and C_{TQ} from experimental values shown as a percentage in the final plot is typical of the agreement found for all aerofoil datasets (results using a different dataset are shown in Figure 3.18). Having concluded the assessment of grid dependence, all subsequent plots show data from the medium resolution hexahedral mesh, deemed to offer sufficient accuracy at reasonable computational expense.

3.5.2.1 Effect of modelling

The data in Figure 3.14 was modelled using the Shen correction, which is taken to be the default, state-of-the-art approach. Figure 3.15 compares the effect of using no tip corrections, only the Glauert correction and finally, the Shen correction. Beginning with the axial induction a and its relation to the annulus averaged induction factor $\overline{a}$: For the Glauert and Shen models, a is calculated as $a = \overline{a}/F$, where the Prandtl tip-loss function F tends to zero as $r/R \to 1$. As the solution converges iteratively, this results in $\overline{a}$ being reduced as $r/R \to 1$ when the Glauert correction is active, but not tending to zero, which is the conclusion of the limit analysis of Shen et al. [62] for the analytical BEM method. The same observations are true for the rotational induction factors, although the effect is smaller as both are already close to zero near $r/R = 1$. The effect on U_{rel} is small, but there is a marked reduction in inflow angle as $r/R \to 1$ and hence angle of attack, α, for the tip loss modelling cases at the blade element (cf. Figure 3.1). The lower angle of attack results in lower aerodynamic force coefficients, leading to lower power, thrust and torque coefficients near $r/R = 1$.

The Shen correction, which is always combined with the Glauert correction, directly drives the force coefficients to zero as $r/R \to 1$. This accentuates the effect of the Glauert correction on the power, thrust and torque, but with the F_1 function (at this λ and blade number Z, cf. Eq. 3.31) becoming more localized at the tip. Reducing the loading via the Shen correction naturally reduces $\overline{a}$ close to $r/R = 1$, which is read from the CFD solution.

Finally, for the Shen modelling case, the dashed line shows the results using the original aerofoil data without applying the 3D corrections of Section 3.1.2. The 3D lift and drag augmentation takes noticeable effect at the inboard sections below $r/R \approx 0.6$, where α is greater than ca. 10 deg, and the model of Du & Selig predicts significantly higher C_L values (cf. Figure 3.6). This results in increased thrust and torque (and power) at the inboard sections, with associated increases in axial and rotational induction.

The deviation of C_{TH} and C_{TQ} from experimental values in the final plot clearly shows the successive improvement of the Glauert and Shen models in matching the experimental forces at the most outboard section. At the inboard locations, the correction of the aerofoil data for 3D effects reduces that absolute deviation from the model to the experimental results, but overestimates the correction. This was typical for all of the aerofoil datasets used in the present study.

3.5.2.2 Effect of tip-speed ratio

Figure 3.16 re-plots the data using the Shen model from the previous figure, but includes results from all tip-speed ratios investigated. The relationships of increasing (normalized) U_{rel} and decreasing α with increasing λ can be easily understood with the help of the vector diagram in Figure 3.1. While the integrated thrust, using $q = \frac{1}{2}\rho U_\infty^2$ in Figure 3.12 increases with λ, the alternative thrust coefficient C_{TH}, which is non-dimensionalized using dynamic pressure $q = \frac{1}{2}\rho U_\infty^2[1 + \lambda_r^2]$ where $\lambda_r = \Omega r/U_\infty$, decreases with increasing λ (for the current range of λ). The simple trends of C_{TH} and C_{TQ} result when all rotor locations at all operating conditions are on the positive slope of the $C_L(\alpha)$ curve (cf. Figure 3.6).

As in the previous figure, all cases were repeated using uncorrected aerofoil data, and the results plotted using dashed lines. The current plot highlights that these corrections only become effective at lower tip-speed ratios where the angle of attack approaches the 2D stall angle. Interestingly in this case, for $\lambda = 4.7$ and 5.4, using the uncorrected data results in very similar values of C_{TH} and C_{TQ} close to the hub. This is due to the flat peak of C_L in the region of $8 < \alpha < 14$ deg (cf. Figure 3.6).

Figure 3.17 re-plots the bottom row of sub-plots from Figure 3.16 to allow closer inspection of the effect of the model performance across various λ with and without aerofoil 3D correction. Overall, the qualitative trends of the AD model agree well with the experimental results. Quantitative agreement is also good, with all but the most inboard radial station, across all studied tip-speed ratios, deviating from the experimental results to a lesser degree than the variability of aerodynamic data.

In the discussion of the grid dependence study, reference was made to a region of accelerated flow bypassing the hub modelled as an impermeable disk (cf. Figure 3.9). The behaviour of the flow in the experiment may have been quite different due to various non-streamlined instrumentation enclosures mounted upstream of the rotor. This may play a role in explaining why the most inboard radial station shows the poorest agreement with the experimental results, across all tip-speed ratios, and also using different aerofoil datasets.

The familiar array of AD output plots are shown also for the CSU aerofoil dataset at Re=$5 \cdot 10^5$ in Figure 3.18. The results follow the same trends discussed already in this section. It is notable that this dataset did not result in the highest C_P occurring at $\lambda = 6.3$ as was the case in the experiment and with the lower Reynolds number dataset. This difference is particularly noticeable when comparing the progression of the radial C_P with λ for the two datasets. Again the 3D aerofoil data correction is seen only to play a significant role for the lowest tip-speed ratio considered. For pitch and rpm controlled turbines operating at their design tip-speed ratio, the 3D aerofoil data correction may therefore not be important.

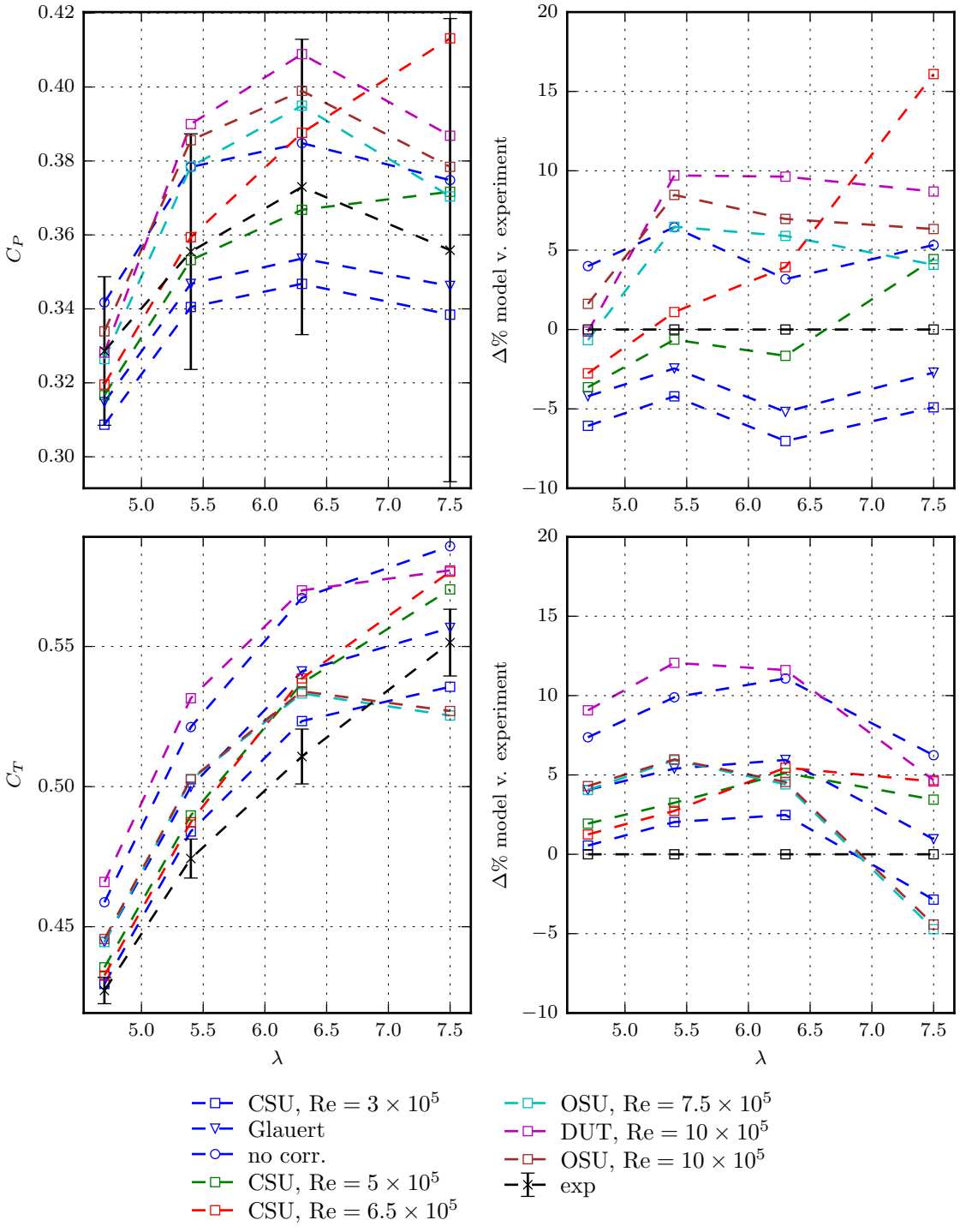


Figure 3.12: C_P and C_T using different aerodynamic data, where the integrated rotor power coefficient $C_P = \frac{P}{\frac{1}{2}\rho U_\infty^3 A}$ and $C_T = \frac{T}{\frac{1}{2}\rho U_\infty^2 A}$. The (default) Shen tip correction is used in all cases except for CSU, Re = 3×10^5 which is also presented for the Glauert correction and no tip correction.

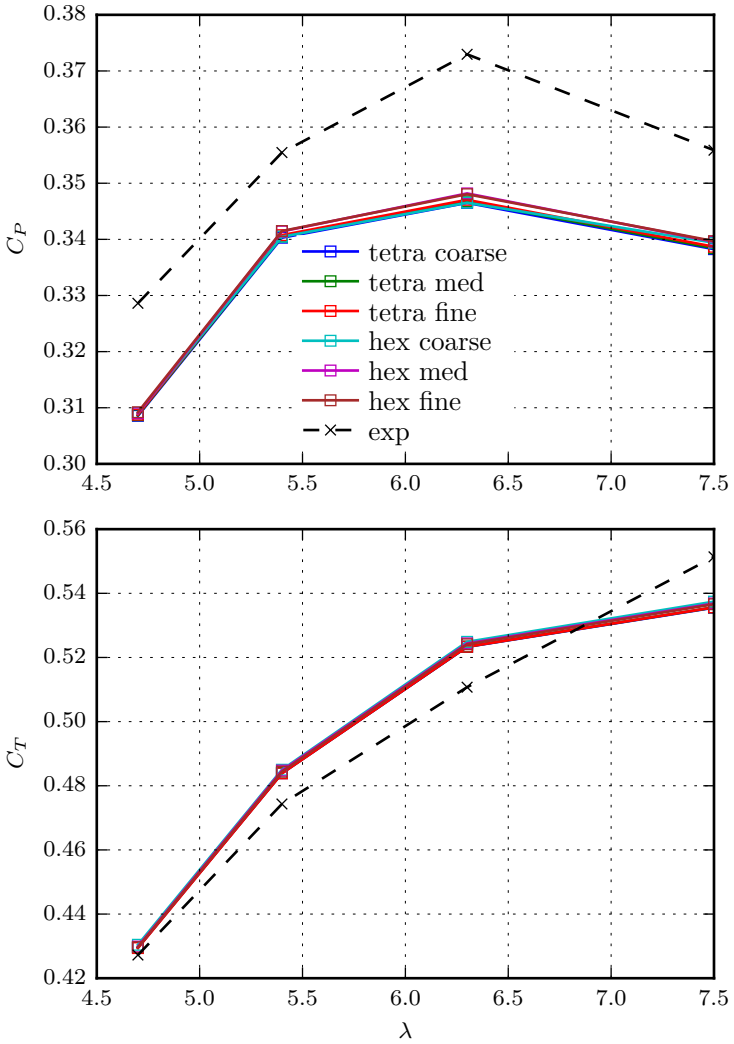


Figure 3.13: C_P and C_T using aerodynamic data CSU $Re_c = 3 \cdot 10^5$ on different grids, using the (default) Shen tip correction. This data generally led to the lowest power predictions as observed in Figure 3.12

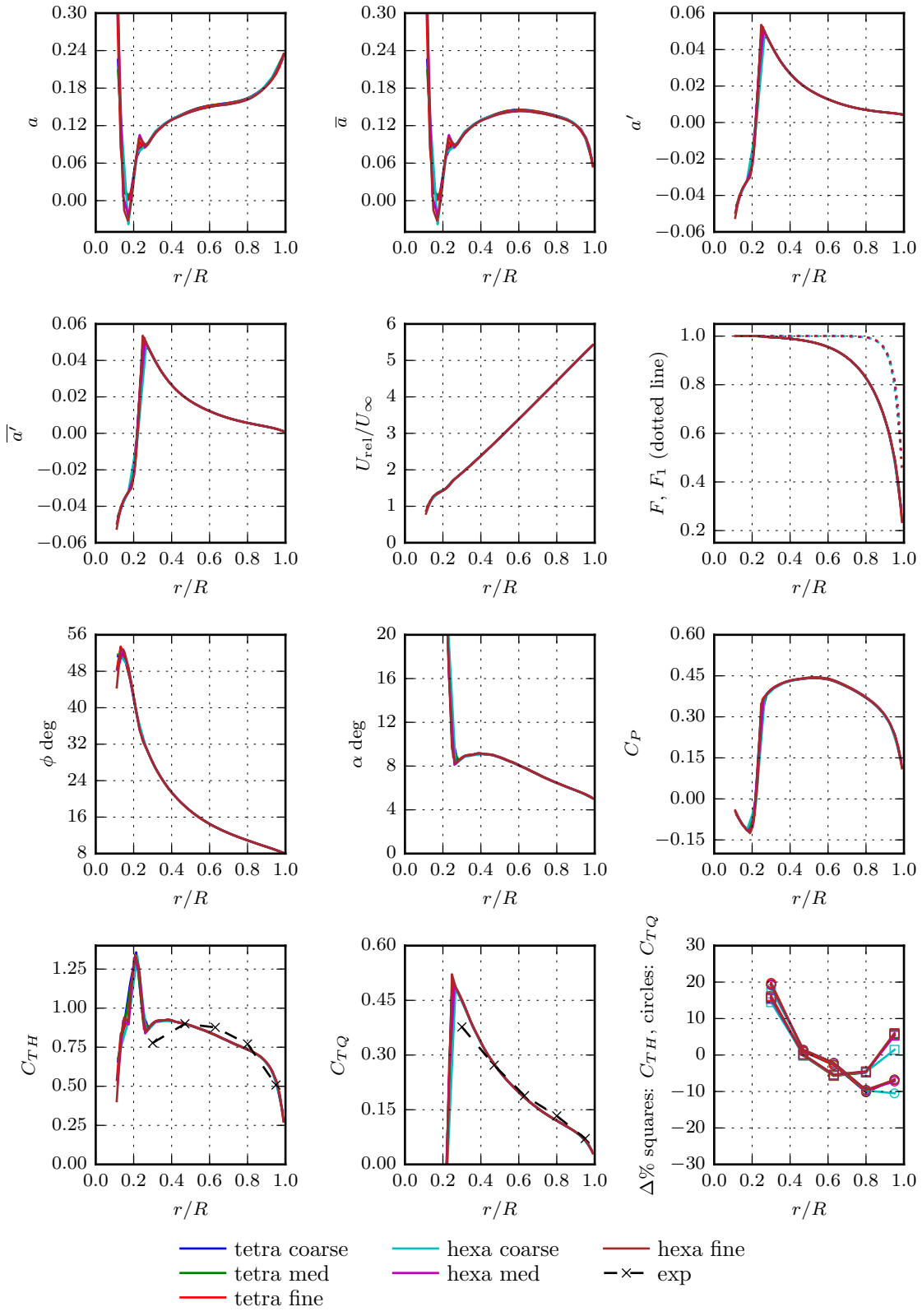


Figure 3.14: Radial outputs from AD using CSU $Re_c = 3 \cdot 10^5$ data on different grids, using the Shen model.

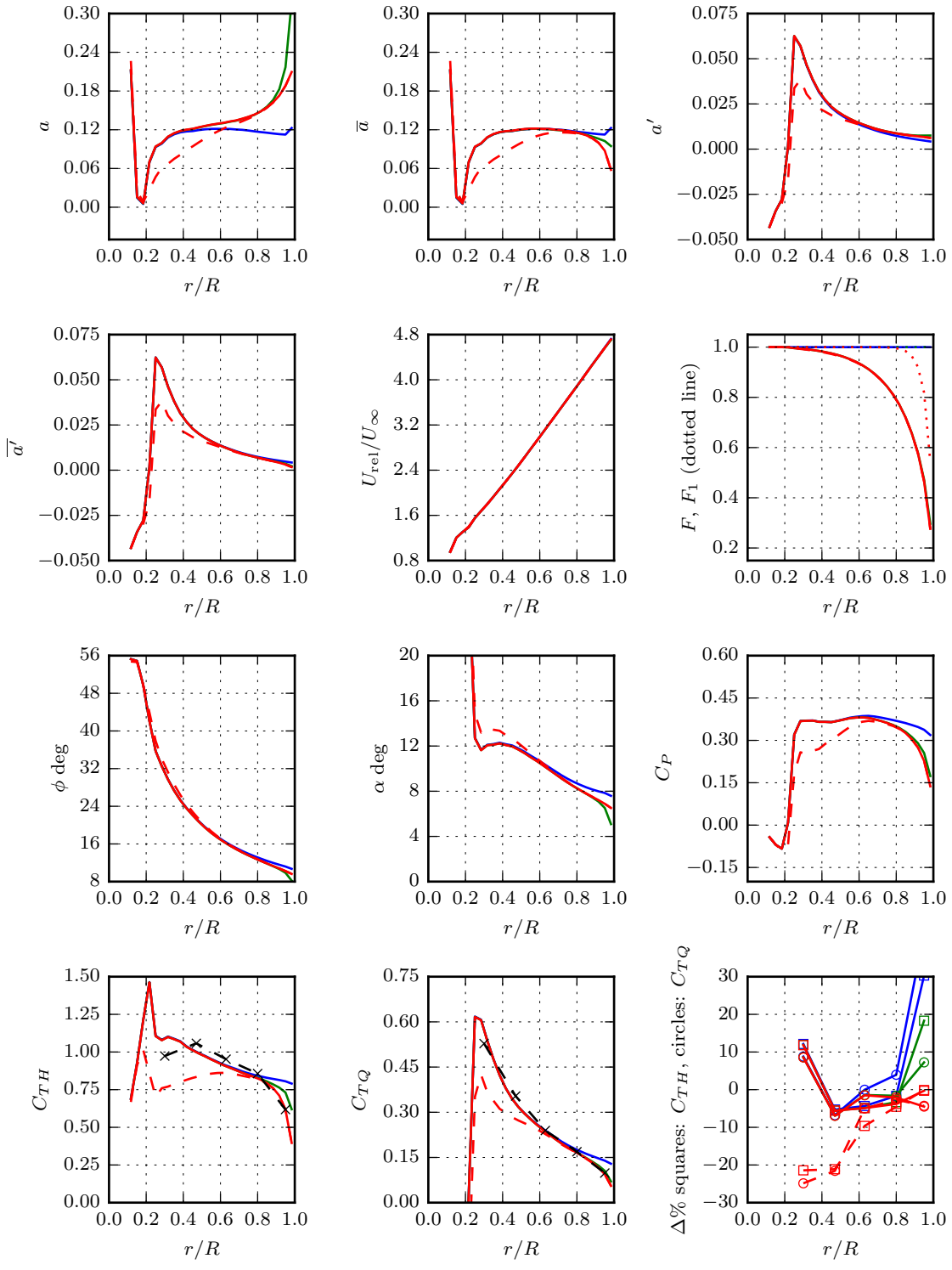


Figure 3.15: Radial outputs from AD using CSU $Re_c = 3 \cdot 10^5$ data, comparing no correction with the Glauert and Shen models (no, Gl, Sh). Dashed red line is without 3D aerofoil data correction, but with the Glauert and Shen models applied.

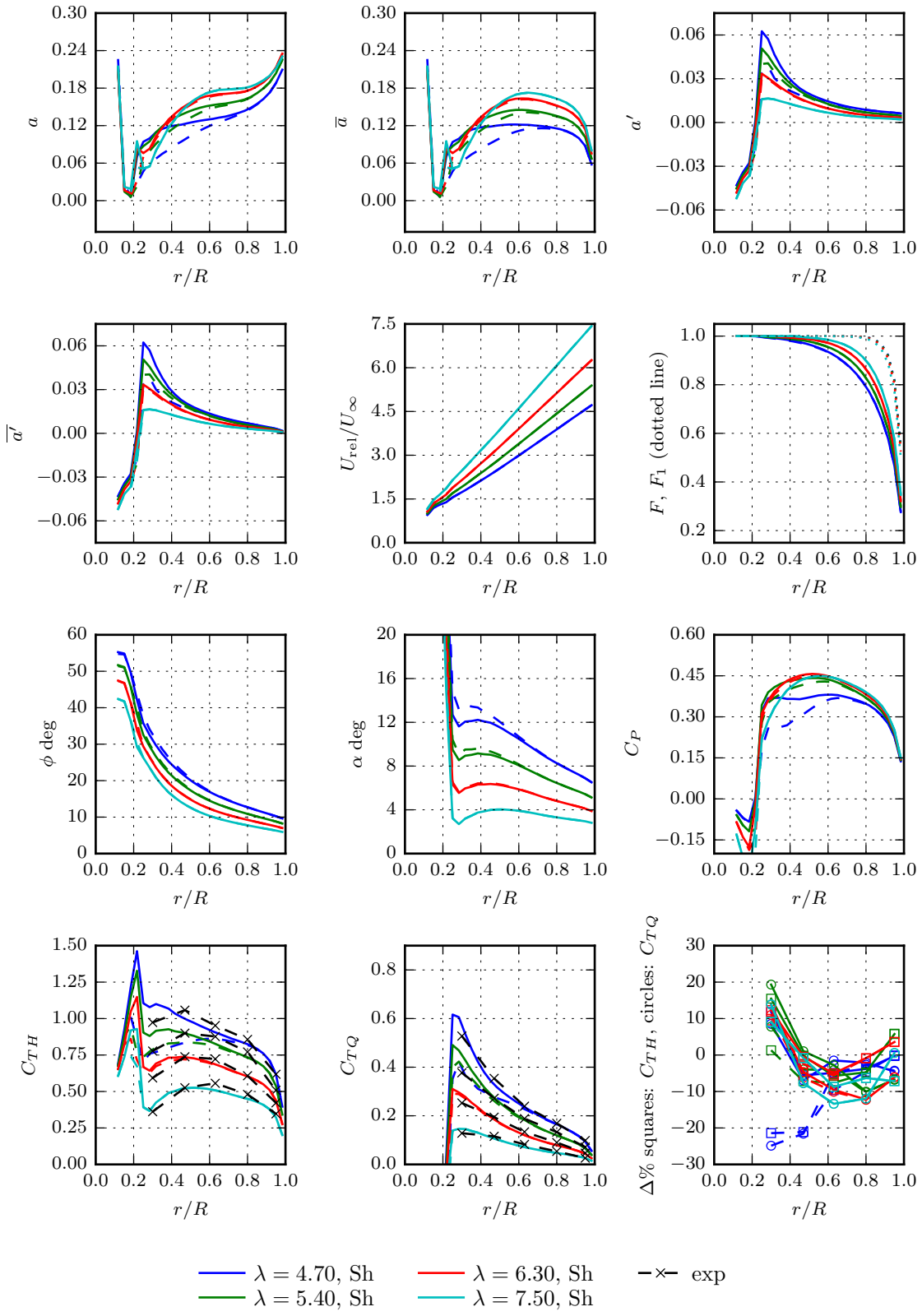


Figure 3.16: Radial outputs from AD using CSU $Re_c = 3 \cdot 10^5$ data at different tip-speed ratios. Dashed lines indicate the same cases simulated with uncorrected aerofoil data.

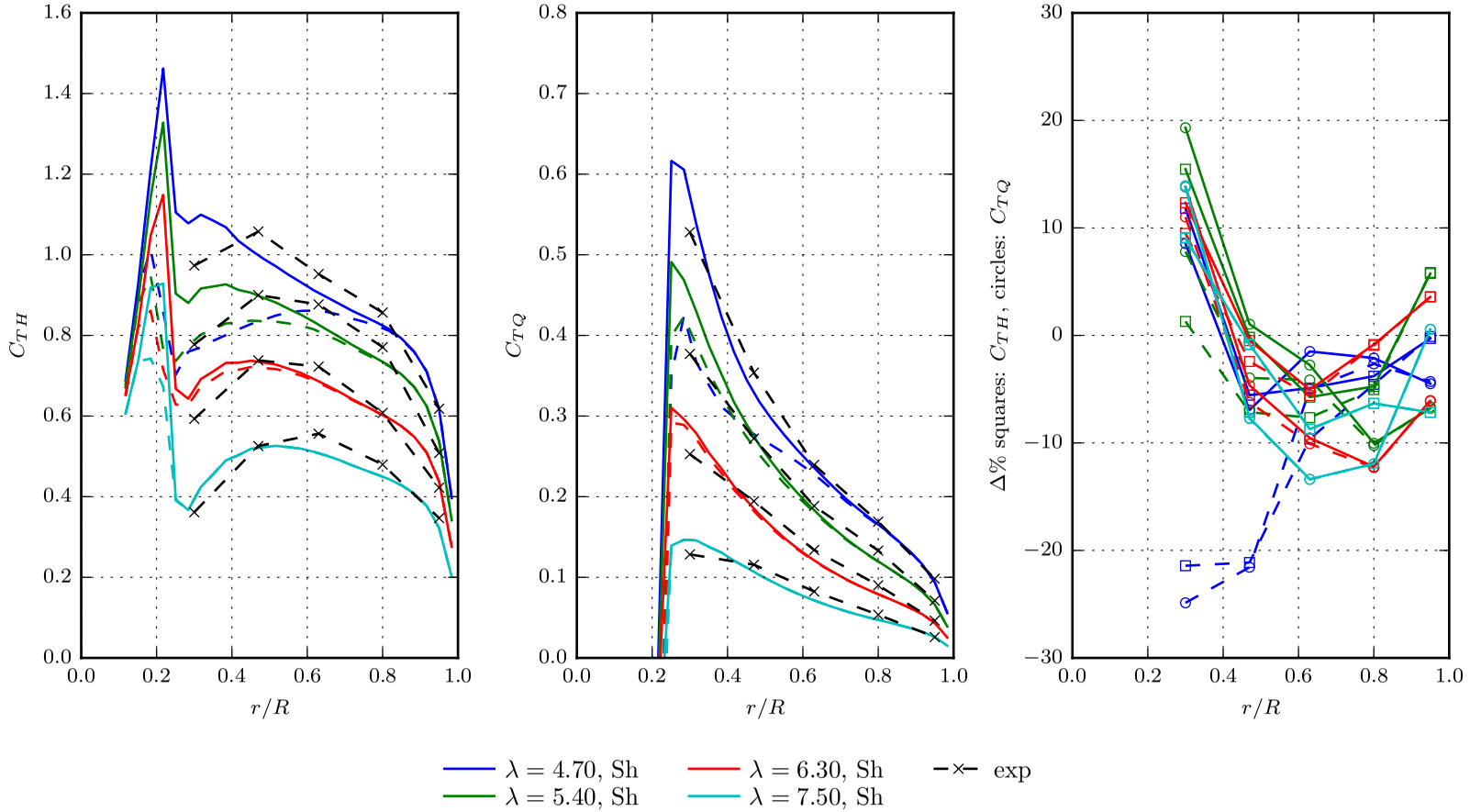


Figure 3.17: Radial outputs from AD using CSU $Re_c = 3 \cdot 10^5$ data at different TSRs. Modified thrust and torque coefficients $C_{TH} = \delta T/q2\pi r\delta r$, $C_{TQ} = \delta F_Q/q2\pi r\delta r$, where $q = \frac{1}{2}\rho[U_\infty^2 + (\Omega r)^2]$, and Δ shows the percent difference comparing simulation to experimental results.

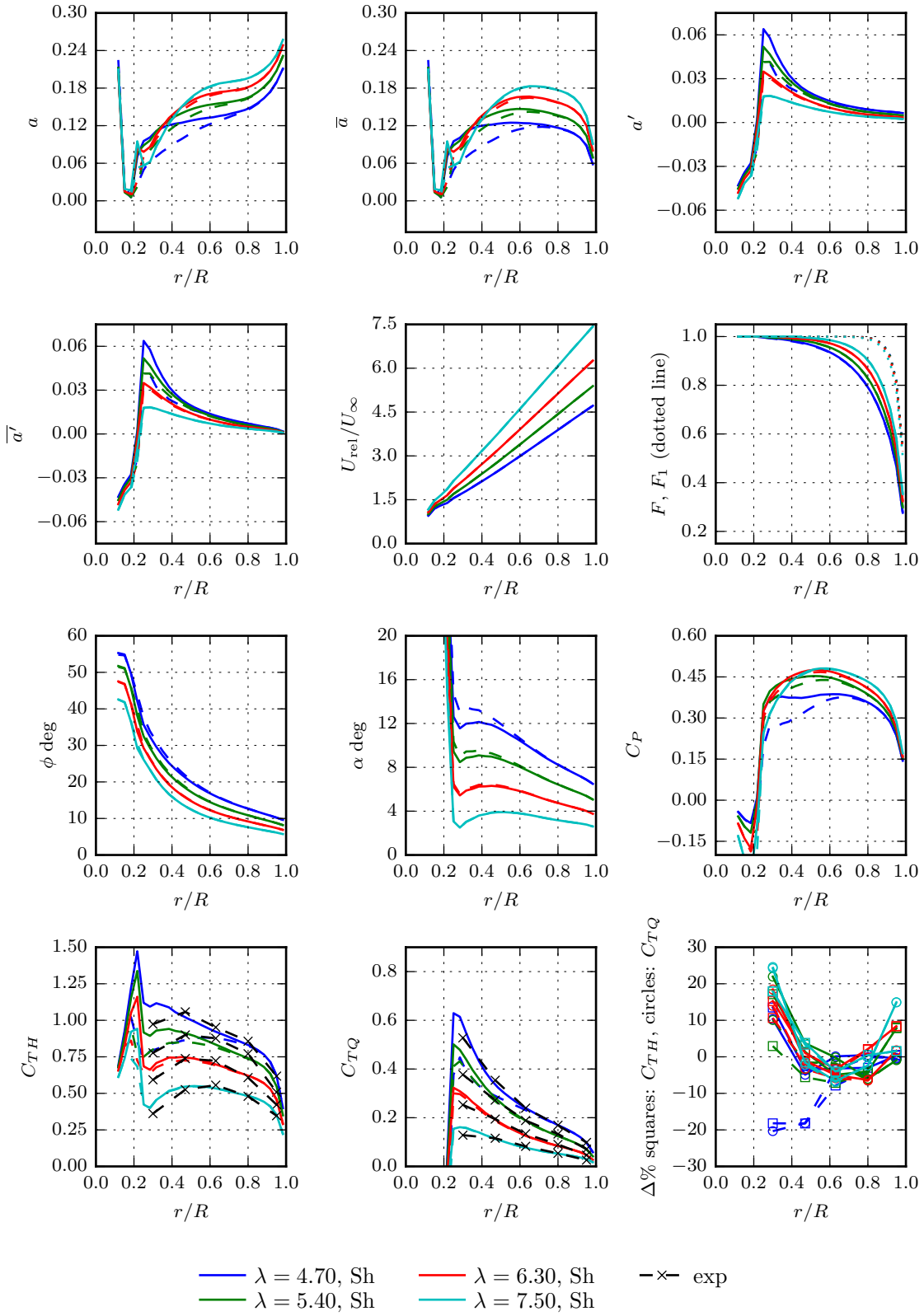


Figure 3.18: Radial outputs from AD using CSU $Re_c = 5 \cdot 10^5$ data at different TSRs.

Chapter 4

Hydrodynamic design of tidal turbines

The simple actuator disk discussed in previous chapters provides the most basic theoretical introduction to understanding the extraction of energy from a flow. The earliest usage of the idea is usually attributed to Froude [26], who conceived the idea to describe the effect of propulsion on the surrounding fluid as a step change of pressure. In the case of a ship propeller the increase of pressure is in the streamwise direction and the ship experiences a thrust in the opposite direction. Fluid is accelerated through the disk resulting in a contraction of the stream-tube passing through the edge of the disk between the undisturbed flow upstream and the disk, and continuing downstream of the disk. While the propeller contributes energy to the flow, all theoretical results of the actuator disk are applicable to rotors extracting energy from the flow if the disk is reversed. When a rotor exerts a thrust T against the flow direction, the flow is decelerated from the far upstream velocity U_∞ to the velocity at the disk U_D, in order to extract energy. As the thrust increases, less fluid interacts with the disk as more is diverted radially into the bypass. The extracted power can be calculated as $P = TU_D$, and control volume analysis can be used to show that a maximum 16/27 of the undisturbed kinetic energy flux through the disk area A can be extracted, when the lateral boundaries are far from the disk. The same limit applies to the contribution of power to fluid by a propeller as was first demonstrated by Lanchester [40] in the context of aeroplane propellers. The more famous derivation appeared several years later when Betz [7] independently applied the analysis in the context of wind turbines. The limit is generally known as the Betz limit for wind turbines, but in recognition of the historical development, many authors now refer to the Lanchester-Betz limit.

The simple actuator disk permits a single parameter to characterise its operation, a typical choice is the local axial thrust coefficient C_{TL} at the disk, which takes a value of 2 at the maximum $C_P = 16/27$ described above. However, the model offers no guidance on the geometry of a rotor that could achieve this performance, which would correspond to a design method. The previous chapter explained how blade element theory was introduced to the general momentum theory in order to characterise actual rotor blade sections. One result was the combined BEM theory presented by Glauert [30], who explained the evaluation of existing rotor geometries as well as a procedure for designing aeroplane propellers with optimum efficiency. Glauert briefly outlines how the developed methods are equally applicable to evaluation and design of wind turbine rotors with suitable reversal of variable sign, and this is now the principal application of the method. In the following section, a second approach is outlined, which originates from Prandtl's lifting line method for finite wings.

4.1 The lifting line method

Prior to the development of the BEM method, the approach to advance beyond the actuator disk description of propellers was motivated by the success of Prandtl's lifting line method for finite wings. In this method the wing or rotor blade is replaced by a line with a spanwise distribution of circulation, Γ. Like the BEM method, application of the lifting line method to rotors was originally in the context of propellers. While the BEM method was formulated for aeroplane propellers and now finds its dominant application in wind turbine design and evaluation, the lifting line method for rotors has remained in the field of propulsion and particularly ship propellers. Epps & Kimball [23] recently presented their unified lifting line theory, which has intentionally been reformulated to allow application to turbines and propellers with suitable variable sign reversal. As the present thesis is solely concerned with turbines, the theory is presented using notation consistent with the derivation of the BEM method in the previous chapter.

In a lifting line framework the lift force is now related to the circulation Γ using the Kutta-Joukowski relationship, rather than an empirical lift coefficient.

$$L = \rho U_{\text{rel}} \Gamma \tag{4.1}$$

The viscous drag force can be included using the empirical drag coefficient, with the drag force acting in the direction of the relative flow velocity U_{rel}, as was done in the

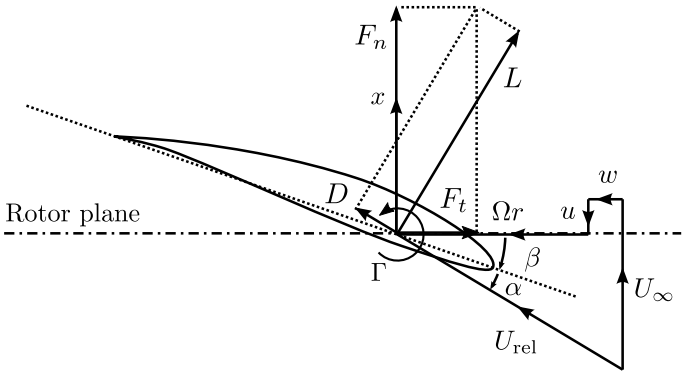


Figure 4.1: Turbine blade element for lifting line model.

BEM method:

$$D = \frac{1}{2}\rho U_{\text{rel}}^2 c C_D \tag{4.2}$$

The induced axial and rotational velocity, the resultant inflow velocity and its inflow angle to the rotor plane are defined in the same way as for the BEM method, as shown in Figure 4.1. The total thrust and torque are evaluated by integrating over the span of the blade and summing over the number of blades, Z:

$$T = \rho Z \int_{r_{\text{hub}}}^{R} \left[U_{\text{rel}} \Gamma \cos\phi + \frac{1}{2} U_{\text{rel}}^2 C_D c \sin\phi \right] \mathrm{d}r \tag{4.3}$$

$$Q = \rho Z \int_{r_{\text{hub}}}^{R} \left[U_{\text{rel}} \Gamma \sin\phi - \frac{1}{2} U_{\text{rel}}^2 C_D c \cos\phi \right] r \, \mathrm{d}r \tag{4.4}$$

Following Helmholtz's theorems for vorticity elements in an inviscid fluid, spanwise variation of Γ will result in a sheet of vorticity being shed at the lifting line and convected downstream. This can be modelled by a discrete number of horseshoe vortices. (A horseshoe vortex is a line vortex of constant strength whose mid-section forms a discrete length of the lifting line while vortex filaments trail from each end). In the general case, the Biot-Savart Law is used to calculate the velocity induced at the rotor plane by the vorticity in the wake. The velocity at each control point on the lifting line would require numerical integration over all the vorticity in the wake, which becomes computationally expensive for a well resolved wake. For a purely helical wake of vortex filaments, analytical solutions are available in terms of infinite series of modified Bessel functions [31], however these converge relatively slowly. Fortunately, highly accurate asymptotic formulas for the sums of Bessel functions exist, which are attributed to Wrench [78]. The formulas of Wrench are in closed form and straightforward to evaluate but are rather lengthy to be repeated here, they can

be found in Kerwin & Hadler [39]. In the numerical implementation, the induced velocities are calculated at M control points, $r_c(m)$, $(m = 1..M)$ on the lifting line:

$$u(m) = \sum_{n=1}^{M} \hat{u}(m,n)\Gamma(n) \tag{4.5}$$

where $\hat{u}(m,n)$ is the axial velocity induced at the m^{th} collocation point, $r_c(m)$, by a horseshoe vortex of unit strength surrounding $r_c(n)$, calculated with the help of the formulas of Wrench. A similar calculation returns the rotational velocity $w(m)$. Given $u(m)$ and $w(m)$, the relative velocity magnitude U_{rel} and flow angle at the blade ϕ follow from the diagram in Figure 4.1 and are therefore identical to Eqs. 3.1 and 3.4.

Now that integrated thrust and torque can be evaluated in terms of the induced velocity at the rotor, and hence in terms of the blade loading Γ, the rotor design is optimised by finding the circulation distribution that maximises the rotor torque:

$$\frac{\partial Q}{\partial \Gamma} = 0 \tag{4.6}$$

where the total torque Q produced by each rotor blade is calculated by summing the contribution from each discrete length, Δr_v, of the lifting line:

$$\frac{Q}{\rho Z} = \sum_{m=1}^{M} \left\langle \left\{ [U_\infty - u]\Gamma - \tfrac{1}{2} U_{\text{rel}} C_D c [\Omega r_c + w] \right\} r_c \Delta r_v \right\rangle_m \tag{4.7}$$

No constraint is placed on the thrust.

While previous lifting line implementations were unable to predict the theoretical maximum $C_P = 16/27$ from momentum theory, Epps & Kimball [23] present necessary constraints on the design problem, which lead to agreement with momentum theory. First it can be shown that the BEM theory in the previous chapter inherently assumes that the induced velocity is perpendicular to the resultant inflow:

$$(\tan\phi \equiv) \frac{U_\infty - \overline{u}}{\Omega r + \overline{w}} = \frac{\overline{w}}{\overline{u}} \tag{4.8}$$

where $\overline{u}$ and $\overline{w}$ are the annulus averaged induced velocities. This means that momentum theory inherently assumes a non-expanding constant pitch helical wake, the necessary condition for minimum induced losses as shown by Betz. (This does not affect the expansion of the stream tube passing the edge of the disk due to the axial deceleration of the fluid.) In the numerical implementation with discrete vortices, this can be implemented as the following design constraint:

$$\frac{\partial u(i)}{\partial w(i)} = \frac{\Omega r_c(i) + 2w(i)}{U_\infty - 2u(i)} \tag{4.9}$$

The second alteration is applied to calculation of the induced velocities from the Wrench formulas. As momentum theory necessarily assumes no interaction between annuli, the induced velocity at one radius should be independent of the circulation at other radii. As a result, the summation of Eq. 4.5 is simplified to

$$\begin{aligned} &\hat{u}(m,i) \approx 0 \quad (\text{for } m \neq i) \\ &u(i) \approx \hat{u}(i,i)\Gamma(i) \end{aligned} \tag{4.10}$$

and similarly for $w(i)$. The constraints of Eqs. 4.9 and 4.10 are incorporated into the overall optimisation problem of Eq. 4.6 to form the following set of M equations for each discrete radial location which are solved using a Newton solver.

$$\begin{aligned} &(U_\infty - u(i)) \\ &+ \tfrac{\partial u(i)}{\partial w(i)} w(i) \\ &+ \tfrac{1}{2} C_D(i) c(i) \tfrac{\partial U_{\text{rel}}(i)}{\partial \Gamma(i)} [\Omega r_c(i) + w(i)] \\ &+ \tfrac{1}{2} C_D(i) c(i) U_{\text{rel}}(i) [\hat{w}(i,i)] = 0 \quad \text{for } i = 1..M \end{aligned} \tag{4.11}$$

Further details of this method and indeed the application to propellers are found in [23] as well as in the code of the open source implementation [22] used in this study.

Once the aerofoil section of the rotor blade is chosen, the design angle of attack, and hence design C_L is normally where the section has the greatest lift-to-drag ratio ($\max C_L/C_D$, cf. Figure 3.5), which will be called α_{LD}. The solution of Eq. 4.11 requires as inputs the design C_L and corresponding C_L/C_D, and returns the circulation distribution and induced velocity along the blade, as well as the local chord length, c, which is related to the circulation as:

$$c = \frac{2\Gamma}{C_L U_{\text{rel}}} \tag{4.12}$$

The induced velocities allow the flow angle at the blade to be calculated using Eq. 4.8, and the local blade twist is found as $\beta = \phi - \alpha_{LD}$.

4.2 RANS actuator disk design method

As mentioned in the introduction, the BEM method represents a different approach to the investigation of real rotor geometries. The analytical BEM method was derived in the previous chapter, it was then adapted as an internal boundary condition for a RANS CFD solver, and the model was validated using experimental data from

a wind tunnel wind turbine test. It is clear that this analysis method can also be used as a design method given a suitable target function and design constraints. The historical development of the two approaches to rotor evaluation and design suggests that the BEM method was formulated as a engineering tool to circumvent the complex evaluation of the circulation distribution and induced velocity at the blade in the lifting line method. This problem was partly solved with the arrival of the formulas of Wrench, although further methods were required to successfully assess off-design conditions [23]. Nonetheless, the BEM method continues to be widely used, even if a number of empirical and semi-empirical corrections had to be added to achieve sufficient accuracy. Compared to the lifting line design tool, the RANS embedded BEM design method offers the potential to account naturally for the effect of blockage and freestream turbulence on the rotor design directly, which is important for tidal turbines. In this section some of the corrections, which are relevant to the current study, are discussed, then the target function and design constraints are discussed and compared to the lifting line method.

4.2.1 Corrections applied to the blade element momentum method

Section 3.1 introduced a number of corrections that are required in addition to equating the differential expressions of thrust and torque from momentum theory and blade element theory. There exist corrections for complex flow situations such as yawed and dynamic inflow, as well as where the inviscid assumption breaks down in the analytical BEM method, see e.g. [11], but the current thesis is only concerned with turbines in steady, uniform flow normal to the rotor plane. For this case, corrections have been developed which are principally active either close to the rotor hub or close to the blade tips, suggesting that the BEM method delivers acceptable accuracy in the region in between. The models for generating aerofoil data from 2D polars principally augment the post-stall C_L towards the hub but, as shown in Figure 3.6, C_L is also reduced at the tips. Other models aim to correct for the effect of centrifugal forces on the mass flux close to the hub [43], or the effect of a root hub vortex on the induction close to the hub [47]. However, the behaviour near the hub is likely to be strongly dependent on details of the nacelle and hub-blade connection, and a detailed understanding of the flow in this region might only be possible using CFD studies of the actual geometry, see e.g. [36]. Due to the small fraction of the swept area of the rotor, as well as the short distance from the centre of rotation, the contribution of blade elements close to the hub to the total thrust and particularly torque is relatively

small. Therefore, more models have been developed to correct either the flow or the forces near the rotor blade tips, where accurate predictions contribute significantly to the accuracy of total predicted power and loads. This discussion is intended to highlight the fact that the models are generally applied in combination with each other, which makes validation of any one of them difficult.

The earliest correction was Prandtl's tip-loss factor for rotors with a finite number of blades. Prandtl's result is an exact solution to an approximate formulation of the problem of the velocity induced at the rotor plane by the wake of an optimum rotor (minimum induced drag). The result approaches Goldstein's solution to the exact problem more closely for a high number of blades, Z, or high tip-speed ratio, λ. For commercial three-bladed wind turbines, which often have a design tip-speed ratio of $\lambda = 7..10$, the accuracy of Prandtl's solution is acceptable. Tidal turbines will need to operate at lower tip-speed ratios to avoid cavitation, for a two-bladed rotor at $\lambda = 5$, the difference between Prandtl's and Goldstein's solution is ca. 6%. In the momentum theory expressions of the analytical BEM method, Prandtl's factor is typically only used to correct the induction factor in the momentum flux terms but not the mass flows. This is done solely for numerical convenience of the resulting expressions, but leads to the orthogonality condition of Eq. 4.8 being broken. Shen et al. follow the earlier study of de Vries [13], who recommends that both occurrences of the induction factor in Eqs. 3.19 and 3.20 are corrected, as well as neglecting higher order terms (setting ϵ_1 and ϵ_2 to unity in Section 3.1). While this results in more complicated expressions in the analytical BEM method, it is the simplest approach in the embedded RANS model as $\overline{a}$ and $\overline{a'}$ returned by the solver are simply corrected once to blade induction factors for the blade element calculation.

The Shen force correction factor, F_1, was developed in combination with the interpretation of the Prandtl correction just discussed. It is a semi-empirical model, which has been tuned to the results of two experimental datasets for the analytical BEM method. One of the experiments is the NREL Phase VI experiment used in the previous chapter. In their BEM simulations, Shen et al. used the DUT $Re_c = 1 \cdot 10^6$ aerofoil dataset, with rotational augmentation corrected using a modified application of the model of Snel & van Holten[65]. The second experimental dataset comes from the measurement of a 5.35m diameter wind turbine in the China Aerodynamics Research and Development Center (CARDC) wind tunnel, also two-bladed, details of which can be found in Ronsten [59]. In both cases, Shen et al.[62] compared modelled and measured radial local thrust coefficients, non-dimensionalized using the dynamic

pressure $q = \frac{1}{2}\rho[U_\infty^2 + (\Omega r)^2]$. This is identical to the definition of C_{TH} in the previous chapter. The blockage in the two experiments, defined as the ratio of the swept area of the turbine, A, to the channel cross sectional area, C, was 0.089 and 0.12 for the NREL and CARDC experiments, respectively. In both experiments, the effect of blockage was assessed with respect to the free-stream velocity correction required to translate the thrust results to unblocked conditions, i.e. $U_\infty = U_{\infty,\text{u.}}(1 + \Delta U/U_{\infty,\text{u.}})$, where subscript u. stands for 'uncorrected' and $\Delta U/U_{\infty,\text{u.}} = f(C_{T,\text{u.}})$. In the NREL experiment, it was deemed that no correction was necessary as $\Delta U/U_{\infty,\text{u.}}$ was well below 1% in all cases, according to an adaption of the momentum method outlined for propeller testing in Glauert [30]. In the CARDC experiment, $\Delta U/U_{\infty,\text{u.}}$ was evaluated using the wall "Wall pressure Signature Matrix" method and was applied to the results. Due to the dominance of the rotational velocity in $q = \frac{1}{2}\rho[U_\infty^2 + (\Omega r)^2]$ however, the results of C_{TH} (and C_{TQ}) are almost insensitive to corrections of U_∞, although the corresponding tip-speed ratio changes as $\lambda = \lambda_{\text{u.}}/(1 + \Delta U/U_{\infty,\text{u.}})$. As a result, for the comparisons (and presumably coefficient fitting) presented, Shen et al.[62] used the unaltered reported values of C_{TH} from each experiment, but with the corrected corresponding λ from the CARDC experiment in combination with their implementation of the analytical BEM method, which assumes unblocked flow.

In a companion paper, Shen et al. [63] suggest that the factor F_1 is equally applicable to actuator disks (AD) and lines (AL) embedded in CFD codes. They present a comparison of a 2D axisymmetric AD model, a (3D) AL model and the analytical BEM results described previously. While the inclusion of the F_1 correction factor generally led to better agreement with the experimental results, significant deviation between the methods was loosely attributed to failings in the generation of the aerofoil data. Numerous studies, in addition to the results of the previous chapter, agree that the aerofoil data provides one of the greatest uncertainties in blade-element type rotor analyses, however it also seems likely that correction factors like F_1 may require different fitting coefficients in CFD actuator models compared to analytical BEM. Madsen et al. [43] (with a correction in Døssing et al. [14]) present a model to account for the reduction of mass flow at the tips due to streamtube expansion in the analytical BEM method. In their model the reduction in streamwise velocity is related empirically to the radial flow velocity. As the radial velocity is not naturally included in the analytical BEM method, it is estimated using the linearized Euler solution for a two dimensional actuator disk, while radial flow and streamtube expansion are captured naturally in the CFD AD method. The analysis of Shen et al. did

not include any corrections between the analytical momentum balance and the CFD calculation.

4.2.2 RANS actuator disk design method and constraints

Performing a numerical optimization of the loading distribution to achieve maximum torque as in the lifting line method would be computationally too expensive for the CFD AD method as every Newton iteration would required a separate converged solution of the discretized flow field. As in the Lifting Line (LL) method, the design tip-speed ratio, $C_L(\alpha_{LD})$ and C_L/C_D are set, and the desired output variables are the blade taper and twist corresponding to the rotor design with maximum C_P. The maximum C_P of any design corresponds to a particular C_T where the flow is decelerated just sufficiently to extract the maximum energy before diverting too much fluid into the bypass. In the case of a simple actuator disk without blade element theory, it is found that C_T varies radially across the disk at the maximum C_P, but that the maximum C_P is achieved when the thrust coefficient based on the local velocity at the disk, $C_{TL} = T/\frac{1}{2}\rho[U_\infty(1-\overline{a})]^2$, is uniform across the disk. This is an empirical result which can easily be verified using CFD. As a result, the search for the rotor design with maximum C_P reduces to optimizing with respect to a single variable: C_{TL}, which is identical to the definition of K in Chapter 2. The optimum K from LMADT can provide a good starting value, and the optimum design is estimated by running simulations for a range of K surrounding the maximum C_P, and interpolating if necessary. In addition to the AD 'evaluation' model of the previous chapter, this 'design' process can be integrated into the iteration loop by updating the blade taper and twist to achieve the desired C_{TL}^{target} and α_{LD}. C_{TL} is calculated from the AD variables as:

$$C_{TL} = \sigma(C_L\cos\phi + C_D\sin\phi)\left(\frac{U_{\text{rel}}}{U_\infty(1-\overline{a})}\right)^2 \tag{4.13}$$

so the adjustment of taper and twist can be implemented as:

$$\sigma^{\text{new}} = \sigma^{\text{old}} + g_1 \cdot \frac{C_{TL}^{\text{target}} - C_{TL}^{\text{old}}}{(C_L\cos\phi + C_D\sin\phi)\left(\frac{U_{\text{rel}}}{U_\infty(1-\overline{a})}\right)^2} \tag{4.14}$$

$$\beta^{\text{new}} = \beta^{\text{old}} + g_2 \cdot (\alpha^{\text{target}} - \alpha^{\text{old}}) \tag{4.15}$$

where g_1 and g_2 are gain factors set at 0.05 and -0.05, respectively in the current study. Evidently, the denominator of Eq. 4.14, while physically consistent, may be considered as a variable part of g_1, and has no effect on the converged solution. The relatively small gain factors are chosen to ensure stability, the solution of the flow

field typically requires several thousand iterations which means that the rotor design problem easily converges. This design method was motivated by ideas presented by McIntosh et al. [45] but the author wishes to point out that this is an entirely new implementation.

The CFD AD method described in this thesis uses blade element theory to relate momentum changes in the flow to aerodynamic forces of rotor blades. However, due to the azimuthal averaging of these forces, the AD boundary condition still appears to the CFD solver as a simple actuator disk with a step change in pressure, albeit now with radial variation of thrust and imposition of rotational velocity downstream of the disk. Therefore, as described above, targeting a uniform local thrust coefficient across the disk in the design loop, e.g. $C_{TL} = 2$ for an unblocked flow, would indeed return the greatest C_P. However, an actual rotor with a finite number of blades, operating at a finite tip-speed ratio, is unable to achieve the loading of an actuator disk and this must be taken into account when defining C_{TL}^{target}. The choice of C_{TL}^{target} for the design of finitely bladed rotors, running at a finite tip-speed ratio, is discussed in the following section.

4.3 Designing for unblocked flow

The lifting line rotor design method described in Section 4.1 is faster than the CFD AD method by several orders of magnitude and it is used here to quickly demonstrate some aspects of the design space for rotors. All of these results can be verified with suitable application of general momentum theory. The combined effects of design tip-speed ratio λ, blade number Z, and C_D/C_L ratio on the C_P of the rotor design are shown in Figure 4.2, where each circle represents a unique turbine design (rather than an operating point of a single design). The dashed black line indicates the Betz limit, which is valid for an infinite number of blades and neglects the loss of kinetic energy in the rotating wake, while the blue points show the analytical AD solution including losses due to wake rotation and blade drag [72], for $C_D/C_L = \{0, 0.01, 0.02\}$. (Figure 3.6 shows typical C_L/C_D ratios for suitable aerofoils of around 100, or $C_D/C_L = 0.01$.)

The green and red points show the result of lifting line optimisation method detailed in Section 4.1, for which the number of blades, Z, is set to 100, as an approximation of the theoretical case of a rotor with infinite blades, and 3, for typical wind (or tidal) turbine design. The lifting line solution for $Z = 100$ is seen to closely approximate the analytical AD solution across all tip-speed ratios and C_D/C_L, which

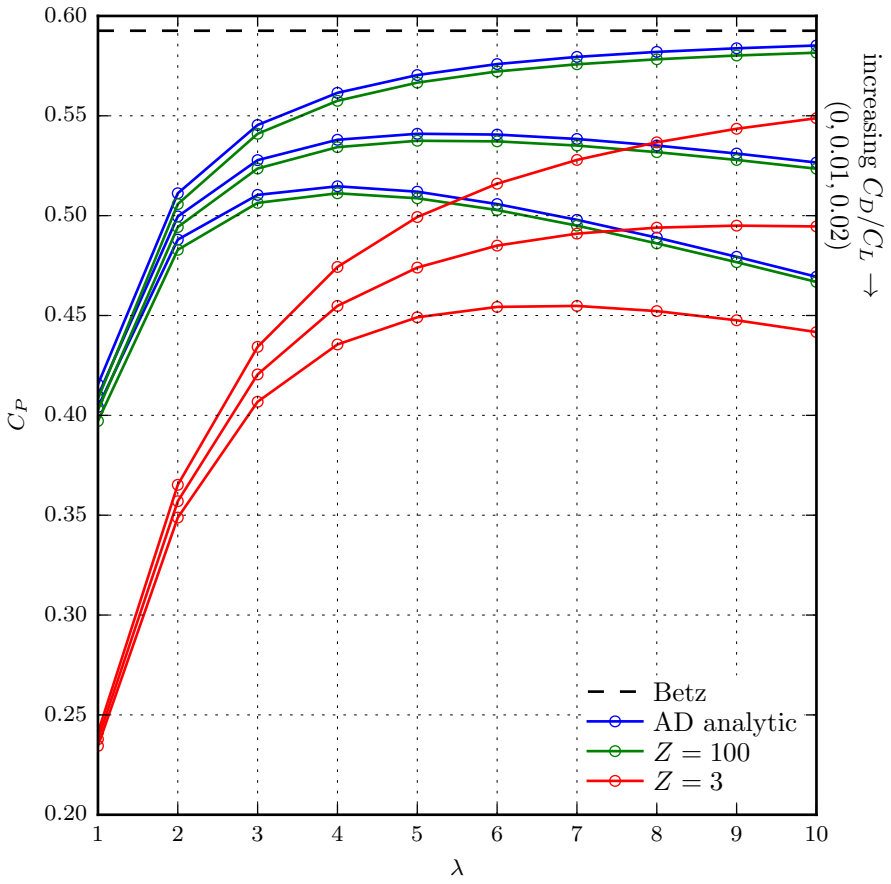


Figure 4.2: $C_{P\max}$ predicted by the OpenProp unified lifting line method for a range of design λ, blade number Z, and lift to drag ratios C_L/C_D. Each circle represents a unique rotor design.

both validates and verifies the OpenProp implementation. The top line is the case with zero drag, which tends to the Betz limit as $\lambda \to \infty$, but C_P falls quickly for lower λ, as more energy is lost to driving the wake rotation. The inclusion of drag, on the other hand, becomes more detrimental to C_P as the U_{rel} at the blade element increases, which scales almost with λ. In all cases where drag is included, there is an optimum λ achieving the highest C_P, which becomes smaller and moves to lower tip-speed ratios as C_D/C_L increases.

The corresponding rotor designs for $Z = 3$ have a lower C_P than the quasi infinitely bladed rotors. In the BEM method, this is a direct consequence of including Prandtl's tip loss factor, cf. Sections 4.2.2 and 3.1. The lifting line method naturally accounts for the azimuthal variation of induction at the rotor plane due to the effect of a finite number of trailed helical vortex sheets in the wake. While three-bladed wind turbines

may be designed to achieve maximum C_P at $\lambda = 7..10$, tidal turbines are limited by the risk of cavitation to perhaps $\lambda = 4.5$, depending on the submersion depth below the free surface. Evidently, unblocked tidal turbines (considering realistic C_L/C_D) have a theoretical limit of just over $C_P = 0.45$, whereas the limit may be closer to $C_P = 0.5$ for wind turbines. However, these results cannot account for either blockage effects or the momentum mixing effect of freestream turbulence, which may both be considerable in tidal turbine operation.

Figure 4.3 shows the now familiar grid of plots related to the CFD AD model, but these variables have been extracted from the lifting line solution for an optimum rotor at $\lambda = 4.5$, with $Z = 3, 6, 9$ and $Z = 100$ blades. Realistic aerofoil $C_L(\alpha_{LD}) = 1.08$ at $\alpha_{LD} = 6$ deg and $C_L/C_D = 90$ have been used. For the cases with $Z = 3$ and $Z = 100$, each set of curves would correspond to one circle on Figure 4.2 at $\lambda = 4.5$, approximately at the intermediate level of drag. The intermediate cases with $Z = 6, 9$ are not practical designs due to their low C_P, they have only been included to demonstrate trends and will be discussed below. The lifting line algorithm naturally returns the induced axial and rotational velocities at the blade (or lifting line control points), the annulus average values have been calculated using Prandtl's result, Eq. 3.22. Together with the flow angle ϕ, all the required velocity components can be recovered and the axial force presented as C_T non-dimensionalized using $\frac{1}{2}\rho U_\infty^2$ or C_{TL} using $\frac{1}{2}\rho[U_\infty(1-\overline{a})]^2$. The radial variation of all variables will be compared to the CFD AD design results in the following section, but the radial distribution of the thrust coefficients is discussed here.

Firstly, it is reassuring that the quasi-infinitely bladed case, $Z = 100$ approaches the results from general momentum theory of $C_T = 8/9$ and $C_{TL} = 2$ for an optimum Betz rotor (the inclusion of wake rotation and blade drag means that C_P is lower than the Betz limit). At radial stations $0.3 < r/R < 1.0$, C_T and C_{TL} are lower but remain within 2% and 5%, respectively, of the values from momentum theory. For both $Z = 3$ and $Z = 100$, the thrust loading at the hub increases relative to the solution from general momentum theory. For the current designs, a hub radius of $r/R = 0.1$ was used and the lifting line method uses image vorticity to model the effect of the hub boundary.

Secondly, for the 3-bladed rotor, the lifting line solution shows that the Betz optimum condition naturally unloads the rotor as $r/R \to 1$. This offers some guidance on the correct distribution of C_{TL}^{target} to use in the CFD AD design method described in the previous section. It is observed visually that the profile of C_{TL}, and the trend with respect to Z, is not dissimilar to that of F, which may not be surprising as the

original definition of the tip loss factor relates the circulation strength (or loading) of a finitely bladed rotor to an infinitely bladed rotor, cf. Eq 3.25. Even ignoring drag temporarily, it is clear from the Kutta-Joukowski relation (Eq. 4.1) that the profiles of relative velocity at the blade, annulus averaged axial velocities as well as the flow angle are required to relate Γ to C_{TL}. However, by overlaying the plot of C_{TL} over r/R in Figure 4.3, a striking agreement was found with the function const.$\cdot F^2$, where the constant is selected to match the LL solution at $r/R \approx 0.4$ (where F is effectively unity). This approach is demonstrated by the dashed lines in the plot of C_{TL}, the constants c_1, c_2 and c_3 have all been set, without further rigour, to 1.9. Neglecting radial stations close to the hub, where the hub image vortex system is active, the close agreement between the LL solution and this simple expression involving Prandtl's tip-loss factor permit optimism that this may be a leading order solution from lifting line theory. Such analysis must unfortunately be postponed to appear in future studies. For the design of three-bladed rotors using the AD method outlined in Section 4.2.2, the profile

$$C_{TL}^{\text{target}} = C_{TL,\text{nom.}}^{\text{target}} \cdot F^2 \tag{4.16}$$

will be used, where 'nom.' indicates a nominal value. The nominal design C_{TL} is used for the presentation of results below, but the 'nom.' subscript is dropped for brevity.

4.3.1 Rotor design

The overall aim of this thesis is to present a method for designing tidal turbines which could be operated in tidal channel conditions like those of the array study in Chapter 2. In the array study, turbines were installed in a channel of depth $2D$ and width $10nD$, where n is the number of turbines. In order to achieve realistic Reynolds numbers on the scale of the turbine, the turbine diameter was $D = 20$m, operating in a channel with uniform inlet velocity of $U_\infty = 2$m/s and the fluid properties were of water. The freestream turbulence intensity at the rotorplane was $TI = 5\%$.

In order to allow comparison with the lifting line method and results from general momentum theory, this section begins with the rotor design for a turbine in a quasi-unblocked flow, with low freestream turbulence, using the CFD AD method as described above in Section 4.1. Compared to paragraph above, the blockage ratio is reduced to $B = 0.005$ with the turbine at the centre of a domain with square cross section, the freestream turbulence intensity is below 1%, and a hub radius of diameter D/10 is defined. While the CFD AD design loop relies on all the details of Section 3.1 for rotor evaluation, including extrapolated and corrected aerofoil data,

the converged design evidently only depends on the values of $C_L(\alpha_{LD})$ and corresponding C_L/C_D. For all designs shown in this chapter, the aerofoil section used is the RISØ-A1-24, which is a 24% thickness aerofoil intended for medium scale commercial wind turbines. This is a simplification as the thickness to chord ratio, t/c, of turbine blades generally decreases (a different aerofoil section is used) as $r/R \to 1$. Like other aerofoil families designed specifically for wind turbine application (NREL S-series, DU-series), the RISØ family consist of parametric curves which have been optimised using viscous-inviscid solvers (Xfoil or similar), with various target functions, but always including a smooth stall behaviour and insensitivity to leading edge roughness. $C_L(\alpha_{LD})$ and C_L/C_D are approximately constant across the span, as the 3D correction models only start to affect the data at angles of attack just below stall. Using $C_L(\alpha_{LD}) = 1.08$ at $\alpha_{LD} = 6$ deg and corresponding $C_L/C_D = 90$, a rotor is also designed using the lifting line method to compare with the AD design.

It is easy to estimate the minimum submersion depth of the turbine to avoid cavitation for a given tip-speed ratio by applying Bernoulli's equation.

$$\Delta y > \frac{-C_{\text{pres,min}}\left[U_\infty^2(1+\lambda^2)\right]}{2g} - \frac{p_{\text{atm}} - p_v}{\rho g} \tag{4.17}$$

where $C_{\text{pres,min}}$ is the minimum pressure coefficient at the blade tip. For a peak channel flow speed of $U_\infty = 2.5$ m/s, tip-speed ratio $\lambda = 4.5$, and $C_{\text{pres,min}} = -2$, Eq. 4.17 requires that the highest point of the turbine blade is at least 3.47 m below the free surface. Higher λ would limit safe turbine operation to greater submersion depths, while reducing λ increases blade loading and reduces the theoretical efficiency limit as shown in Figure 4.2. Therefore, $\lambda = 4.5$ is chosen as the design tip-speed ratio for all designs presented in this chapter.

Figure 4.4 demonstrates the iterative search for the optimum design using the CFD AD method. Each point represents an individual turbine design, λ is constant, but C_{TL} (nominal, cf. previous section) is varied in steps until the trend around the optimum design is clear. Using a cubic spline interpolation of the results, the location of the optimum design (maximum C_P) is estimated and indicated by the black crosses. For comparison, the dashed line labelled 'PJ' is for a simple actuator disk ('porous jump'), like the one used in the array studies of Chapter 2, but now including a hub. Momentum theory predicts that the simple actuator disk achieves the Betz limit of $C_P = 0.593$, at $C_{TL} = 2.0$ and $C_T = 8/9$. The RANS solution agrees well with this (0.594, 1.97, 0.883), the 1% area fraction occupied by the hub reduces the power producing area of the rotor but appears to compensate almost equally by accelerating the flow past the hub. The lines labelled 'Glauert' and 'Shen' indicate inclusion of

the factor F, and F_1 in combination with F, respectively, as in the preceding chapter. 'Tip Constraint (TC)' indicates an additional constraint on the design process which will be introduced below. It is seen that these three cases lead to almost identical results as the lines obscure each other in Figure 4.4. The effect of Shen's F_1 correction factor, which is used in the evaluation part of the design loop becomes very small as C_{TL}^{target} approaches zero at $r/R \to 1$ much faster than F_1. (The simulation with no tip correction, labelled 'no', i.e. $F = 1$ and $F_1 = 1$ in both the design and evaluation sections of the solution process, is included only for reference as it neither physically represents an infinitely-bladed nor a three-bladed rotor).

Compared to the porous jump solution (and AD solution with no tip correction), the Glauert tip correction moves the optimum C_P to a higher C_{TL}, which is unsurprising as C_{TL}^{target} also becomes a smaller fraction of the nominal C_{TL}, while the limit of power extraction is closely related to the overall momentum balance. In the plot of C_P, the distance between the porous jump and blade-element AD results is interpreted as the losses due to wake rotation and viscous drag, as well tip losses due to the finite number of blades, similarly to the explanations of Figure 4.2.

Figure 4.5 shows the resulting rotor designs corresponding to $C_{TL} = 2.0$ in Figure 4.4. For ease of comparison, the Glauert and Shen designs at $C_{TL} = 2.0$ are plotted, despite $C_{P\max}$ being achieved at $C_{TL} = 2.2$. The solidity, σ, and twist, β, defining the rotor geometry are plotted across the span. For clarity, $\sigma = Zc/2\pi r$ is also plotted as the dimensionless chord length, c/R, with the length centred at zero on the vertical axis. (Arguably, if this was intended to show the planform of the blade, the chord length might be centred at its centre of aerodynamic moment, typically close to $c/4$). For comparison, the chord and twist distribution calculated by the lifting line method are shown in black. This is the from the same dataset as the $Z = 3$ case in Figure 4.3.

Comparison of the lifting line design with the unblocked CFD AD design may be discussed in relation to three areas: Close to the hub, close to the tip, and generally along the main length of the blade, i.e. $0.2 < r/R < 0.75$. As mentioned in the previous section, the LL implementation uses an image vortex system to model the presence of the hub as a wall extending in the axial direction, while the AD simulations simply use an impermeable disk to divert the flow. In Section 4.2.1, the author argued that flow details at the hub are both less important in terms of their contribution to overall power and thrust, and also likely strongly dependent on the particular geometry and therefore not well suited to reduced order modelling techniques like the AD. Therefore, the deviations at the hub are not discussed further.

Over a wide range of radial stations, e.g. $0.2 < r/R < 0.75$, there is good qualitative agreement between the LL design and the AD designs. The AD designs include the now familiar presentation of 'no' tip correction (for reference only), and the Glauert and Shen corrections, which only begin to significantly affect the design outboard of $r/R \approx 0.75$. However, along this intermediate region, the AD method results in a fairly uniform $5-10\%$ greater solidity than the LL design, while the twist is typically greater, but by less than 2%.

Outboard of $r/R \approx 0.75$, the solidity of the Glauert design is slightly lower than the LL solidity which is a direct consequence of a slightly too rapidly decreasing C_{TL} profile as $r/R \to 1$ in Figure 4.3. Because the Shen factor reduces the thrust imposed in the evaluation loop of the simulation, the solidity 'recovers' back towards the LL solution again. In both cases, the twist at the final few radial stations is reduced slightly (twist towards rotorplane) compared to the LL design in order to achieve $\alpha^{\text{target}} = 6$ deg at the corresponding flow angle, ϕ (cf. Figure 4.6).

While the lifting line naturally unloads the blade towards the tip as indicated by tapering the chord length towards zero, the uncorrected CFD AD method predicts a considerable finite chord length at the last radial station. The Glauert and Shen factors force a similar unloading in the CFD AD method via a reduction in solidity because of the definition of C_{TL}^{target} in Eq. 4.16, (cf. Eq. 4.14). Subplots in each main plot of Figure 4.5 show an enlarged view of the data at radial stations $0.9 \leq r/R \leq 1.0$. This may be the region where the most striking differences occur, particularly at the last two radial stations, but unfortunately, it is also the region where the least physical insight can be gained, because, following the discussion in Section 4.2.1, the results depend strongly on the interaction of numerous semi-empirical models. Due to Shen's F_1 factor in the evaluation loop, it is also clear that the rotor design outboard of $r/R \approx 0.9$ has a rapidly diminishing impact on the rotor performance, according to the AD model (cf. plot of $F_1(r/R)$ in Figure 4.6).

Compared to the LL solution, the AD cases impose a higher thrust on the flow (higher C_T), which results in a reduction of the annulus-averaged and blade axial induction factor inboard of $r/R \approx 0.8$, while the opposite is true for the outboard sections. It is notable that while the LL method predicted marginally lower thrust coefficients than the theoretical result for an unblocked rotor of $C_T = 8/9$, the AD method predicts values in excess of this inboard of $r/R \approx 0.8$, dropping rapidly further outboard. This is a timely reminder that the momentum theory results are a 1D approximation, which at best, may correspond to the mean values across the AD. The same observation can be made with respect to the distribution of the power

coefficient. (The reader is reminded that the plotted annulus-averaged C_P must be weighted by r to find the integrated total C_P). The greater predicted power inboard of $r/R \approx 0.8$ corresponds to the increase in rotational induction, and vice versa at the outboard stations. This is a direct consequence of conservation of angular momentum by Equation 3.33.

4.3.1.1 Tip constraint for twist

Because there are two design variables, solidity (σ) and twist (β), but only one target function, C_{TL}, the design process requires an additional constraint. In the simplest case, as discussed above, β is adjusted so that $\alpha = \alpha_{LD}$, to minimise loss of torque due to drag. The rotor naturally unloads towards the tips and this is accounted for by numerous mechanisms in the model as discussed above, but it may also be argued that α_{target} should be relaxed to α_0 at $r/R = 1$, where α_0 is the zero lift angle. On the one hand, there is no requirement for $\alpha = \alpha_{LD}$ at the tip if the forces are constrained to zero by the Shen factor, on the other hand, at any section where the force generation is non-zero, $\alpha \neq \alpha_{LD}$ will result in reduced efficiency. One approach for constraining β is demonstrated in Figure 4.5. In Equation 4.15, $\alpha^{\text{target}} = \alpha_{LD}$ is replaced by

$$\alpha^{\text{target}} = \alpha_0 + F_1(\alpha_{LD} - \alpha_0) \tag{4.18}$$

Using Shen's F_1 factor, α^{target} remains equal to α_{LD} across most of the span but is then smoothly driven to the zero lift angle of attack at $r/R = 1$. (This can be verified in the plot of α in Figure 4.6). For the aerofoil dataset used, $\alpha_{LD} = 6$ deg and $\alpha_0 = -3.65$ deg. The effect of this constraint on the C_P is negligibly small ($< 0.1\%$), but consistent with the explanation above, it results in a reduction. (The effect on C_P is actually included in Figure 4.4 with the point labelled 'Shen, TC'). Figure 4.5 shows that the tip constraint results in a reversal of the trend of twist close to the tip, with the blade rapidly twisting into the wind in order to approach α_0. This is accompanied by an increase of solidity in order to meet C_{TL}^{target} at the last radial station. According to the current model, the effect of this additional constraint will always be negligible as the Shen correction means that the forces reduce to zero at the tips regardless of the taper or twist. In the absence of a better understanding of the flow physics at the tips, the author chooses not to add this further complication to the calculation of the tip geometry for the remainder of this study.

4.3.2 Closing remarks on designing for unblocked flow

Figure 4.3 showed that the LL model found the optimum design for a three-bladed rotor at $\lambda = 4.5$ had a local thrust coefficient C_{TL} around 5% lower than the momentum theory solution of 2 at the inboard radial stations, dropping to zero as $r/R \to 1$ in a similar fashion to the tip-loss function F. In fact, the profile $1.9 \cdot F^2$ closely matched the LL result for C_{TL}. In comparison, Figure 4.4, clearly shows that the AD design method finds an optimum C_P at a nominal $C_{TL} = 2.2$ for the Glauert and Shen models, respectively. (Clustering of simulations around $C_{TL} = 2$ ensure that this is the predicted trend). This difference in predicted thrust coefficient propagates through the rotor design and flow variables as discussed above, preventing perfect agreement of the two models.

A second interesting observation is made on the predicted axial induction factors. To remind the reader, the blade induction factor, a, is the natural variable of the LL method as its value is calculated due to the induction of the trailed helical vortices, the azimuthally averaged induction $\overline{a}$ in Figure 4.6 is calculated as $\overline{a} = Fa$. The reverse is true in the CFD AD method where the flow field solver naturally returns $\overline{a}$ and the blade induction is calculated as $a = \overline{a}/F$. The LL design solution for a is generally lower but within $1 - 5\%$ of $\frac{1}{3}$ for $r/R > 0.3$ (i.e. neglecting the hub region). In the analytical BEM method, setting $a = \frac{1}{3}$ in each annular streamtube is used to derive the familiar blade shape solution for an ideal Betz rotor. Despite the lower thrust coefficient at the tip, relative to the LL solution the CFD AD model returns a higher annulus-averaged axial induction factor, which when corrected to the blade induction factor using F results in a small deviation from $\frac{1}{3}$ outboard of $r/R \approx 0.75$. As discussed above, this propagates through the design process, by calculating a reduced blade flow angle, ϕ, leading to reduced blade twist β. Further research, e.g. using blade resolved CFD simulations, would be required to establish where the actual solution lies, for the moment it is simply highlighted as a key difference in the analytical and numerical implementation of the blade element theory.

4.3.3 Rotor performance

In this section, the CFD AD model is run as an evaluation tool only, as in Chapter 3, to compare the performance over tip-speed ratio of the optimum rotor geometry design presented in Section 4.3.1 with the geometry calculated by the lifting line tool.

The results are shown in Figure 4.7. The choice of the design tip-speed ratio of $\lambda = 4.5$ was discussed at the beginning of Section 4.3.1 (this tip-speed ratio is used

for all designs presented in this thesis). It may initially appear surprising that the maximum C_P of the rotor or $C_{P\max}$ (cf. Chapter 2) does not occur at $\lambda = 4.5$, in fact the CFD AD method predicts that the maximum C_P is achieved near $\lambda = 5.5$. However, this can be explained with the help of Figure 4.2. The lifting line solution for the optimal three-bladed rotor at $\lambda = 4.5$ has a power coefficient $C_P = 0.462$, while at $\lambda = 5.5$ (a different rotor design) it is $C_P = 0.475$, an increase of 2.6%. The rotor designed at $\lambda = 4.5$ can achieve a higher C_P at $\lambda = 5.5$ but this will of course be lower than the C_P of the rotor designed at that tip-speed ratio, otherwise the latter would not be the optimum rotor. This is permissible due to the positive gradient (at this range of tip-speed ratio) of the curve of optimum rotor designs in Figure 4.2. Physically, it is a result of the rotor imposing a greater thrust on the flow, which allows it to approach the infinitely bladed solution, before the additional drag causes C_P to fall again. The AD model predicts a slightly higher C_P for the LL rotor design than the value predicted by the LL method, $C_P = 0.483$ (+4.5% compared to LL evaluation), and $C_P = 0.501$ at $\lambda = 5.5$ or 3.54% greater than C_P at the design tip-speed ratio $\lambda = 4.5$. The difference between the LL and AD solutions is not unexpected and this constitutes good agreement given the range of approximations involved in both models. The Glauert rotor design is compared (plotted in green on Figure 4.5), rather than the Shen rotor design, but it is evaluated using both the Glauert and Shen tip treatments. Using either tip model for evaluation, the LL geometry outperforms the AD design at all tip-speed ratios plotted, although the agreement is within ca. 1.5%. This is very satisfactory considering the uncertainty surrounding the target local thrust distribution, Eq. 4.16.

Figure 4.8 shows the radial variables calculated by the AD evaluation. The differences in operation of the AD and LL rotors follow from the differences in their geometry, which have already been discussed. They will be very briefly recapped here, the author finds it helpful to refer to Figure 3.1 when considering the effect of induction factors on flow angles. The solid green line is the same dataset as the solid green line in Figure 4.6 (which is obscured by the almost identical Shen design), as the evaluation is carried out as part of the design process. By comparison, the LL rotor, in the AD evaluation tool, imparts a lower thrust inboard of $r/R \approx 0.8$, leading to a lower axial induction factor, slightly higher flow angle and angle of attack, while the opposite is true at the outboard stations. This means that the LL rotor is operating at a slightly non-optimal angle of attack, $\alpha > \alpha_{LD}$, at many inboard stations. However, it still achieves a greater total power due to a higher C_P at radial stations outboard of $r/R \approx 0.9$. This does not indicate that the CFD AD method is generally

limited to designing sub-optimum rotors, rather it corresponds to the accuracy of C_{TL}^{target}.

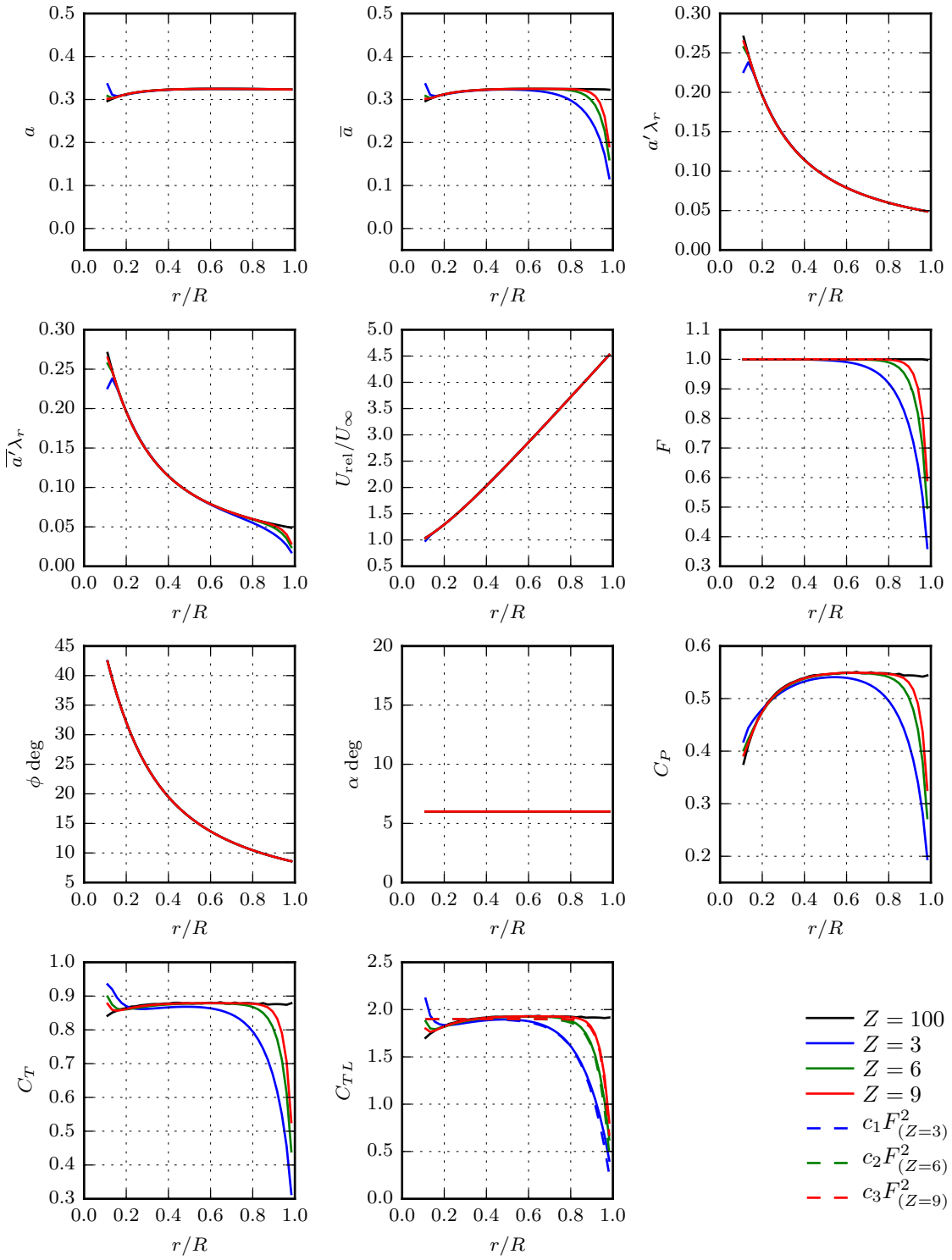


Figure 4.3: Radial variables corresponding to BEM AD model extracted from lifting line solutions for $Z = 3, 6, 9$ and $Z = 100$ (quasi-infinite) blades, $C_L/C_D = 90$.

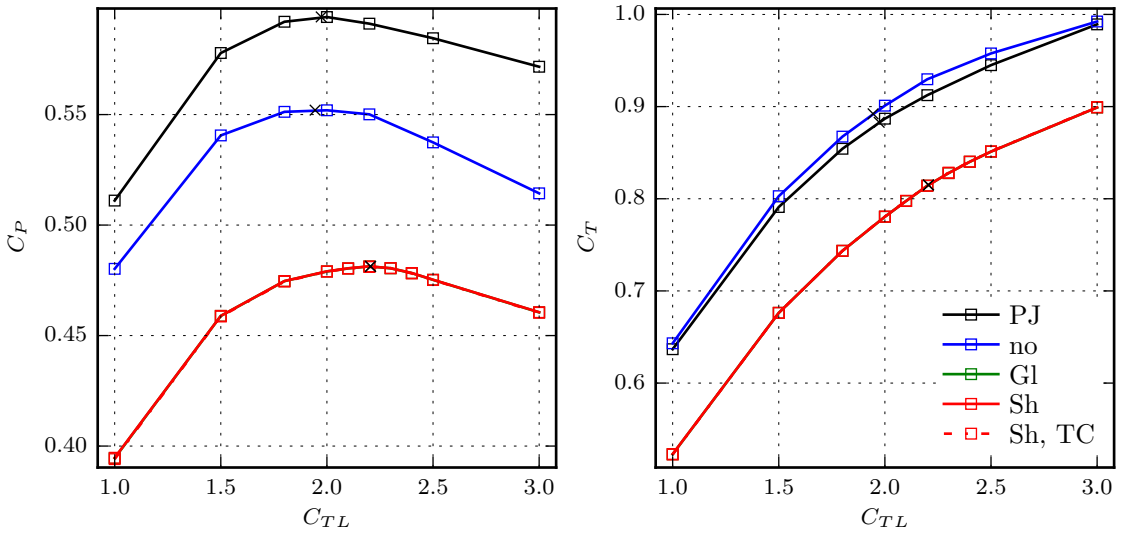


Figure 4.4: C_P and C_T of rotor designs at different target C_{TL} (each point corresponds to a unique rotor design). Black crosses indicate the location of the optimum design (maximum C_P). The three tip models (no, Glauert and Shen) are demonstrated, and the simple AD (or 'porous jump') solution is shown for comparison. Note that the Glauert and Shen corrections produce almost identical solutions.

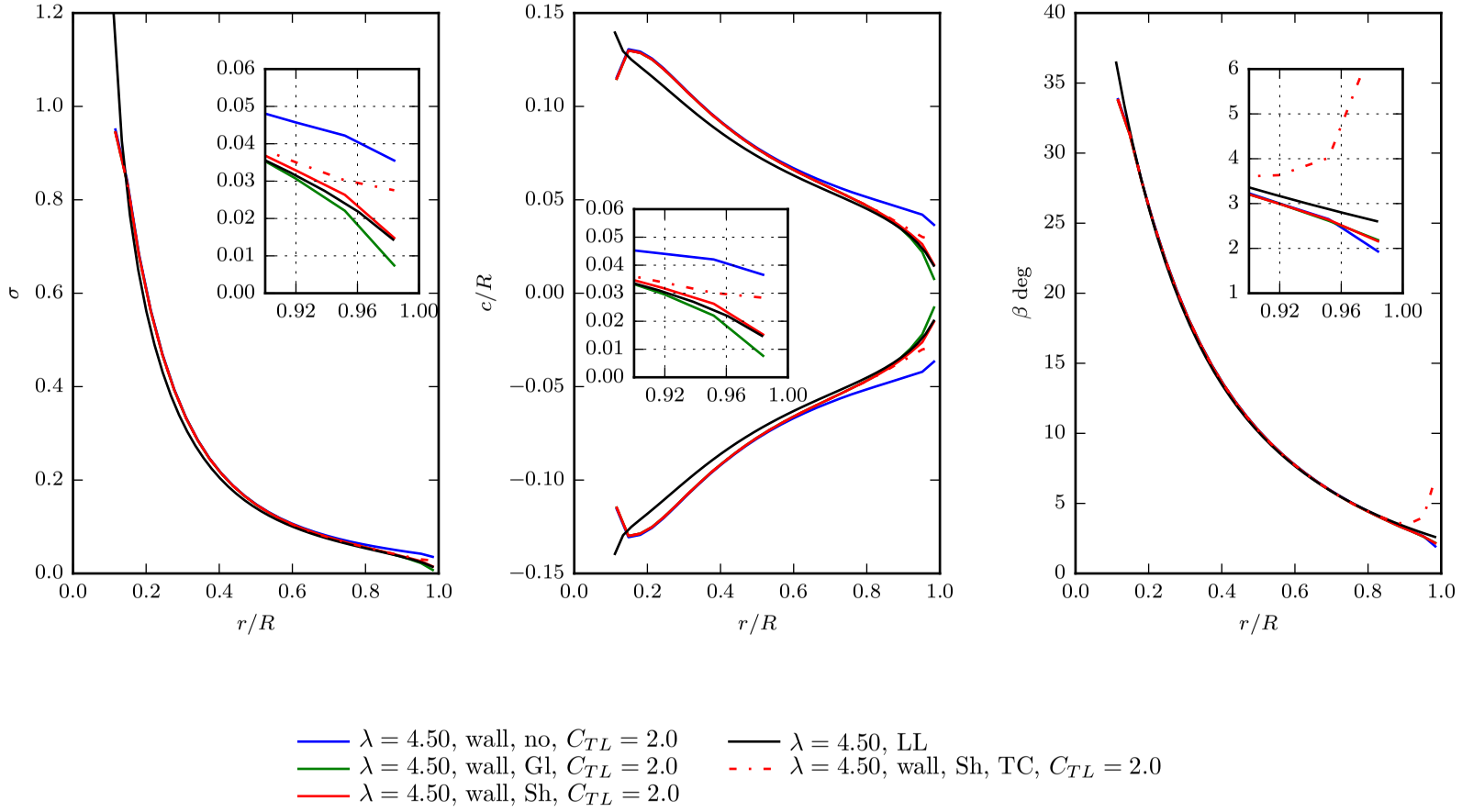


Figure 4.5: Designed rotor geometries: The AD method is applied with no, Glauert and Shen tip corrections; for the AD method the hub is modelled as an impermeable wall, and 'TC' indicates the use of a tip constraint on β. The zoomed subplots show only $r/R \geq 0.9$. The LL design is shown for comparison.

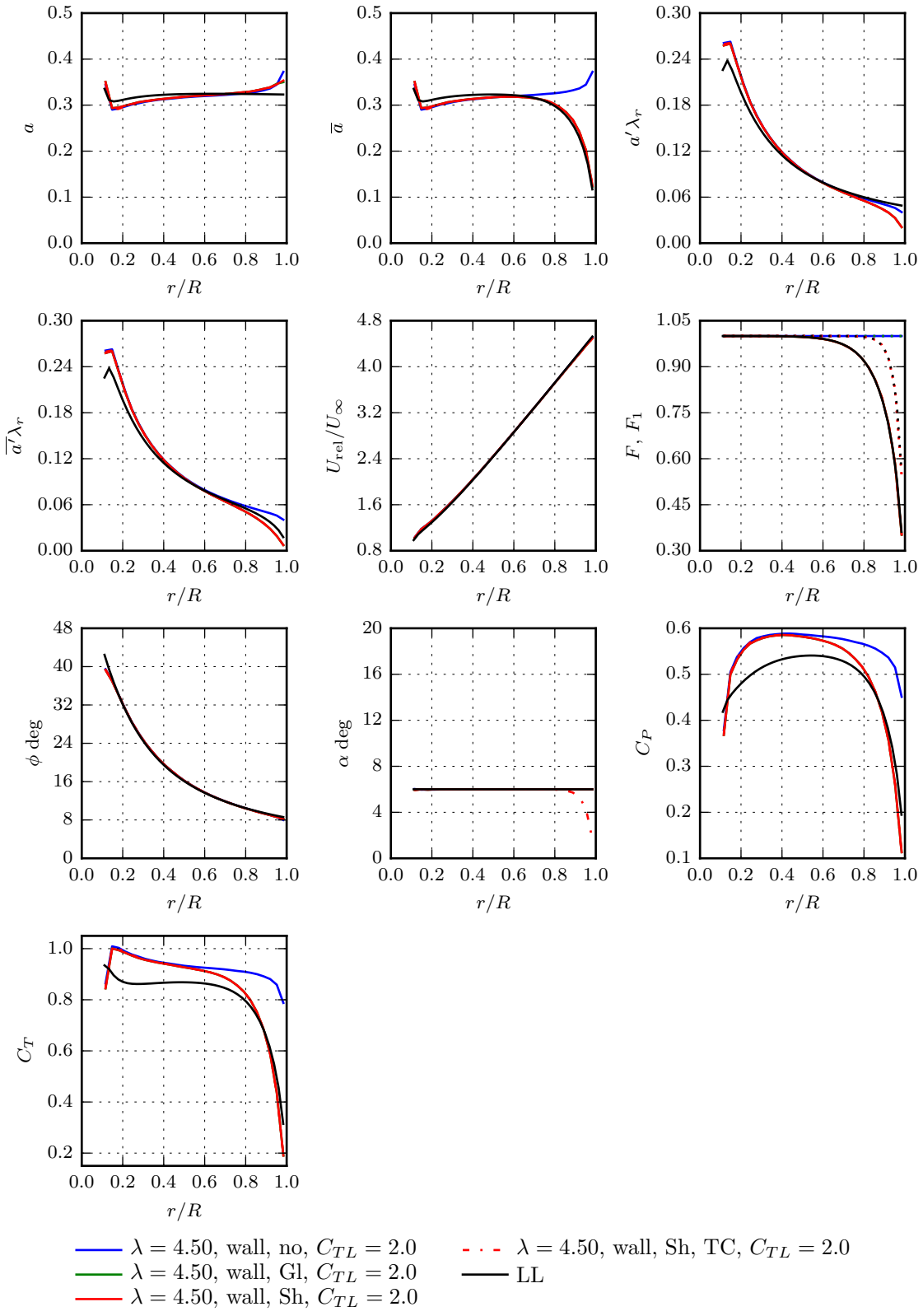


Figure 4.6: Radial AD variables corresponding to designed rotor geometries of Figure 4.5, LL data corresponds to $Z = 3$ design in Figure 4.2.

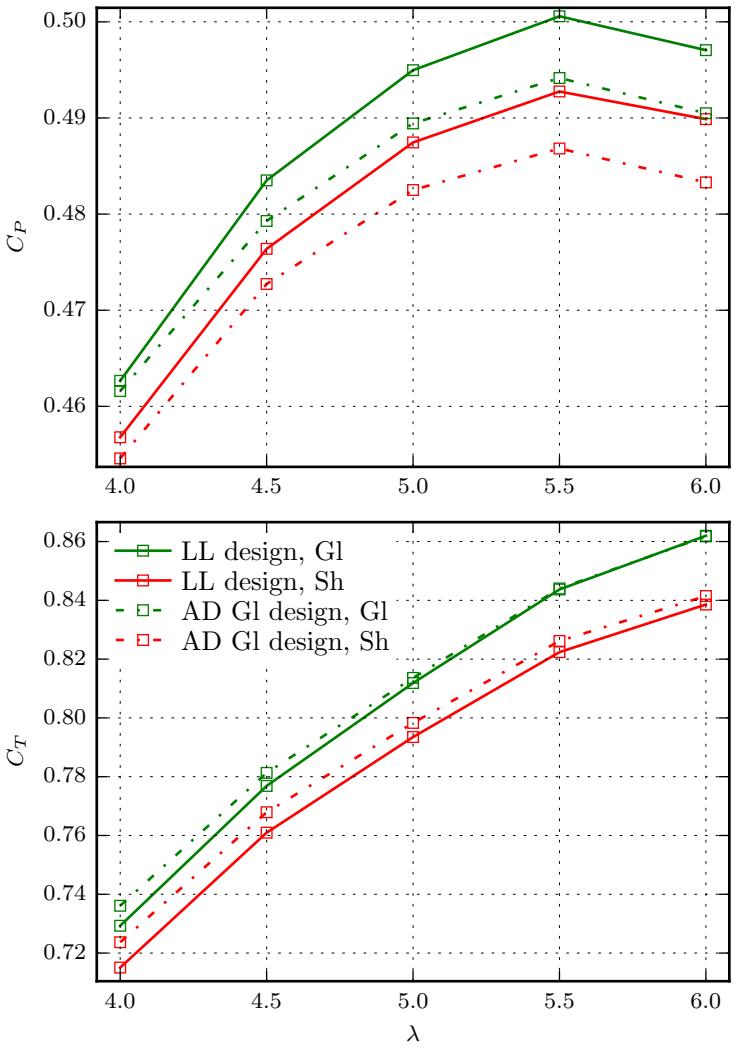


Figure 4.7: C_P and C_T, comparing AD Glauert rotor design at $C_{TL} = 2.0$ to the LL design at $\lambda = 4.5$, evaluated in the AD framework with each of the Glauert and Shen tip treatments.

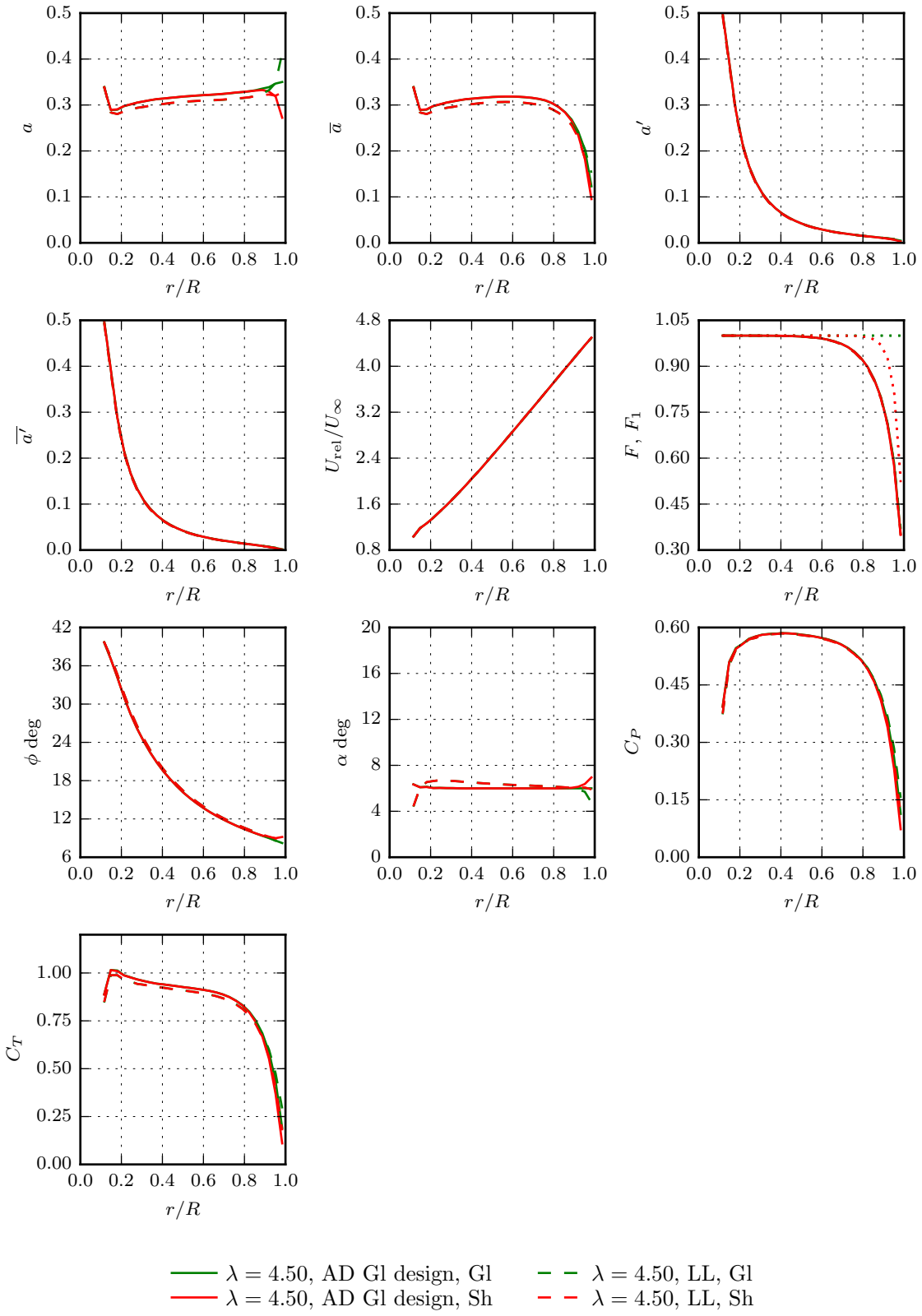


Figure 4.8: Radial blade element variables, comparing AD Glauert rotor design at $C_{TL} = 2.0$ to the LL design at design tip-speed ratio $\lambda = 4.5$.

Chapter 5

Hydrodynamic design of tidal turbines for an array

5.1 Computational domain

In this chapter, the AD design method of the previous chapter, which can naturally account for flow blockage and freestream turbulence via the computational domain and the RANS solution, is used to design turbines to operate in an array. The array channel dimensions and flow conditions are chosen to allow comparison with the results of Chapter 2 where simple actuator disks without blade element theory were used. Turbines are located on the yz-plane at $x = 0$ in a channel of depth $2D$ and width $10nD$, where n is the number of turbines. In order to achieve realistic Reynolds numbers on the scale of the turbine, the turbine diameter is $D = 20$m, operating in a channel with uniform inlet velocity of $U_\infty = 2$m/s and the fluid properties are of water. In Chapter 2, the length of the computational domain upstream and downstream of the actuator disks was deliberately large in order to observe array scale wake recovery even for wider arrays, e.g. 8 disks. For the purpose of designing a single or even two turbines, a domain of $-10 \leq x/D \leq 20$ is sufficient to produce results which are independent of the location of the boundaries in the axial direction. This has been found by the current author in previous, unpublished work and by others performing similar computations, e.g.[50][61].

The rotor designs presented in the previous chapter for unblocked flow with negligible freestream turbulence used an impermeable disk of diameter $D/10$ to model the hub. In this chapter, the hub diameter is increased to $0.15D$ and the nacelle was included as a solid boundary generated by rotation of a 2:1 aspect ratio semiellipse at the upstream and downstream end, a cylindrical mid-section and overall length of $3/5D$. The geometry was simply intended to be a streamlined forebody without

blunt edges. The dimensions were chosen to approximate those found in images of numerous full-scale prototype devices [21], with the assumption that these are the minimum structural and/or space requirements to house the gearbox and power generation equipment. The nacelle geometry can be seen in Figure 5.4. While unstructured tetrahedral meshes were marginally inferior to structured hexahedral meshes in predicting wake profiles downstream of actuator disks, Figure 3.14 in Chapter 3 showed that the solutions at the disk plane were negligibly different at sufficient resolution (medium or fine). To conveniently include the nacelle boundary and to allow a homogeneous meshing strategy for different sized domains, the grids in this chapter are all tetrahedral grids, with resolution between the medium and fine case of Chapter 2.

The Chapter begins by isolating the effect of freestream turbulence on the design of a single rotor in the channel aspect ratio defined above. In the second section, an array of rotors is designed in situ in a four turbine array (non-homogeneous flow conditions across the array). These designs are compared with independently designed rotors.

5.2 Designing for turbulence

5.2.1 Simulation details

A single disk was centred on the on the yz-plane at $x = 0$ in a channel of depth $2D$ and width $10D$. The design process was repeated for two freestream turbulence intensity levels, the inlet values were adjusted accordingly to result in $TI \approx 0\%$ and $TI \approx 10\%$ at $D/2..D$ upstream of the AD before velocity gradients cause an increase. As in the previous chapter, the optimum design was sought by running simulations for a range of nominal C_{TL} as defined in Eq. 4.16. As well as the three tip treatment options: 'no' tip correction, Glauert and Shen, simulations were run using the simple porous disk of Chapter 2 and uniform local thrust coefficient ($C_{TL} = K$ from Chapter 2).

5.2.2 Simulation results

The power and thrust coefficients are plotted in Figure 5.1 where the maximum C_P has also been estimated by finding the maximum of a cubic spline interpolation of the simulation points. The solid and dashed lines show the cases run with negligible ($TI \approx 0\%$) and high freestream turbulence ($TI \approx 10\%$), labelled 'LoFreestream Turbulence (FST)' and 'HiFST' respectively. In terms of the effect of freestream turbulence, the

results agree with previous investigations using simple actuator disks, e.g. by Nishino & Willden [50]: With increasing freestream turbulence, $C_{P\max}$ increases and occurs at a higher local thrust coefficient. This was explained in Chapter 2 as a consequence of increased turbulence enabling increased momentum transfer between the faster bypass flow and the slower core flow through the turbine. The rotor designs approximately corresponding to $C_{P\max}$, i.e. at nominal design $C_{TL} = 2.5$ and $C_{TL} = 3.0$ for the low and high freestream turbulence cases, respectively, are plotted in Figure 5.2 while Figure 5.3 shows the radial profile of the blade element variables at the design C_{TL}.

Comparing the effect of the Glauert and Shen model at any particular design C_{TL} and freestream turbulence level, the Shen model results in an increase of solidity with increasing r/R outboard of $r/R \approx 0.7$. This occurs because the target C_{TL} is almost unchanged while the Shen correction in the evaluation part of the calculation directly reduces the effectiveness of any given blade geometry close to the tips. There is a negligible effect on C_P according to Figure 5.1. While the validation study in Chapter 3 found that the Shen correction did improve overall agreement of the numerical and experimental results, it is important to recall that the correction model was developed with a view to improving agreement when evaluating this particular experimental rotor [62]. The author notes that the NREL Phase VI [32] rotor was a two-bladed rotor with a linear taper from $c/R = 0.147$ at $r/R = .25$ to a substantial chord of $c/R = 0.0707$ at $r/R = 1$. The second experiment used to calibrate the Shen model similarly was a two-bladed rotor with linear taper from $c/R = 0.117$ at $r/R = .252$ to $c/R = 0.0467$ at $r/R = 1$. Thus neither rotor had a rounded tip such as predicted by the LL design tool, or the AD design tool using the Glauert tip model and C_{TL}^{target} from Eq. 4.16. It seems unlikely that such a simple model as the Shen tip correction could be sufficiently general to be accurate for all blade geometries. Furthermore the model was developed for evaluation, not design, and it is because the Shen model restricts the impact of the computed load that seemingly improbable blade sections are allowed to develop towards the tip as their impact is limited due to the rapid fall-off of F_1 as $r/R \to 1$. The increase of solidity when using the Shen model, compared to the Glauert model, was already observed when designing for unblocked conditions in Figure 4.5 but the effect was less severe. In light of the variable effect on the design in the tip region and the concerns discussed above regarding the generality of the model, the Glauert design will be used in performance comparisons presented in this chapter.

Comparing the Glauert rotor design at the same $C_{TL} = 2.5$ but at low and high freestream turbulence in Figure 5.2 shows a small uniform increase in solidity and

twist (tendency to reduce the angle of attack) across most radial stations. The solidity increase corresponds to an increase of C_T in Figure 5.3, while the increased twist is a response to the increased flow angle, which in turn is a result of turbulent mixing acting to increase the mass flow through the rotor (i.e. reduce the axial induction factor). If necessary, the author recommends referring to Figure 3.1 to verify the relationship of induction factors, flow angles and force vectors. Achieving the optimum design for high freestream turbulence, i.e. the Glauert design at $C_{TL} \approx 3.0$ (cf. Figure 5.1), requires a larger increase in blade solidity to provide the required thrust. This results in a relative increase in axial induction, which following similar arguments to those above, results in a small reduction in blade twist.

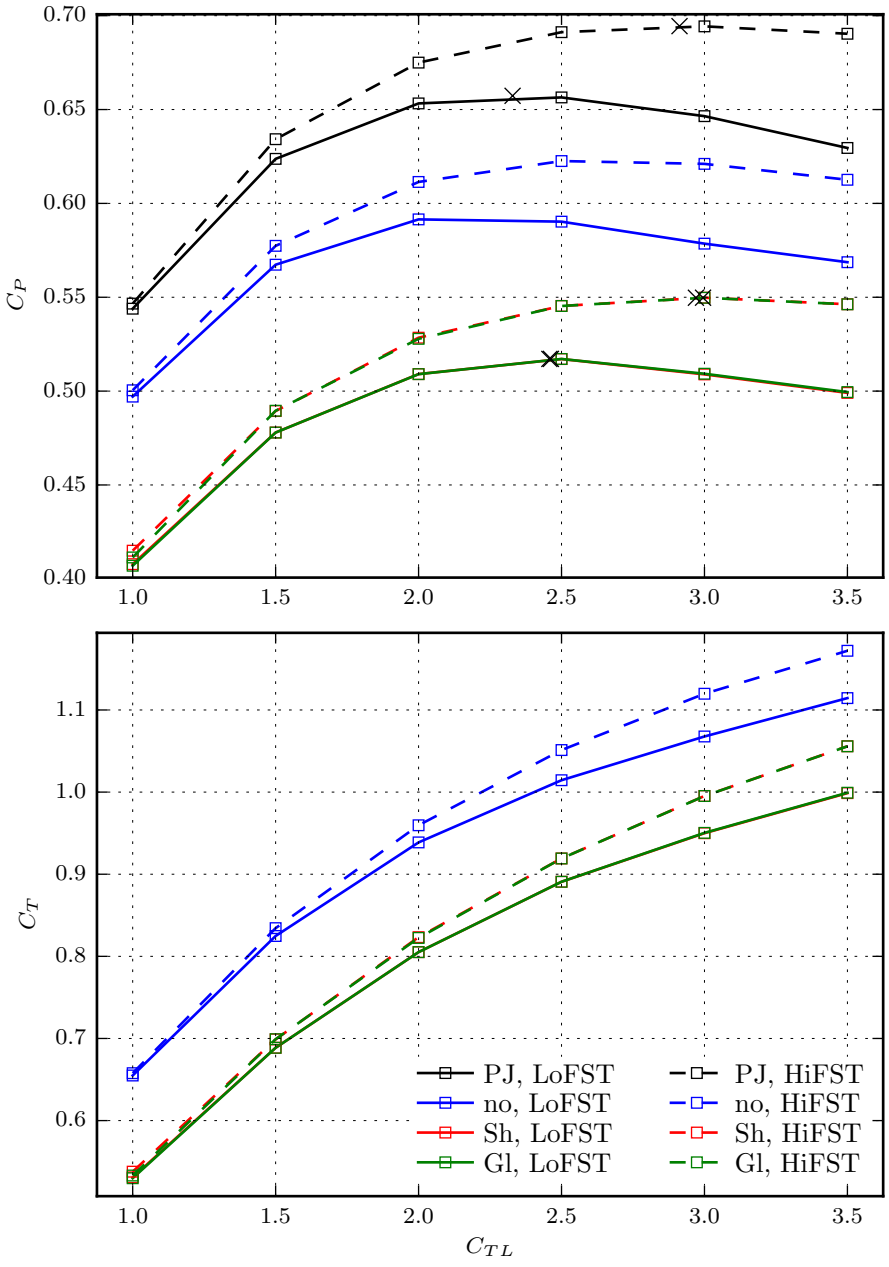


Figure 5.1: C_P and C_T of rotor designs at different target C_{TL} (each point corresponds to a unique rotor design). C_{TL} is the nominal target local thrust coefficient defined in Eq. 4.16. Black crosses indicate the location of the optimum design (maximum C_P). The three tip models (no, Glauert and Shen) are demonstrated, and the simple porous jump solution is shown for comparison. 'Lo' and 'Hi' indicate the two levels of freestream turbulence.

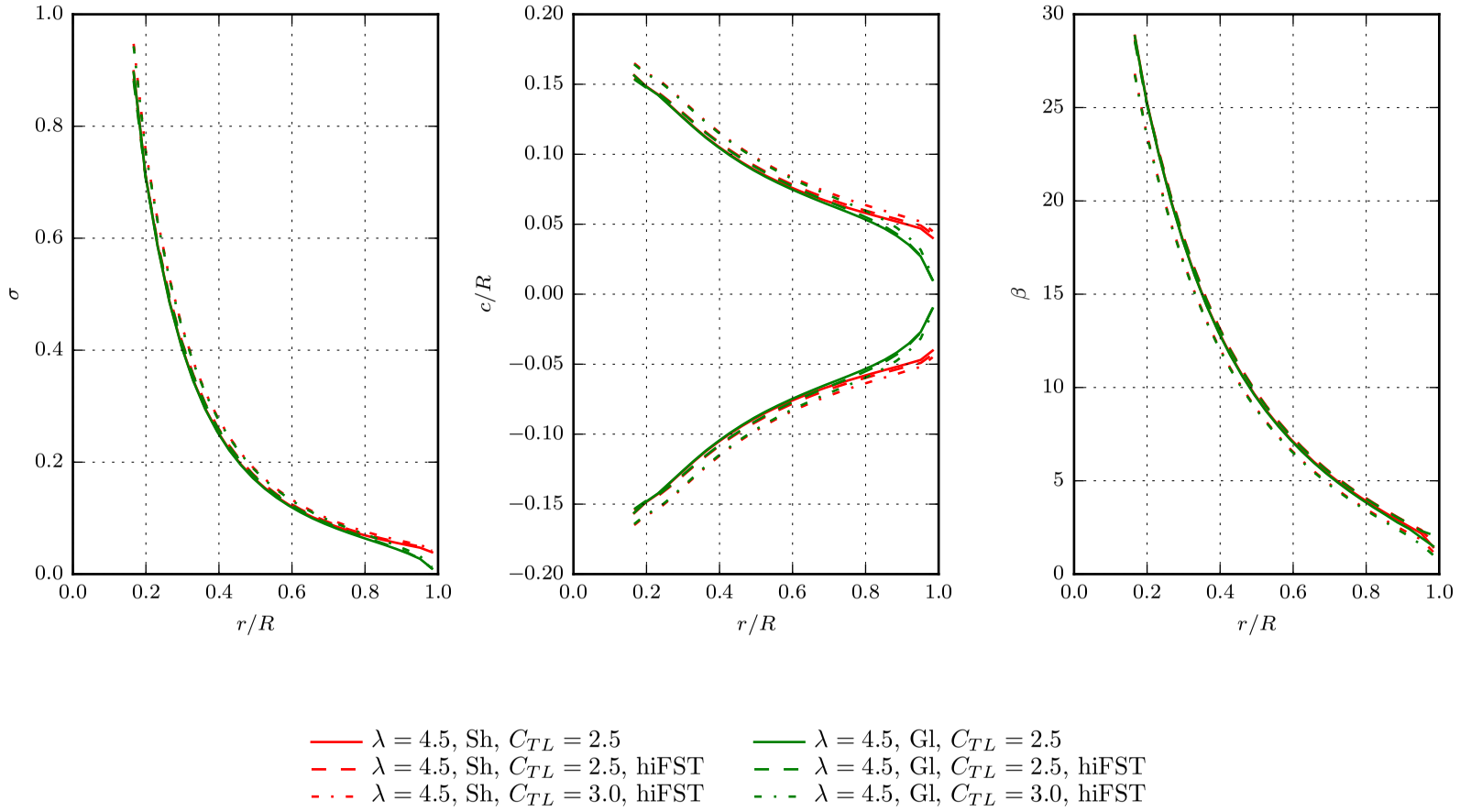


Figure 5.2: Designed rotor geometries in a channel of width $W = 10D$ and $H = 2D$, and high and low freestream turbulence.

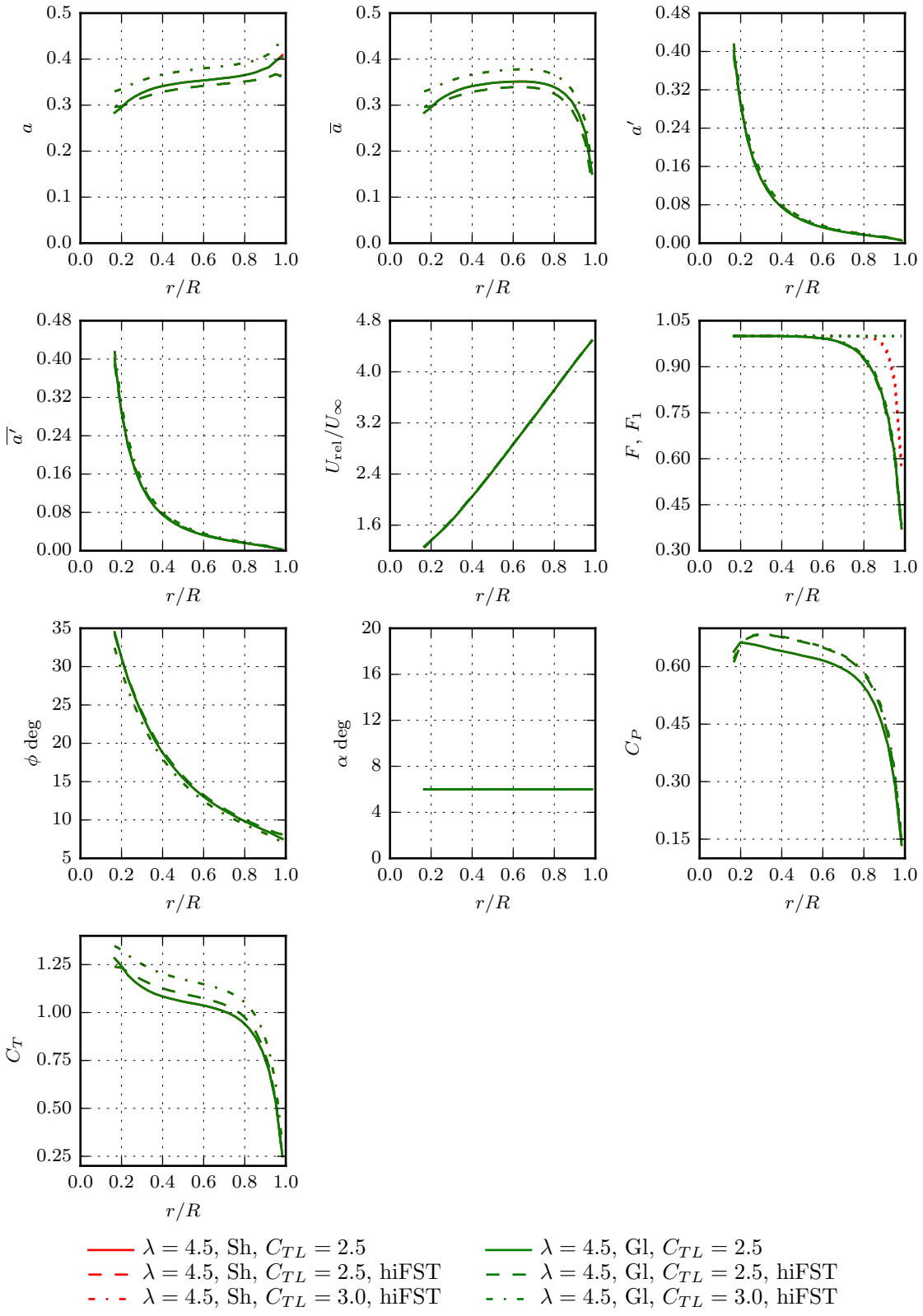


Figure 5.3: Radial outputs from BEM design of low and high freestream turbulence designed rotors using Glauert and Shen Tip corrections. The Shen and Glauert solutions are very close and obscure each other.

5.3 In situ array rotor design

Using simple actuator disks, Chapter 2 showed that C_T varies across a closely spaced array, being greater at the inboard rotors and lower at the outboard rotors of the array (cf. Figure 2.4). It is therefore clear that the optimum rotor design must vary across the array. The CFD AD boundary condition has been implemented in such a way that multiple rotor designs can be carried out simultaneously in the computational domain. This section seeks to demonstrate the effect of designing specifically for an array and concludes with a comparison of array performance using in situ designed rotors versus alternative rotors designed in isolation, such as that designed in Section 5.2.

Inlet conditions to the channel are now controlled to result in freestream turbulence just upstream of the AD of $TI \approx 5\%$, which is midway between the two cases shown in Section 5.2 and close to the value used in the array simulations of Chapter 2.

5.3.1 The computational domains

While an array of four turbines centred on the yz-plane leads to a symmetric problem with respect to the $y = 0$ and $z = 0$ planes using the simple actuator disk in Chapter 2, the blade element AD developed from Chapter 3 onwards does not permit any symmetry plane intersecting the disk because of the rotational wake. However, the array of four turbines can be calculated as two pairs of turbines using a symmetry plane at $z = 0$, with the non-critical restriction of symmetric rotation directions about $z = 0$.

As an alternative to in situ, simultaneous design, three rotors are designed in isolation to be tested in the array for comparison. The first is in an effectively unblocked domain ($B = 0.005$), which will produce a similar rotor to the LL method, or indeed the analytical BEM method. The second is in a domain with square cross-section but the same blockage as the rectangular channel containing the array of four turbines, i.e. with side of length $L = \sqrt{W \cdot H}$, where the channel domain for one disk has width $W = 10D$ and height $H = 2D$. The final design is performed in a domain with the local blockage provided by the array, (borrowing a concept from the analytical model of Nishino & Willden [51]), i.e. $D + s$ wide, where s is the tip-to-tip gap between rotors, and the channel height of $2D$. In this last case periodic boundary conditions are used in the cross-stream direction so that this effectively corresponds to an infinitely wide array. The three domains will be indicated by the labels ‘unblocked’, ‘square’ and ‘local’ respectively in the presentation of the results.

Conceptually, it seems that the actual effective blockage felt by the turbines in the array should lie between these latter two cases.

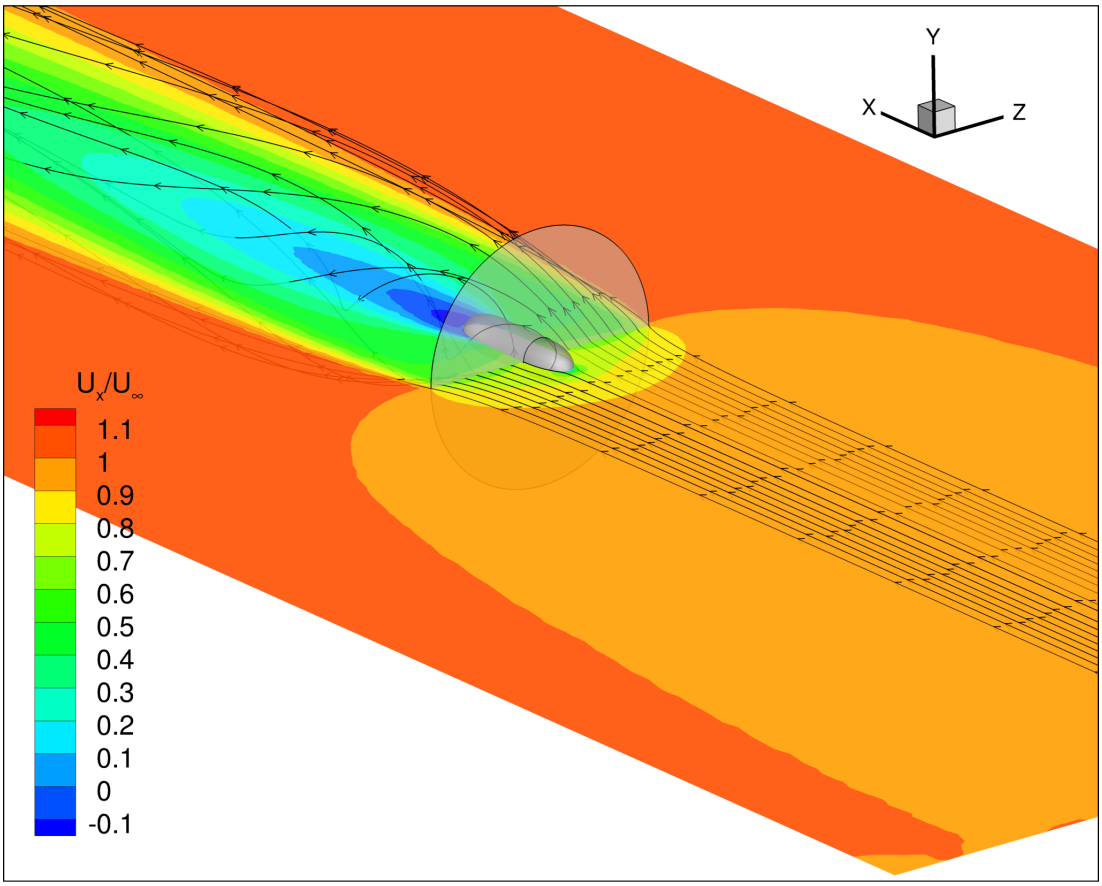


Figure 5.4: Velocity contours and streamlines from the $C_{TL} = 2.5$ design in the square domain.

5.3.2 Simulation results

Figure 5.4 shows contour plots of normalised streamwise velocity on a horizontal plane through the centre of the AD, as well as streamlines passing a uniformly spaced rake of 20 points across the width of the AD. The velocity contours show flow features such as the development of a shear layer downstream of the edge of the AD, the wake with recirculation behind the nacelle, and the flow retardation upstream of the nacelle and AD which causes diversion of flow into the bypass. The streamlines show the effect of conservation of angular momentum as enforced by Eq. 3.34. (The rotor is rotating in a positive sense about the x-axis, causing the wake to rotate in the opposite direction.

Figure 5.5 shows the search for C_{TL} producing the rotor design with the highest C_P in each domain. This is the same process as was used in Section 4.3.1. Each simulation

point, indicated by a square marker, corresponds to a different rotor design. Larger steps in C_{TL} are used initially, and then further simulations are added around the optimum design. The black crosses indicate the estimated maximum by using a cubic spline interpolation of the simulation results. In the 'unblocked' or lowest blockage domain, the rotor design is optimised for a nominal $C_{TL} = 2.30$, slightly higher than was found for in Chapter 4 (by comparison, the current case has a higher freestream turbulence but also a greater hub radius and realistic nacelle geometry), achieving $C_P = 0.497$. The next highest $C_P = 0.519$ at $C_{TL} = 2.43$ is achieved by the rotor in the 'square' domain with blockage equal to the channel.

The points labelled 'array' are the rotors designed simultaneously at their position in the four-turbine array. As in Chapter 2, considering the symmetry about the $z = 0$ plane, the inboard disk is labelled 'd1' and the outboard disk 'd2'. As expected from the results of Chapter 2, the inboard rotor achieves a higher optimal $C_P = 0.589$ at $C_{TL} = 3.20$ than the outboard rotor, $C_P = 0.575$ at $C_{TL} = 2.87$. In other words, the inboard rotor produces about 2.4% more power than the outboard rotor (cf. increase of 2.6% in Figure 2.4). The very high C_P of the 'local' array blockage domain indicates that a four turbine array is much too short to behave like a quasi-infinitely wide array, this case will not be discussed further.

As has been found in Section 5.2, activating the Shen model during rotor design has a negligible effect on the C_P of the rotor, but can lead to an increase in solidity near the tips compared to the Glauert model, cf. Figures 5.5 and 5.6. Intuitively, this does not seem like the right solution for an optimum rotor, but rather an artefact of the tip correction model being used outside of the conditions it was calibrated for. As a result, only the Glauert design will be considered in the subsequent array performance comparisons.

The relevant differences between rotor designs in Figure 5.6 can again be explained by interpreting the force and flow field coupling with the help of Figure 5.7. The optimum design points for disk 1 and 2 designed in situ in the array occur at higher C_{TL}, which requires a higher blade solidity, resulting in a greater axial induction, lower flow angle and hence lower blade twist than either of the rotors designed in isolation. It is instructive to note that the array designed rotors, for which the local blockage is greater, achieve peak power at increased induction, i.e. lower mass flow, relative to single isolated rotors in lower blockages; peak array rotor C_P occurs for $\overline{a} > \frac{1}{3}$ which concurs with the blockage analysis of Garrett & Cummins [27] and simulations of Nishino & Willden [50]. The inboard disk also has a 1-2% greater solidity than the outboard disk across the majority of the span (ignoring hub and tip effects) in

order to achieve the optimum thrust distribution across the array. Despite the higher thrust on the inboard rotor, the induction is slightly lower than at the outboard rotor as the array forces a greater mass flux through the inboard turbines. By comparison, the outboard rotors suffer a form of array-tip leakage resulting in reduced mass flux, i.e. higher induction, through them despite their relative reduced thrust compared to the inboard rotors. Again, these conclusions agree qualitatively with the results for simple actuator disks in Chapter 2. Compared with the sub-optimal rotors, the optimal array rotors produce significantly greater power at all radial stations.

5.3.3 Tuning the four turbine array

In Chapter 2, the maximum power from an array of four simple actuator disks was found when the inboard and outboard disks had the same local thrust coefficient. This results in a greater mass flow through the inboard disks accompanied by increased power and thrust at the inboard disks. The AD design implementation has been used to confirm that this trend is the same for physically more realistic blade element actuator disks. Figure 5.8 shows a range of design points where the nominal target C_{TL} is varied either evenly for both rotors (as has been done until now), but also at fixed ratios where either the inboard or outboard rotor has a 10% higher target C_{TL}, while the other has a 10% lower target C_{TL}. Recall that C_{TL} is the nominal value and the actual local target thrust coefficient always varies with $F^2(r)$ across each rotor. Cases where the inboard rotor is loaded with a higher C_{TL} are labelled 'centre' while 'edge' indicates multi-rotor design where the outboard rotor has the higher C_{TL}. It is observed that attempting to increase loading at the centre disks results in a more balanced distribution of thrust and power across the array than using a uniform target C_{TL}, while the opposite is true when attempting to increase the loading at the edge. However, the maximum mean array power is only achieved with a uniform target C_{TL}. As discussed in Chapter 2, the benefit of more uniform thrust across the array from a structural point of view may justify the very minor reduction in array power ($< 0.1\%$).

5.3.4 Closing comments on in situ tidal turbine design

Eq. 4.16 is a heuristic solution to the problem of constraining the loading of the AD rotor design problem to allow optimisation using a single variable, $C_{TL,\text{nom.}}$, which is necessary to limit the computational expense. It appears that this profile is quite accurate for the design of rotors in unblocked flow and with negligible freestream

turbulence. The same approach has been used in an extended model to allow in situ designing of multiple rotors in a closely spaced array, where global blockage and device interaction, as well as free stream turbulence have a considerable effect on the limit of power extraction. It is not yet known whether the profile of Eq. 4.16 will produce the optimum rotor designs for this situation but it is also clear however that designing for a uniform C_{TL} would ignore the results of lifting line theory for optimum rotors with a finite number of blades.

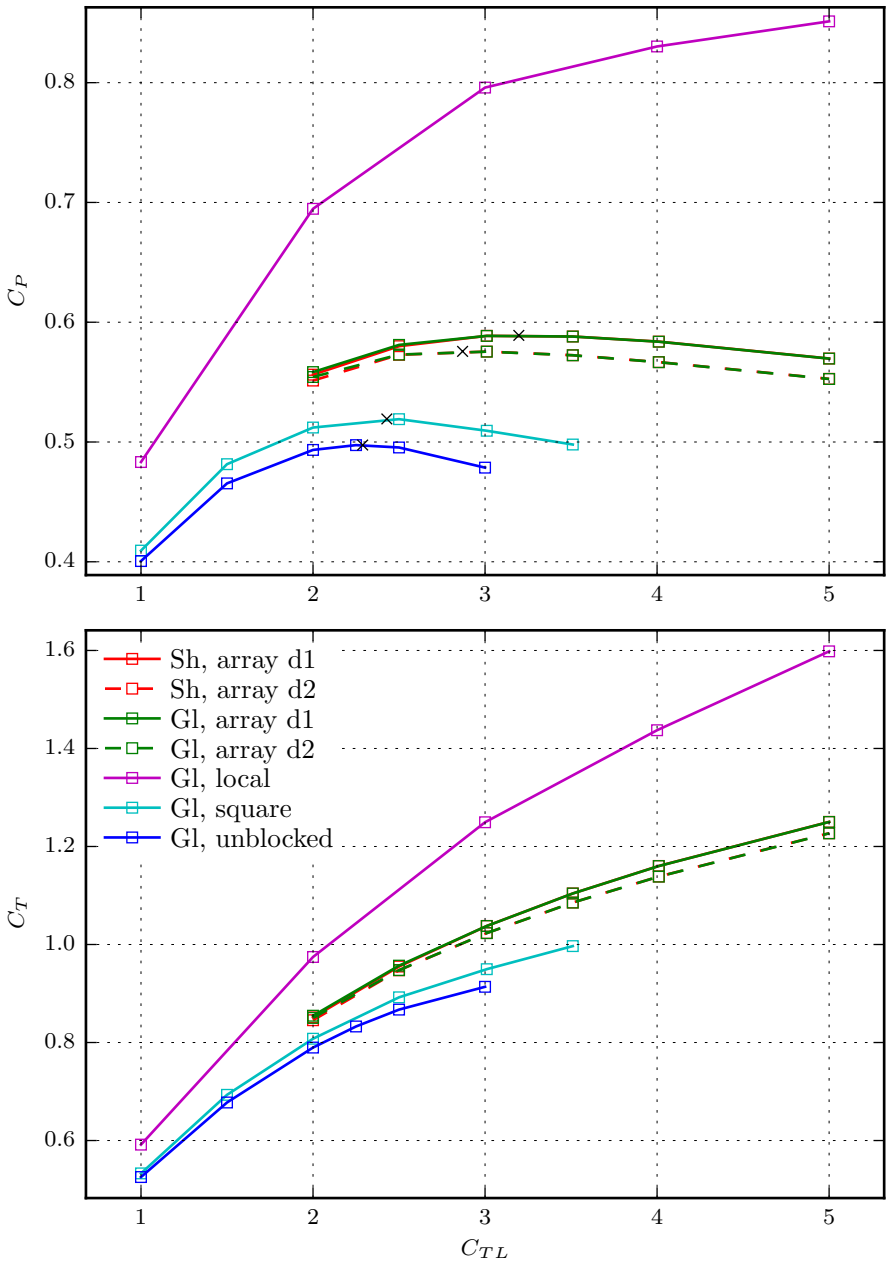


Figure 5.5: C_P, C_T in different domains: 4-disk array in a channel ($H/D = 2$, $W/D = 10nD$) using $z = 0$ symmetry plane (disk 1 at centre, disk 2 at edge), (single disks:) 'local' indicating a domain the size of the (high) local array blockage with periodic lateral boundaries, 'square' indicating a domain of square cross-section with the blockage of the channel, and (quasi-) unblocked. C_{TL} is the nominal target local thrust coefficient defined in Eq. 4.16.

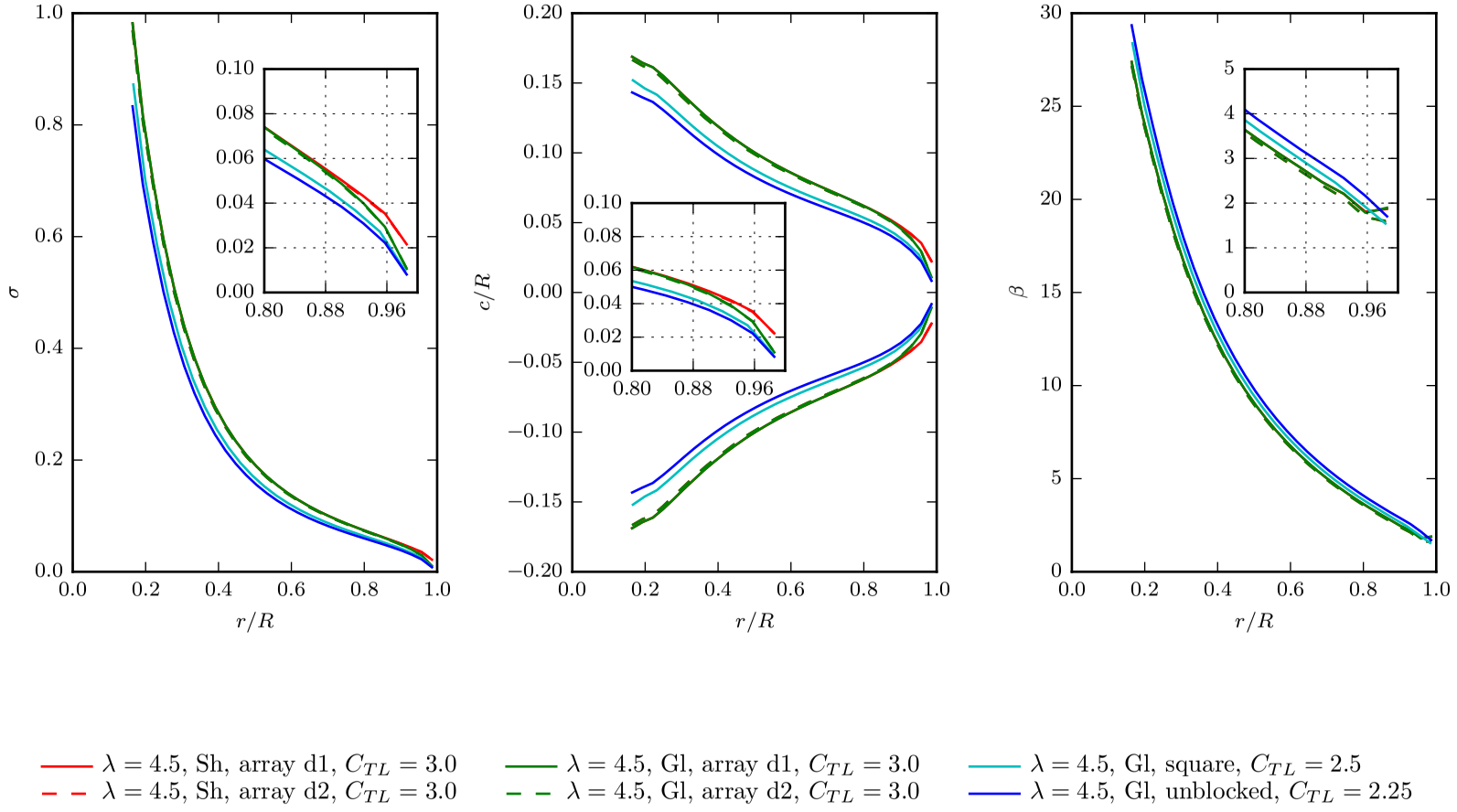


Figure 5.6: Designed rotor geometries corresponding to points at $C_{TL} = 3$ in Figure 5.5 for the channel, $C_{TL} = 2.5$ for the square domain with channel blockage, and $C_{TL} = 2.25$ for the (quasi-) unblocked domain.

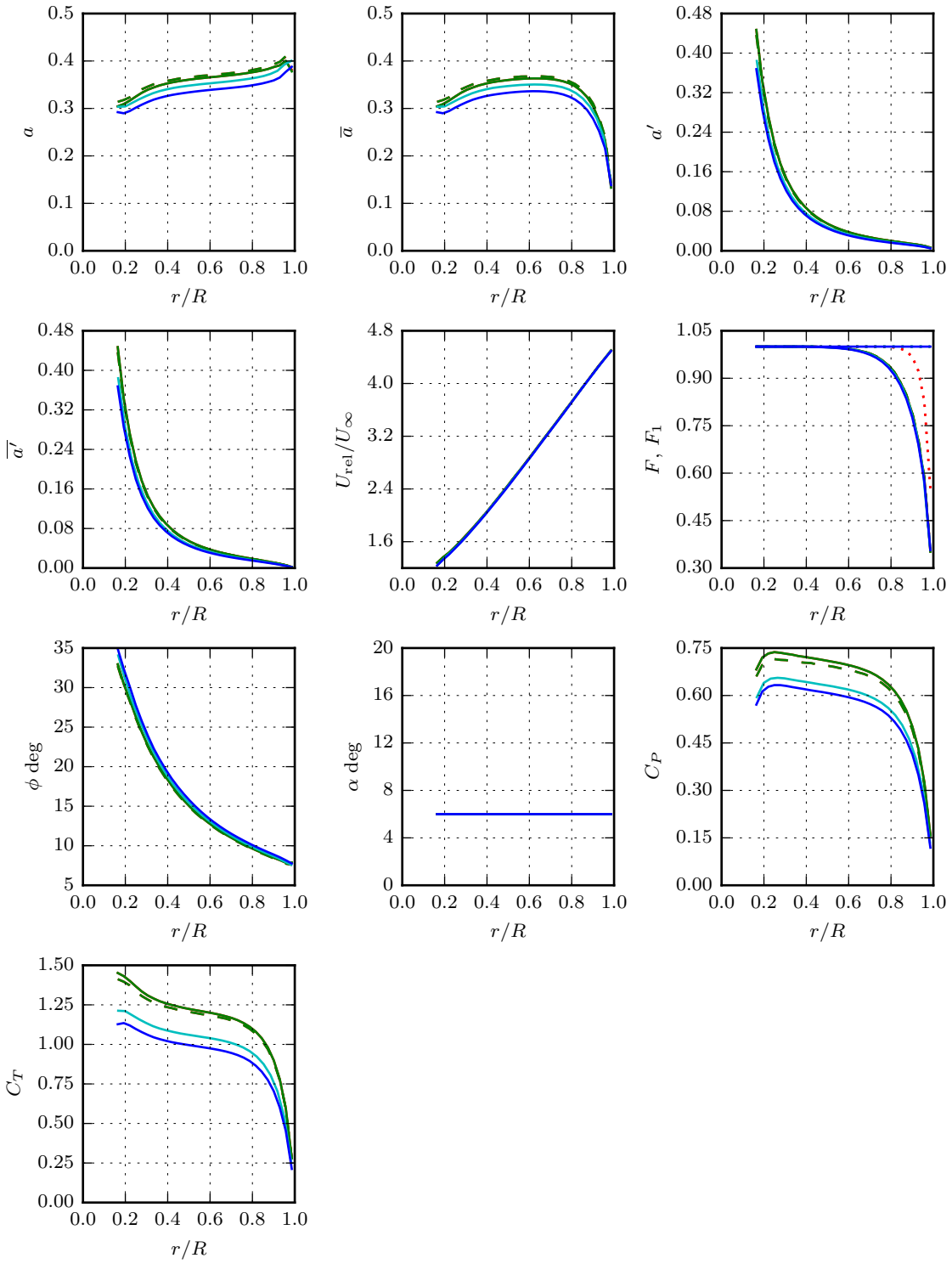


Figure 5.7: Radial AD variables for designed rotor geometries corresponding to Figure 5.6.

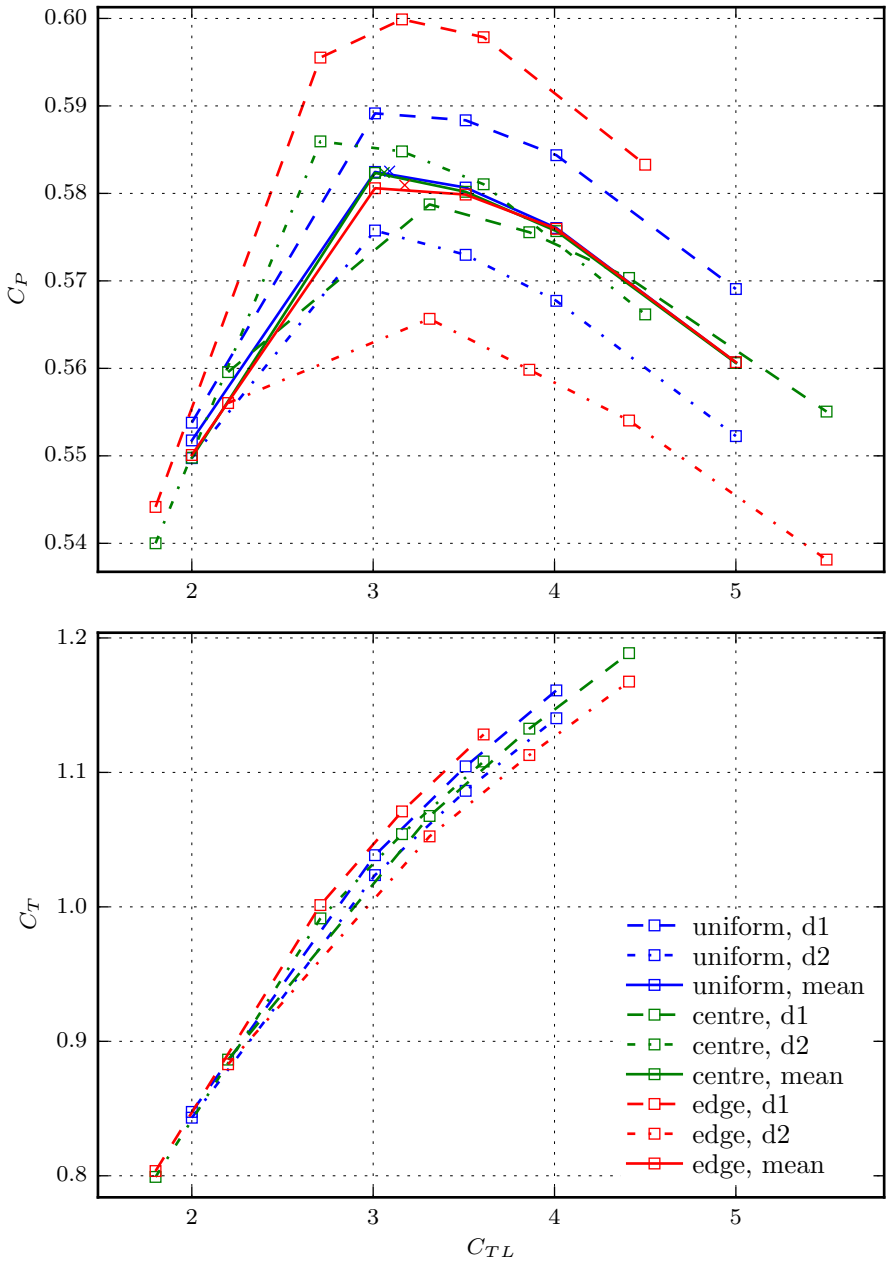


Figure 5.8: C_P, C_T of disk 1 and 2 (centre and edge) of a 4-disk array using a symmetry plane. Rotors are designed at $\lambda = 4.5$, where 'uniform' indicates that both disks are designed using the same C_{TL}^{target}, while 'centre' indicates that C_{TL}^{target} is adjusted 10% higher for disk 1 and 10% lower for disk 2, about the same mean value as the uniform case, and vice-versa for 'edge'.

5.4 Rotor performance

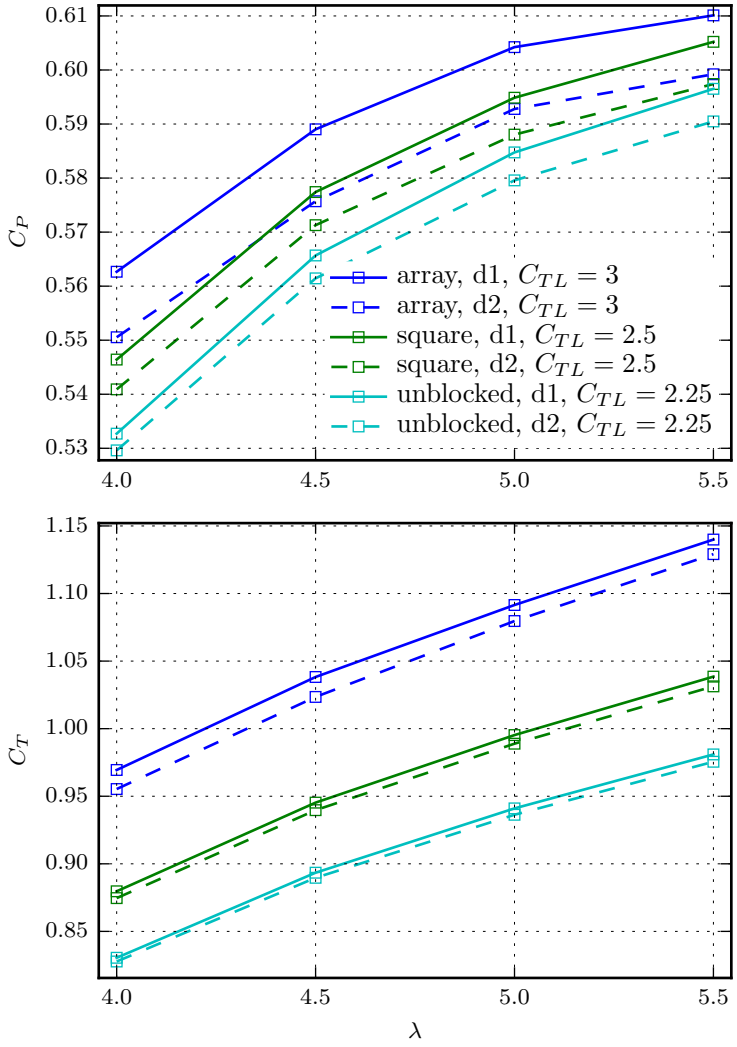


Figure 5.9: Performance of rotor designs in channel domain in terms of C_P, C_T for a range of λ. The in situ designed 'array rotors' have different geometries at each array position, while the 'square' and 'unblocked' rotors have a single design across the array, and were designed in isolation at medium and low blockage, respectively.

In this final section, the rotors designed in Section 5.3 are operated in the four disk array in the channel domain at different tip-speed ratios. As turbine controllers attempt to find the maximum power point, it is possible that non-optimal rotors will simply be run at higher tip-speed ratios in order to support the thrust required to extract maximum power in an array. In Figure 5.9, increasing λ from 4.5 to 5.5 for the rotors designed in either the quasi-unblocked, or square domain with the same

blockage as the channel, results in an increase of power even above the level of the in situ designed rotors operating at the design $\lambda = 4.5$. This may appear to question the need for simultaneous in situ multi-rotor design methods as presented in this chapter as a sub-optimal design can simply be run at a higher tip-speed ratio. However, as discussed in Section 4.3.1, tidal turbines will be limited to lower tip-speed ratios in order to avoid cavitation. If the higher tip-speed ratio is somehow permissible, because of the cavitation insensitive aerofoil section or sufficient submersion depth, then the results suggest that the in situ designed rotors will always outperform a rotor designed in isolation. The effect of operating the turbines designed in isolation away from their design point may be observed in Figure 5.10. Most notably, the angle of attack for the rotor designed in the 'square' domain (equal global blockage to channel domain) already deviates from α_{LD} at the design tip-speed ratio due to operation in a domain markedly different from that for which it was designed, but deviates further at $\lambda = 5.5$ due to above operational design rotational speed, resulting in loss of torque to drag. In contrast, the array designed rotors maintain the α_{LD} as required by their design and correspondingly higher C_T and reduced mass flow (increased induction).

It is worth noting that some of the effects of operating in a blocked environment are experienced "for free" without explicitly designing for them; the in-array performance of the square blockage designed rotor is still 10% greater than its performance in the relatively unblocked environment for which it is designed. It is also clear that although additional power could be generated by the square rotor domain design without designing for it, such power increase comes with an unknown change in blade loads that can only be determined from the analysis of the in situ performance of the disks in the array.

Figure 5.11 shows a plot of streamwise velocity contours on the midplane through the centre of the symmetric four-turbine array. Streamlines passing through the disk are shown as in Figure 5.4. It is notable that the counter-rotating disks result in increased wake mixing, which corresponds to a small increase in array C_P (0.2%). It is also apparent that the predictable streamline pattern for the isolated rotor of Figure 5.4 is largely maintained even in the presence of other turbines in a closely spaced array.

This chapter concludes by noting that, for the chosen tip-speed ratio, the in situ designed array achieves an array C_P of 0.58 which is a marked increase on the implied Betz optimal limit of 0.46, and a modest increase from the performance of operating the unblocked rotor design in the array, i.e. $C_P = 0.56$.

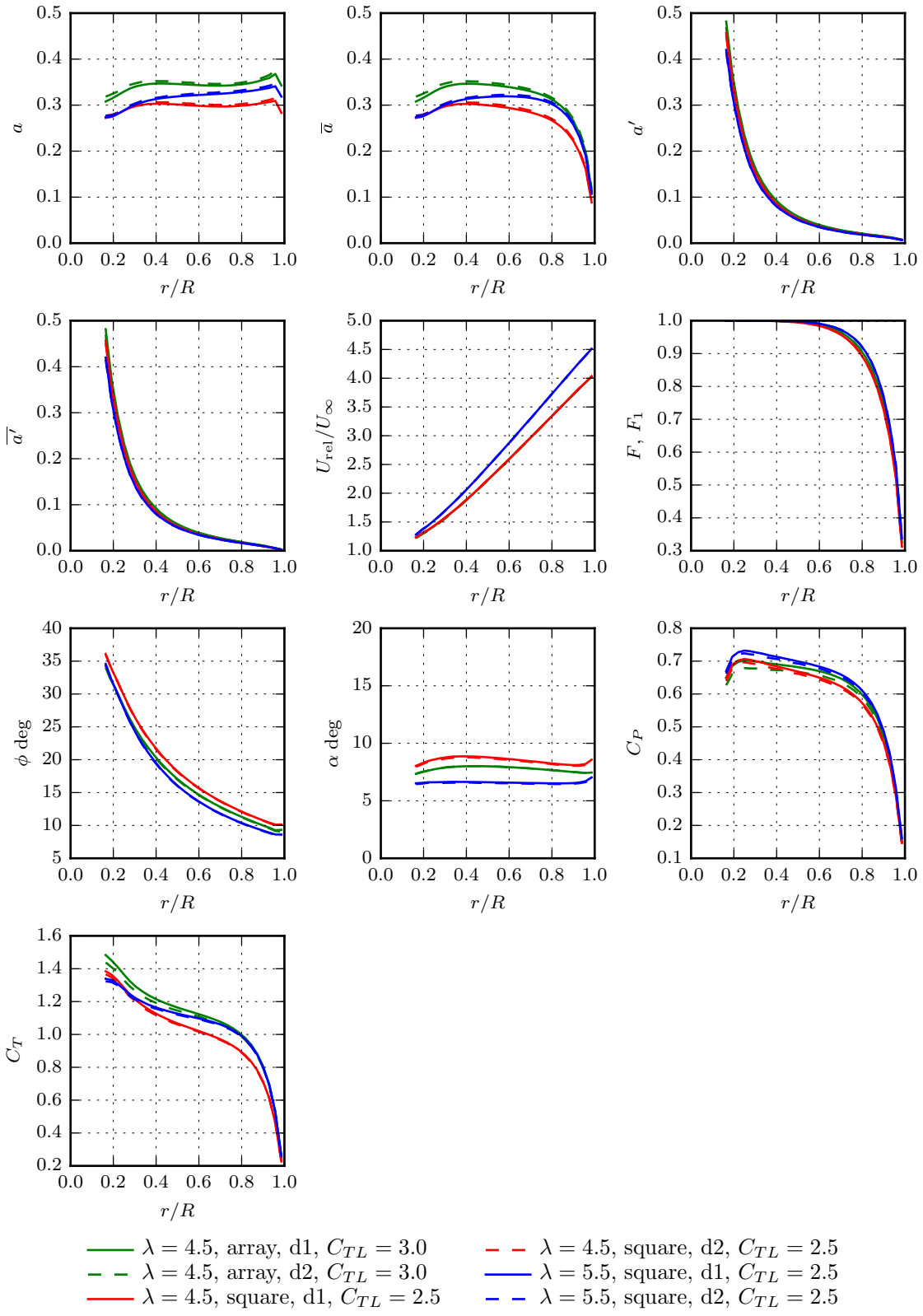


Figure 5.10: Radial outputs from the CFD solver for the in situ designed array rotor and rotor designed in isolation in the 'square' domain. Results for the latter are also plotted at a higher than design tip-speed ratio

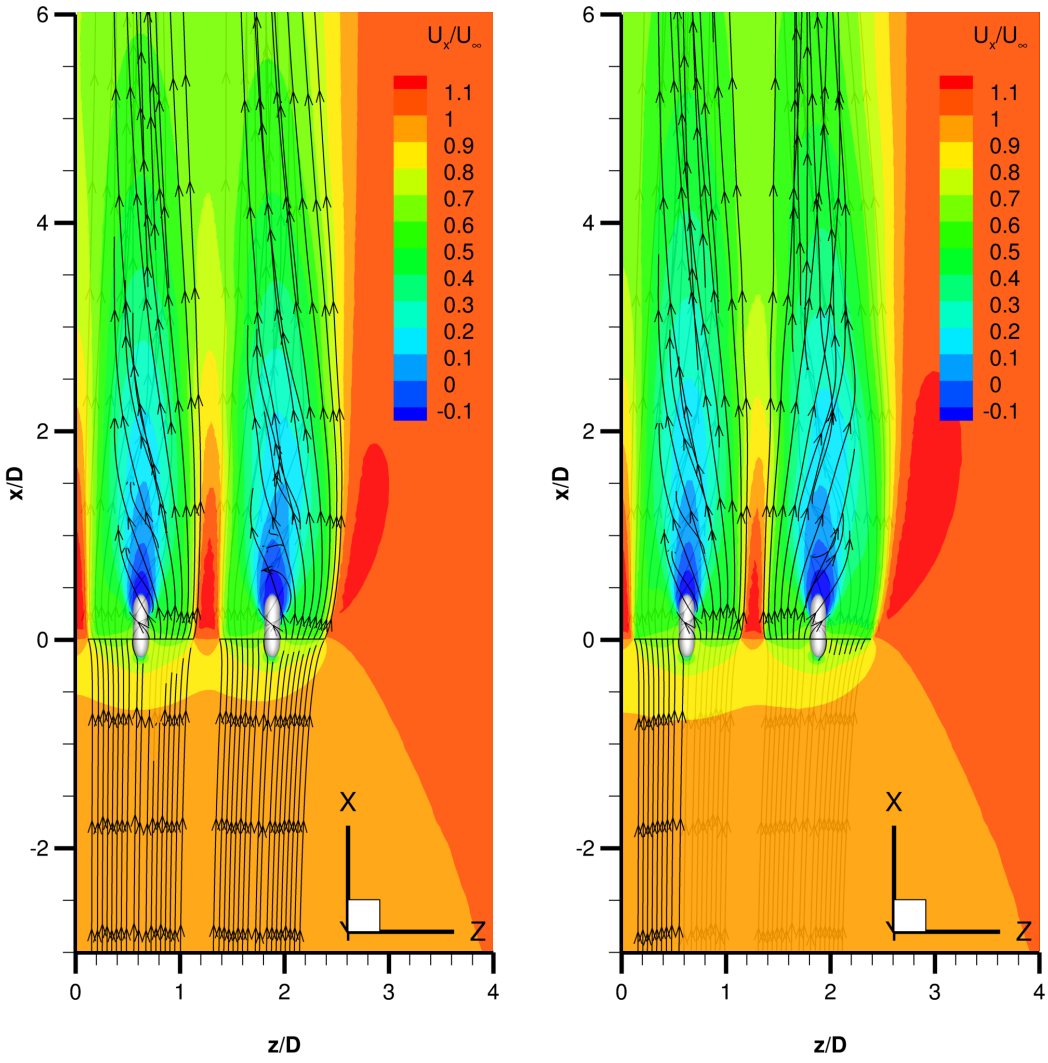


Figure 5.11: Velocity contours and streamlines for two rotors (on one side of the $z = 0$ symmetry plane) of the four disk array as viewed from above (cf. Figure 2.1), with the undisturbed flow direction up the page. Left: both turbines rotating in a positive sense about the axial, x-axis. Right: Counter-rotating turbine operation, producing marginally higher power due to improved wake mixing.

Chapter 6

Conclusions

6.1 Conclusions

A simple and advanced CFD embedded actuator disk model have been used to address the aims outlined in Section 1.3. This begins in Chapter 2 with a study of the limit of energy extraction of a fence of ideal tidal turbines using the simple actuator disk model. Motivated by the predictions of existing analytical models, a number of array layouts and configurations, which would be difficult or impossible to model analytically, are investigated numerically. Where comparable, the results agree qualitatively with the analytical models, thus confirming their assumptions, while new conclusions are made for staggered and non-uniform operation of arrays. These results suggest that the best strategy to maximise the power extraction by a given number of turbines is to arrange them in a non-staggered array (with an optimal intra-turbine spacing that can be estimated analytically), and operate them with a uniform flow resistance coefficient across the entire array

Chapter 3 presents the development and validation of an advanced CFD embedded actuator disk model using blade element theory. The validation study uses selected results from the NREL Phase VI Unsteady Aerodynamics Experiment, the largest scale wind turbine wind tunnel experiment to date, using a two-bladed rotor of diameter, $D = 10.058$ m. The implementation of the model as a customised boundary condition in ANSYS® Fluent® is described in full detail. Application of the model to the wind tunnel experiment shows very good qualitative agreement, while demonstrating the effect of a number of commonly used correction models, and highlighting the challenge of "constructing" suitable tables of aerodynamic forces as input data for aerofoils.

Following the analysis of ideal turbines and real but pre-defined turbines in Chapters 2 and 3, respectively, Chapter 4 addresses the subject of rotor design for tidal

turbines. The historical development of rotor design theory is outlined which necessarily introduces lifting line theory and its relationship to the blade element method. Using an open source implementation of the numerical lifting line method, properties of the design space for turbines are explained and compared to the results of the CFD blade element actuator disk model. This is followed by a thorough discussion of the correction methods applied to the BEM method, and the postulation of a target loading distribution to enable the actuator disk model to be used also as a design tool. The design tool is demonstrated on the design of a rotor for a quasi-unblocked flow, including a discussion of the effect of tip correction models and comparison with the lifting line design.

The overall aim of the thesis, as formulated in Section 1.3, is fulfilled in Chapter 5 with the application of the design tool of Chapter 4 to simultaneous design of multiple tidal turbine rotors, in situ, in a fence emulating the four turbine array of Chapter 2. Array performance is compared for the in situ designed rotors (different rotor geometry for each location across the fence), and the same array using a single rotor, which is designed in isolation. The four turbine array of in situ designed rotors (slightly) outperforms the same array layout using rotors designed in isolation, and has an array $C_P = 0.58$, which is significantly higher than the implied optimal limit of 0.46 from classical rotor theory, which does not account for the effects of global and local blockage and free stream turbulence.

6.2 Contributions

Operation and layout of tidal turbine arrays

A number of questions regarding the design of arrays of tidal turbines have been posed and answered, with a high degree of certainty, by demonstration using simple and advanced actuator disk models. Two particular hypotheses suggested increasing the output of arrays of tidal turbines by non-uniform operation of turbines across the array, or staggering the array into sub-arrays. Array layout optimization continues to be a key interest of the tidal energy research community and this thesis has delivered important conclusions to the field.

RANS blade element actuator disk

The description of the blade element RANS actuator disk model in Chapter 3 and subsequent application to the modelling of test sequences from the NREL Phase VI

experiment represents the most thorough approach to validation of this type of model that the author is aware of. The effect of all commonly used correction models to the standard BEM model (relevant to the selected experimental runs, i.e. steady inflow, zero yaw) are quantitatively demonstrated in an effort focused on transparency rather than seeking the best agreement between simulation and experiment.

Rotor design for tidal turbines in closely spaced arrays

Finally, in recognition of the different flow conditions present across an array of closely spaced turbines, a design method is presented which enables the simultaneous, in situ design of rotors in an array. The resulting rotor designs are different depending on their location in the array, directly responding to the local flow field. The same tool is used to evaluate the performance of the array for given turbine designs and shows that, for a given design tip-speed ratio, the in situ designed rotors outperform an array of rotors designed in isolation. If cavitation or other constraints permit, operating the turbine designed in isolation at a higher tip-speed ratio compensates some of the difference in performance.

6.3 Future work

Blade resolved simulations

The range of corrections that have been suggested for the blade element momentum method highlights the limited accuracy of the basic equations to describe the flow through an axial rotor. As a result, all actuator methods require validation for each new usage case. The extension of the CFD-embedded blade element actuator disk in the current study incorporates the theoretical insights of the lifting line method, but still requires additional validation. Rotors designed in isolation may be simulated by solving the RANS equations in a single moving reference frame for a cylindrical domain. This would enable evaluation of rotor designs for different levels of blockage and at varying freestream turbulence levels, as well as different rotational speeds (or tip-speed ratios). However, there are some challenges in making quantitative comparisons with the RANS actuator disk results. Firstly, while the axial and tangential forces in the actuator disk model are derived from lift and drag polars, the resolved simulations return the flow field surrounding the blade as well as the surface forces on the blades. In order to make comparisons between the models, a consistent approach must be defined for constructing the aerodynamic tables for the actuator disk model

from the resolved simulations. Given the uncertainty surrounding experimental data discussed in Chapter 3, and the limitations of viscous-inviscid codes, such as Xfoil, for predicting, e.g. the effect of freestream turbulence, the author proposes that the aerodynamic tables should be based on 2D RANS simulations of the sections. If care is taken to match the flow conditions (chord-based Reynolds number and freestream turbulence), grid resolution and numerical settings, then the need for additional correction of the data can be clearly evaluated. It may also be more challenging to generate quality meshes for the geometries of optimum rotors compared to typical wind turbine rotors. The large solidity at the root tapering to almost zero chord length at the tip as well as the high twist of the root sections make high quality structured hexahedral blocking challenging for these rotors.

Depending on the success of this initial validation, simulations of a short tidal turbine array, like the 4 turbine fence of Chapters 2 and 5, could possibly be attempted using multiple rotating reference frames in the fixed channel domain.

Lifting line model

The rotor designs produced by the current blade element actuator disk model rely on a loading distribution, which has been postulated based on the results of the lifting line method. The lifting line method inherently assumes an unblocked flow domain and cannot account for the effect of free stream turbulence. These restrictions are less critical for wind turbine design and analysis, and the method is widely used in industry and academia. However, it is almost certain that the optimal loading distribution for tidal turbines in a closely spaced array will be different from a simple linear scaling of the optimal distribution of an isolated turbine. The author considers that this problem could be tackled in two ways: Using blade resolved simulations as outlined in the previous sections, incremental improvements to the loading distribution could be made to attempt to approach the optimum. Alternatively, it may be possible to extend the lifting line method to account for the flow confining effect of channel boundaries or neighbouring turbines, by using singularity elements modelling symmetry planes. However, it is likely that the optimization procedure, outlined in Chapter 4, would become much more computationally expensive.

Bibliography

[1] ANSYS Inc. *ANSYS Fluent Theory Guide*, 15.0 ed. Cannonsburg, PA, 2013.

[2] ANSYS Inc. *ANSYS ICEM CFD User's Manual*, 15.0 ed. Cannonsburg, PA, 2013.

[3] Bahaj, A. S., Batten, W. M. J., and McCann, G. Experimental verifications of numerical predictions for the hydrodynamic performance of horizontal axis marine current turbines. *Renewable Energy 32*, 15 (2007), 2479–2490.

[4] Batten, W. M. J., Harrison, M. E., and Bahaj, A. S. Accuracy of the actuator disc - RANS approach for predicting the performance and wake of tidal turbines. *Philosophical Transactions of the Royal Society of London A: Mathematical, Physical and Engineering Sciences 371*, 1985 (2013).

[5] BERR. Atlas of UK Marine Renewable Energy Resources. Tech. rep., 2008.

[6] Betz, A. Schraubenpropeller mit geringstem Energieverlust. Mit einem Zusatz von L. Prandtl. *Nachrichten von der Gesellschaft der Wissenschaften zu Göttingen, Mathematisch-Physikalische Klasse* (1919), 193–217.

[7] Betz, A. Das Maximum der theoretisch möglichen Ausnützung des Windes durch Windmotoren. *Zeitschrift für das gesamte Turbinenwesen 26*, 307-309 (1920), 8.

[8] Black & Veatch. UK Tidal Current Resource & Economics. Tech. rep., Carbon Trust, 2011.

[9] Branlard, E. Wind turbine tip-loss corrections. Master's thesis, Risø DTU, Copenhagen, Denmark, 2013.

[10] Bryden, I. Survey of Energy Resources. Tech. rep., World Energy Concil, 2007.

[11] Burton, T., Jenkins, N., Sharpe, D., and Bossanyi, E. *Wind Energy Handbook*. John Wiley & Sons, 2011.

[12] Consul, C. A., Willden, R. H. J., and McIntosh, S. C. Blockage effects on the hydrodynamic performance of a marine cross-flow turbine. *Philosophical Transactions of the Royal Society of London A: Mathematical, Physical and Engineering Sciences 371*, 1985 (2013), 20120299.

[13] de Vries, O. Fluid dynamic aspects of wind energy conversion. Tech. rep., DTIC Document, 1979.

[14] Døssing, M., Madsen, H. A., and Bak, C. Aerodynamic optimization of wind turbine rotors using a blade element momentum method with corrections for wake rotation and expansion. *Wind Energy 15*, 4 (2012), 563–574.

[15] Draper, S., Adcock, T. A. A., Borthwick, A. G. L., and Houlsby, G. T. Estimate of the tidal stream power resource of the Pentland Firth. *Renewable Energy 63* (2014), 650–657.

[16] Draper, S., and Nishino, T. Centred and staggered arrangements of tidal turbines. *Journal of Fluid Mechanics 739* (2014), 72–93.

[17] Draper, S., and Nishino, T. Centred and staggered arrangements of tidal turbines - ERRATUM. *Journal of Fluid Mechanics 743* (2014), 636–636.

[18] Drela, M. Xfoil: An analysis and design system for low Reynolds number airfoils. In *Low Reynolds Number Aerodynamics*. Springer, 1989, pp. 1–12.

[19] Du, Z., and Selig, M. S. A 3-D stall-delay model for horizontal axis wind turbine performance prediction. *AIAA Paper 21* (1998), 9–19.

[20] Eggers, A. J., Chaney, K., and Digumarthi, R. An assessment of approximate modeling of aerodynamic loads on the UAE rotor. In *ASME 2003 Wind Energy Symposium* (2003), pp. 283–292.

[21] EMEC. The European Marine Energy Centre Ltd: Our Tidal Clients. `http://www.emec.org.uk/about-us/our-tidal-clients`. Accessed Jan 14, 2016.

[22] Epps, B. P., and Kimball, R. W. OpenProp v3: Open source software for the design and analysis of marine propellers and horizontal-axis turbines. `http://www.engineering.dartmouth.edu/epps/openprop`, 2013–.

[23] Epps, B. P., and Kimball, R. W. Unified rotor lifting line theory. *Journal of Ship Research 57*, 4 (2013), 181–201.

[24] Fleming, C. *Tidal turbine performance in the offshore environment.* PhD thesis, University of Oxford, UK, 2014.

[25] Fraenkel, P. MCT's SeaGen tidal turbine. In *The 4th Annual Global Marine Renewable Energy Conference* (2011).

[26] Froude, R. E. On the part played in propulsion by differences of fluid pressure. *Transactions of the Institution of Naval Architects 30* (1889), 390–405.

[27] Garrett, C., and Cummins, P. The power potential of tidal currents in channels. In *Proceedings of the Royal Society of London A: Mathematical, Physical and Engineering Sciences* (2005), vol. 461, pp. 2563–2572.

[28] Garrett, C., and Cummins, P. The efficiency of a turbine in a tidal channel. *Journal of Fluid Mechanics 588* (2007), 243–251.

[29] Giguere, P., and Selig, M. S. Design of a tapered and twisted blade for the NREL combined experiment rotor. *NREL/SR 500* (1999), 26173.

[30] Glauert, H. Airplane propellers. In *Aerodynamic Theory.* Springer, 1935, pp. 169–360.

[31] Goldstein, S. On the vortex theory of screw propellers. *Proceedings of the Royal Society of London. Series A, Containing Papers of a Mathematical and Physical Character* (1929), 440–465.

[32] Hand, M. M., Simms, D. A., Fingersh, L. J., Jager, D. W., Cotrell, J. R., Schreck, S., and Larwood, S. M. Unsteady Aerodynamics Experiment Phase VI: Wind tunnel test configurations and available data campaigns. Tech. rep., 2001.

[33] Hansen, M. O. L. *Aerodynamics of Wind Turbines.* Routledge, 2015.

[34] Houlsby, G. T., Draper, S., and Oldfield, M. L. G. Application of linear momentum actuator disc theory to open channel flow. Tech. rep., University of Oxford Report No. OUEL 2296/08, 2008.

[35] Hunter, W., Nishino, T., and Willden, R. H. J. Investigation of tidal turbine array tuning using 3D Reynolds-averaged Navier–Stokes simulations. *International Journal of Marine Energy 10* (2015), 39–51.

[36] Johansen, J., Madsen, H. A., Sørensen, N. N., and Bak, C. Numerical investigation of a wind turbine rotor with an aerodynamically redesigned hub-region. In *2006 European wind energy conference and exhibition, Athens, Greece* (2006).

[37] Jones, E., Oliphant, T., Peterson, P., et al. SciPy: Open source scientific tools for Python. `http://www.scipy.org`, 2001–.

[38] Katz, J., and Plotkin, A. *Low-speed Aerodynamics.* Cambridge University Press, 2001.

[39] Kerwin, J. E., and Hadler, J. B. *Principles of Naval Architecture: Propulsion.* SNAME, 2010.

[40] Lanchester, F. W. A contribution to the theory of propulsion and the screw propeller. *Transactions of the Institution of Naval Architects 56* (1915), 98–116.

[41] Launder, B. E., and Spalding, D. B. *Lectures in Mathematical Models of Turbulence.* Academic Press, London, England, 1972.

[42] Lindenburg, C. Investigation into rotor blade aerodynamics. *ECN Report: ECN-C-03-025* (2003).

[43] Madsen, H. A., Bak, C., Døssing, M., Mikkelsen, R., and Øye, S. Validation and modification of the blade element momentum theory based on comparisons with actuator disc simulations. *Wind Energy 13*, 4 (2010), 373–389.

[44] Malki, R., Masters, I., Williams, A. J., and Croft, T. N. Planning tidal stream turbine array layouts using a coupled blade element momentum - computational fluid dynamics model. *Renewable Energy 63* (2014), 46–54.

[45] McIntosh, S. C., Fleming, C. F., and Willden, R. H. J. Embedded RANS-BEM tidal turbine design. In *Proc. 9th European wave and tidal energy conf* (2011).

[46] Moffitt, B. A., Bradley, T. H., Parekh, D. E., and Mavris, D. Validation of vortex propeller theory for UAV design with uncertainty analysis. In *46th AIAA Aerospace Sciences Meeting and Exhibit* (2008), no. 406.

[47] Moriarty, P. J., and Hansen, A. C. *AeroDyn theory manual*, 2005.

[48] Munk, M. M. The minimum induced drag of aerofoils. Tech. rep., NACA Report No. 121, 1923.

[49] Ning, S. A. *AirfoilPrep.py Documentation*, 2013.

[50] Nishino, T., and Willden, R. H. J. Effects of 3-D channel blockage and turbulent wake mixing on the limit of power extraction by tidal turbines. *International Journal of Heat and Fluid Flow 37* (2012), 123–135.

[51] Nishino, T., and Willden, R. H. J. The efficiency of an array of tidal turbines partially blocking a wide channel. *Journal of Fluid Mechanics 708* (2012), 596–606.

[52] Nishino, T., and Willden, R. H. J. The efficiency of tidal fences: A brief review and further discussion on the effect of wake mixing. In *ASME 2013, 32nd International Conference on Ocean, Offshore and Arctic Engineering* (2013).

[53] Nishino, T., and Willden, R. H. J. Energetics of marine turbine arrays - extraction, dissipation and diminution. In *Proceedings of the International Symposium on Marine and Offshore Renewable Energy, Tokyo, Japan* (2013).

[54] Nishino, T., and Willden, R. H. J. Two-scale dynamics of flow past a partial cross-stream array of tidal turbines. *Journal of Fluid Mechanics 730* (2013), 220–244.

[55] O'Doherty, T., Egarr, D. A., Mason-Jones, A., and O'Doherty, D. M. An assessment of axial loading on a five-turbine array. *Proceedings of the ICE-Energy 162*, 2 (2009), 57–65.

[56] Patankar, S. V. *Numerical Heat Transfer and Fluid Flow*. Hemisphere Publishing Corporation, 1980.

[57] Pope, S. B. *Turbulent Flows*. Cambridge University Press, 2000.

[58] Rhie, C. M., and Chow, W. L. Numerical study of the turbulent flow past an airfoil with trailing edge separation. *AIAA Journal 21* (1983), 1525–1532.

[59] Ronsten, G. Static pressure measurements on a rotating and a non-rotating 2.375 m wind turbine blade. comparison with 2D calculations. *Journal of Wind Engineering and Industrial Aerodynamics 39*, 1 (1992), 105–118.

[60] Sanderse, B., van der Pijl, S. P., and Koren, B. Review of computational fluid dynamics for wind turbine wake aerodynamics. *Wind Energy 14*, 7 (2011), 799–819.

[61] Schluntz, J., and Willden, R. H. J. The effect of blockage on tidal turbine rotor design and performance. *Renewable Energy 81* (2015), 432–441.

[62] Shen, W. Z., Mikkelsen, R., Sørensen, J. N., and Bak, C. Tip loss corrections for wind turbine computations. *Wind Energy 8*, 4 (2005), 457–475.

[63] Shen, W. Z., Sørensen, J. N., and Mikkelsen, R. Tip loss correction for actuator/Navier–Stokes computations. *Journal of Solar Energy Engineering 127*, 2 (2005), 209–213.

[64] Snel, H., Houwink, R., and Bosschers, J. Sectional prediction of lift coefficients on rotating wind turbine blades in stall. Tech. rep., 1994.

[65] Snel, H., and van Holten, T. Review of recent aerodynamic research on windturbines with relevance to rotorcraft. In *Aerodynamics and Aeroacoustics of Rotorcraft* (1994), AGARD.

[66] Sørensen, J. N. Aerodynamic aspects of wind energy conversion. *Annual Review of Fluid Mechanics 43* (2011), 427–448.

[67] Sørensen, J. N., and Kock, C. W. A model for unsteady rotor aerodynamics. *Journal of Wind Engineering and Industrial Aerodynamics 58*, 3 (1995), 259–275.

[68] Sørensen, J. N., and Myken, A. Unsteady actuator disc model for horizontal axis wind turbines. *Journal of Wind Engineering and Industrial Aerodynamics 39*, 1 (1992), 139–149.

[69] Sørensen, J. N., and Shen, W. Z. Numerical modeling of wind turbine wakes. *Journal of Fluids Engineering 124*, 2 (2002), 393–399.

[70] Sørensen, N. N., and Hansen, M. O. L. Rotor performance predictions using a Navier–Stokes method. In *36th Aerospace Sciences Meeting and Exhibition* (1998), no. 25.

[71] Sørensen, N. N., Michelsen, J. A., and Schreck, S. Navier–Stokes predictions of the NREL Phase VI rotor in the NASA Ames 80 ft $\times$ 120 ft wind tunnel. *Wind Energy 5*, 2-3 (2002), 151–169.

[72] Stewart, H. J. Dual optimum aerodynamic design for a conventional windmill. *AIAA Journal 14*, 11 (1976), 1524–1527.

[73] Sun, X., Chick, J. P., and Bryden, I. G. Laboratory-scale simulation of energy extraction from tidal currents. *Renewable Energy 33*, 6 (2008), 1267–1274.

[74] Vennell, R. Tuning tidal turbines in a tidal channel. *Journal of Fluid Mechanics 663* (2010), 253–267.

[75] Vennell, R. Tuning tidal turbines in-concert to maximise farm efficiency. *Journal of Fluid Mechanics 671* (2011), 587–604.

[76] Viterna, L. A., and Janetzke, D. C. Theoretical and experimental power from large horizontal-axis wind turbines. Tech. rep., National Aeronautics and Space Administration, Cleveland, OH (USA). Lewis Research Center, 1982.

[77] White, F. *Fluid Mechanics*. McGraw-Hill, 2015.

[78] Wrench Jr, J. W. The calculation of propeller induction factors AML Problem 69-54. Tech. rep., DTIC Document, 1957.